Ultrafast Vibrational Dynamics of Biomimetic Catalysts

By

Peter A. Eckert

A dissertation submitted in partial fulfillment of
the requirements for the degree of
Doctor of Philosophy
(Chemistry)
in the University of Michigan
2018

Doctoral Committee:

Professor Kevin Kubarych, Chair
Professor Eitan Geva
Professor Roseanne Sension
Professor Stephen Ragsdale

Peter A. Eckert
zpeckert@umich.edu
ORCID iD: 0000-0002-8875-440X

Dedication

To my Mother

Acknowledgments

I acknowledge first and foremost my advisor, Dr. Kevin Kubarych. Kevin has been a patient and insightful mentor and has incessantly supported my development as a practitioner and communicator of scientific research. The freedom which he has given me to pursue my vision throughout my graduate studies has enabled me to synthesize and study the range of molecular systems presented in this work.

I am deeply indebted to the past and present members of the Kubarych group, with whom I have learned how to perform scientific research and communicate the results. I am especially indebted to Dr. Laura Kiefer and to Lindsay Michocki for their unfailing patience and insight.

I thank my candidacy committee members, Professor Roseanne Sension, Professor Eitan Geva, Professor Mary Anne Carroll and Professor Stephen Ragsdale for scientific advice and support that they have provided me during my time at the University of Michigan. I especially thank Professor Ragsdale for his graciousness in joining my committee after I had advanced to candidacy.

I gratefully acknowledge the support of the University of Michigan, particularly the Rackham Graduate School for a Post-Candidacy Research Grant and two Travel Grants.

I deeply acknowledge the immeasurable support of my friends and family and thank my parents and my siblings, Tabitha, James, Matthew, Josiah, Ruthanna, and Sarah, for their presence during this time, especially my mother and Matthew. I thank Bryce Brown, Charles Flowe, and Jonathan Jaber for grounding and uplifting me throughout the process, and Emma Navarro, Monika Blazeski, and Katherine Miller for showing me how to discern and value the joy and the meaning in my life.

Finally, I would like to thank Dr. Dori Karlesky, Dr. Paul Bialek, and Dr. Alexander Laskin for their mentorship during my time as an undergraduate.

I dedicate this work to my beloved mother, Susan Eckert.

Table of Contents

Dedication ii

Acknowledgments ii

List of Figures vi

List of Abbreviations xv

Abstract xvii

Chapter 1: Introduction 1

1.1 Introduction 1

1.2 Hydrogenase enzyme and Active-Site Mimics 2

1.3 Metal Carbonyls and Two-Dimensional Infrared Spectroscopy 7

1.4 Experimental Details and Experimental Observables 8

1.4.1 Experimental Set-up. 8

1.4.2 Vibrational Relaxation. 10

1.4.3 Cross Peaks and IVR. 11

1.4.4 Spectral Diffusion. 13

1.5 Outline 15

Chapter 2: Oxidation-State Dependent Vibrational Dynamics Probed with 2D-IR 27

2.1 Introduction 27

2.2 Experimental Procedures 31

2.3 Results 33

2.4 Discussion 35

2.5 Conclusion 40

Chapter 3: Dynamic Flexibility of Hydrogenase Active Site Models Studied with 2D-IR 47

3.1 Introduction 47

3.2 Experimental Methods 51

3.3 Results 51

3.4 Discussion 54

3.5 Conclusion 63

Chapter 4: Dendritic Modulation of Vibrational Dynamics in a Biomimetic Photocatalyst Studied with 2D-IR 71

4.1 Introduction 71

4.2 Experimental Details 74

4.3 Results 76

4.4 Discussion 78

4.5 Conclusion 87

Chapter 5: Vibrational Coherence Transfer in a Class of Excitonic Biomimetic Catalysts Studied with 2D-IR 93

5.1 Introduction 93

5.2 Experimental Methods 95

5.3 Results 96

5.4 Discussion 101

5.5 Conclusion 112

Chapter 6: Conclusion 119

6.1 Summary 119

6.2 Outlook 121

Appendix 130

A1: Spectral Diffusion and IVR Data for $[Fe(\mu\text{-}S)(CO)_3]_2$ and the Dendrimer 130

List of Figures

Figure 1.1: (A) (μ-pdt)[Fe(CO)$_3$]$_2$ (pdt =1,3-propanedithiolate), an archetypical [FeFe]-hydrogenase enzyme active site mimic. (B) [FeFe]-hydrogenase active site. (C) Molecular geometry of (μ-pdt)[Fe(CO)$_3$]$_2$ in the transition-state of the turnstile carbonyl isomerization, where the carbonyl ligands are rotated ~ 60° from the ground state geometry. Note the similarity of the turnstile transition state of (μ-pdt)[Fe(CO)$_3$]$_2$ to the geometry of the hydrogenase enzyme active site, especially the exposed iron atom. (D) Diagram of the proposed proton-shuttling mechanism in hydrogenase enzyme active site. The direct accessibility of the iron atom is significant to the formation of a reactive terminal hydride 3

Figure 1.2: (A) Reaction mechanism proposed by Lyon et. al. for the nucleophilic substitution of CO by cyanide in (μ-edt)[Fe(CO)$_3$]$_2$ (edt =1,2-ethanedithiolate). The reaction is initiated by a turnstile-type isomerization of the carbonyl groups on one iron atom and nucleophilic substitution occurs in the transition state of the carbonyl isomerization.[13] (B) Reaction mechanism proposed by Felton et. al. for the electrochemical production of H_2 by (μ-bdt)[Fe(CO)$_3$]$_2$ (bdt =1,2-benzenedithiolate). The catalyst is prepared by reduction of (μ-bdt)[Fe(CO)$_3$]$_2$ and a bridging hydride is formed as a key intermediate in the catalytic mechanism.[14] Both of these mechanisms involve a turnstile-type reorganization of the carbonyl groups on one of the iron atoms. 5

Figure 1.3: (A) (μ-1,3-propanedithiolate)[Fe(CO)$_3$]$_2$, an archetypical [FeFe]-hydrogenase enzyme active site mimic. (B) Infrared spectrum of the carbonyl vibrational modes of (μ-1,3-propanedithiolate)[Fe(CO)$_3$]$_2$ in hexane, with vibrational frequencies numbered from highest to lowest. (C) Atomic displacements for the carbonyl vibrations of the diiron hexacarbonyl molecules used in this work. Vibrational

modes are numbered from highest to lowest frequency, corresponding to the numbering of the spectrum in (B), and are referred to by their numbering scheme in the remainder of this work. Mode 6 is not IR active. 7

Figure 1.4: (A) Depiction of the experimental pulse sequence, with pulses $\mathbf{k_1}$, $\mathbf{k_2}$, and $\mathbf{k_3}$, and the time intervals between them, t_1, t_2, and t_3. (B) Depiction of the spatial alignment of the three pulses in a box geometry and the background-free direction of the signal field. 9

Figure 1.5: (A) Model peak amplitude decays for a diagonal peak, displaying a biphasic monotonic decay of peak amplitude, and a cross peak, displaying an increased in peak amplitude during early waiting times followed by a decrease in in peak amplitude. (B) Ratio of the time-dependent amplitudes of the diagonal and cross peak. The ratio begins to approach a value of one after ~ 40 ps, and visual inspection of 3a will show a corresponding similarity of the diagonal and cross peak on the same timescale. 12

Figure 1.6: (A) A single homogeneously broadened peak, corresponding to the spectral response of a system with a single microstate. (B) A single inhomogeneously broadened peak, corresponding to the spectral response of a system with multiple microstates, each of which with a slightly differing frequency. (C) A fluctuation of frequency within the inhomogeneously broadened system corresponding to a change in microstate experienced by the sample. The timescale required for a system to sample all of its available microstates is described by the frequency-frequency autocorrelation function (FFCF). 14

Figure 2.1. (A-C) Schematic representation, DFT-optimized geometry, and space-filling representation of DPPFCr. Note that in the space-filling representation the carbonyl groups are somewhat enclosed by the four phenyl groups. (D) FTIR spectra of the four carbonyl stretching modes of DPPFCr in neutral (top) and oxidized (bottom) electronic states. Note that the x-axes are shifted by roughly 100 cm^{-1} due to the change in electronic structure, and that gaussian fits have been added to the spectra to clarify the overlapping vibrational bands. (E) Mode

assignments based on quantum chemical calculations. This figure was adapted from the journal article in which these results were published. 27

Figure 2.2. A) Normalized peak amplitude of mode 1 in CH_2Cl_2 for DPPFCr(0) and DPPFCr(I). Vibrational lifetimes given by the fits are listed in the figure. B) 2D-IR nonrephasing spectrum of mode 1, DPPFCr(I), in CH_2Cl_2, 3.7 ps after excitation. C) Ratio of the amplitudes of the (ω_{excite}=mode 2, ω_{detect}=mode 1) cross peak and the diagonal mode 1 peak in CH_2Cl_2. The timescale for intramolecular vibrational randomization for DPPFCr(0) and DPPFCr(I) are given as 11.2±2 ps and 4.6±2 ps, respectively. D) Spectral diffusion data for mode 1 of DPPFCr(0) and DPPFCr(I) in CH_2Cl_2, with the respective time-constants of 2.5±0.7ps and 2.9 ±0.8 ps. This figure was adapted from the journal article in which these results were published. 33

Figure 2.3. Changes in the partial charges on various atoms and groups in DPPFCr(I) as a percentage of the DPPFCr(0) charges. All charges become more positive since there is a net loss of one electron on the complex. The Cr charge changes the most, followed by the equatorial and the axial carbonyls, respectively. The charge decrease of the equatorial carbonyls is probably associated with the larger frequency shifts of the mode involving only these carbonyl groups. This figure was adapted from the journal article in which these results were published. 34

Figure 3.1: (A) The DFT optimized structure of μ-pdt-$[Fe(CO)_3]_2$ is essentially two-fold symmetric with respect to the carbonyl ligands. (B) The crystallographic hydrogenase enzyme active site reveals an open coordinate site where hydrogen has been shown to bind [PDB: 3C8Y] (C) The transition-state (colors) geometry superposed on the (gray) fully optimized structure shows a conformation resembling that of the enzyme. (D) A depiction of the pendant amine shuttling a proton to iron active site highlights the interrelationship between the bridge and the open coordination site. This figure was adapted from the journal article in which these results were published. 48

Figure 3.2: (A) FTIR of μ-pdt-$[Fe(CO)_3]_2$ in hexane, undecane, and hexadecane. The mode numbering scheme detailed in Chapter 1.3 is recapitulated here. (B) Absolute value 2D-IR rephasing spectrum of μ-pdt-$[Fe(CO)_3]_2$ in hexane, tuned to mode 2. The intense cross peaks reflect coupling between the carbonyl modes. (C) Structure of (μ-pdt)$[Fe(CO)_3]_2$ with arrows indicating the out-of-phase symmetric carbonyl displacements of mode 2. This figure was adapted from the journal article in which these results were published. 52

Figure 3.3: (In all panels, curves are offset for clarity) (A) Frequency-fluctuation correlation functions, $C(t_2)$, for (μ-pdt)$[Fe(CO)_3]_2$ in hexane, undecane, and hexadecane yield essentially indistinguishable decay constants. The oscillatory features appearing during the first 15 ps result from vibrational coherences among the excited CO modes. The data has been offset for clarity of display. (B) A comparison of the FFCFs for (μ-pdt)$[Fe(CO)_3]_2$ and (μ-edt)$[Fe(CO)_3]_2$ in undecane shows a slight slowdown in the case of the edt linker. The data has been offset for clarity of display. (C) The nonrephasing signal amplitude obtained by integrating the peak 2 diagonal of (μ-pdt)$[Fe(CO)_3]_2$ in hexane, undecane, and hexadecane shows indistinguishable long-time decays due to vibrational energy relaxation. The data have been offset for clarity of display. (D) Ratios of crosspeak (ω_{excite} = 2015 cm^{-1}, ω_{detect} = 2038 cm^{-1}) and mode 2 amplitudes for (μ-pdt)$[Fe(CO)_3]_2$ in hexane, undecane, and hexadecane show significant solvent-dependent IVR timescales. The IVR timescales depend linearly on solvent carbon chain length: $\tau_{IVR} = n \times 1.65$ ps + 0.92 ps. The data have been offset for clarity of display. This figure was adapted from the journal article in which these results were published. 53

Figure 3.4: Plot of C≡O site energy vs. C≡O bond length in a series of variants of BCT which were symmetrically tri-substituted at the 1, 3, and 5 positions. The R groups are labeled on the plot. The line of best fit is given by (Site Energy, cm^{-1}) = (-7081 $\frac{cm^{-1}}{Å}$) × (C≡O Bond Length, Å) + 10280 cm^{-1}. This figure was adapted from the journal article in which these results were published. 54

Figure 3.5: (A) The Boltzmann distribution of torsional angles for (μ-pdt)[$Fe(CO)_3$]$_2$ as a function of $Fe(CO)_3$ rotor twist shows significant structural distortion is present at room temperature. (B) Boltzmann distribution of conformations as a function of both $Fe(CO)_3$ rotor twists indicate that the two angles are correlated. This figure was adapted from the journal article in which these results were published. 56

Figure 3.6: (left) The fully optimized structure with bond distances depicted in units of Å; Fe-C are in yellow and C-O are in white. (right) The twisted transition state structure showing the changes in the bond distances relative to the optimized geometry (twisted – optimized). This figure was adapted from the journal article in which these results were published. 58

Figure 3.7: (A) Molecular geometry of $Ru_3(CO)_{12}$. $Os_3(CO)_{12}$ has the same molecular structure. (B) FTIR spectra of $Ru_3(CO)_{12}$ and $Os_3(CO)_{12}$ in dodecane and heptane, respectively. The vibrational bands investigated further are the second-highest frequency band in both spectra, at frequencies of 2031 cm^{-1} in $Ru_3(CO)_{12}$ and 2036 cm^{-1} in $Os_3(CO)_{12}$. (C) 2D-IR spectrum of $Ru_3(CO)_{12}$ in dodecane, with FTIR spectra set across from the excitation and detection axes. (D) Spectral diffusion of vibrational bands at frequencies of 2031 cm^{-1} in $Ru_3(CO)_{12}$ and 2036 cm^{-1} in $Os_3(CO)_{12}$. Although exact fitting is obfuscated by the pronounced vibrational coherences in $Os_3(CO)_{12}$, both data series are well fit by an exponential decay with a single time constant of ~ 5 ps. 60

Figure 4.1: (A) [Fe(μ-S)$(CO)_3$]$_2$, which we use as a reference small-molecule. (B) [Fe(dendron)$(CO)_3$]$_2$, where the dendrons are second-generation Frechet-type poly(aryl ether) dendrimers. 72

Figure 4.2: (A) Representative carbonyl vibrational spectra of [Fe(μ-S)$(CO)_3$]$_2$ and the dendrimer in DMF. The vibrational frequencies of the dendrimer are uniformly red shifted from the frequencies of [Fe(μ-S)$(CO)_3$]$_2$. (B) 2D-IR spectrum of the dendrimer in DMF, centered on mode 2. (C) Carbonyl vibrational spectra of [Fe(μ-S)$(CO)_3$]$_2$ in all of the solvents used in this study. (D) Carbonyl vibrational spectra of the dendrimer in all of the solvents used in this study. (E) Carbonyl vibrational

spectra of $[Fe(\mu\text{-}S)(CO)_3]_2$ in all of the tested solvents, focused on modes 1-2. Note that acetone, $CHCl_3$, and CH_3CN show almost identical vibrational frequencies for mode 1, which are blue shifted from the almost identical vibrational frequencies of mode 1 in toluene, THF, and DMF. (F) Carbonyl vibrational spectra of $[Fe(\mu\text{-}S)(CO)_3]_2$ in all of the tested solvents, focused on modes 1-2. Note that acetone, $CHCl_3$, and CH_3CN show almost identical vibrational frequencies for mode 1, which are blue shifted from the almost identical vibrational frequencies of mode 1 in toluene, THF, and DMF. 75

Figure 4.3: (A) Decay of mode 2's nonrephasing peak amplitude for all solvents tested and for both the dendrimer and $[Fe(\mu\text{-}S)(CO)_3]_2$. Note that the decay in peak amplitude for both compounds in all solvents except $CHCl_3$ are essentially indistinguishable after 60 ps, and in $CHCl_3$ the vibrational relaxation of both compounds appears to become similar as t_2 approaches 80 ps. (B) Decay of mode 2's nonrephasing peak amplitude in THF and acetone, representing solvents in which the early-time vibrational relaxation differs and does not differ, respectively, between the dendrimer and $[Fe(\mu\text{-}S)(CO)_3]_2$. 76

Figure 4.4: (A) Spectral diffusion of mode 2 in acetone. Note that both compounds display a decay which is best fit by a biexponential decay. (B) Spectral diffusion of mode 2 in DMF. Note that only the dendrimer is best fit with a single exponential decay. (C) Spectral diffusion of mode 2 in CH_3CN. Note that neither data series are best fit by a biexponential decay on our experimental timescale. 77

Figure 4.5: FTIR spectrum of $[Fe(\mu\text{-ethanethiol})(CO)_3]_2$ in hexanes. The double peak near 2070 cm^{-1} is due to a frequency difference of mode 1 in the two isomers, as are the four modes between 1980-2000 cm^{-1}. The axial-equatorial and equatorial-equatorial conformations are depicted to the right. 79

Figure 4.6: Molecular conformations for the dendrimer in acetonitrile, acetone, and toluene. Acetone and toluene show very similar conformations, but even at the low generation number of the dendrimer the conformation in acetonitrile is much more compact than in acetone or toluene. This is in good agreement with the previously

published work on the conformation of poly(aryl ether) dendrimers in good and poor solvents. 80

Figure 5.1: Molecular structures of the three diiron hexacarbonyl compounds tested in this study and infrared spectra of their carbonyl stretching vibrations. In [Fe(μ-S)$(CO)_3$]$_2$ the vibrational band at ~ 2005 cm^{-1} arises from two degenerate modes which are not degenerate in either of the other compounds. All data was collected in hexadecane solvent 97

Figure 5.2: Spectra shown are coherence maps depicting the intensity of oscillatory features during t_2 by their frequencies of excitation and detection. (A) 71-73 cm^{-1} frequency in the rephasing spectra of xyl. The difference frequency of mode 1 and mode 4 in xyl is 72 cm^{-1}, and a 72 cm^{-1} oscillatory feature is expected on the (ω_1=mode 1,ω_3=mode 4) cross peak and its conjugate in rephasing spectra. (B) 36-39 cm^{-1} frequency in the rephasing spectra of xyl. The difference frequency of mode 1 and mode 2 in xyl is 37 cm^{-1}, and that difference frequency is expected on the (ω_1=mode 1,ω_3=mode 2) cross peak and its conjugate in rephasing spectra. A 37 cm^{-1} frequency is not expected on the (ω_1=mode 1,ω_3=mode 4) cross peak or its conjugate. (C) 80-83 cm^{-1} frequency in the nonrephasing spectra of edt. The difference frequency of mode 1 and mode 4 in edt is 82 cm^{-1}, and a 82 cm^{-1} oscillatory feature is expected on the (ω_1=mode 1,ω_3=mode 1) and (ω_1=mode 4,ω_3=mode 4) in nonrephasing spectra. (D) 28-31 cm^{-1} frequency in the nonrephasing spectra of edt. The difference frequency of mode 2 and mode 3 in edt is 30 cm^{-1}, and that difference frequency is expected on the (ω_1=mode 2,ω_3=mode 2) and (ω_1=mode 3,ω_3=mode 3) peaks in the nonrephasing spectra. A 30 cm^{-1} frequency is not expected on the (ω_1=mode 2,ω_3=mode 3) cross peak. 98

Figure 5.3: Spectra shown are coherence maps depicting the intensity of oscillatory features during t_2 by their frequencies of excitation and detection. All coherence maps are from rephrasing spectra. (A) 41-43 cm^{-1} frequency in edt. The difference frequency of mode 1 and mode 2 in edt is 42 cm^{-1} and the difference of modes 2 and 4 is almost the same. A 42 cm^{-1} oscillatory feature is unexpected on the (**1**, **4**)

cross peak. (B) 36-39 cm^{-1} frequency in xyl. The difference frequency of mode 1 and mode 2 in xyl is 37 cm^{-1}, and the difference of mode 2 and 4 is almost the same. A 37 cm^{-1} frequency is unexpected on the (**1**, **4**) cross peak and its conjugate. (C) 36-38 cm^{-1} frequency in the spectra of S_2. The difference frequency of mode 1 and mode 2 in S2 is 37 cm^{-1} and the difference of modes 2 and 4 is almost the same. An oscillatory frequency of 37 cm^{-1} is unexpected for the (**1**, **4**) cross peak and its conjugate. (D) 28-31 cm^{-1} frequency in the rephasing spectra of edt. The difference frequency of mode 2 and mode 3 in edt is 30 cm^{-1}. A 30 cm^{-1} frequency is unexpected on the (**2**, **5**) cross peak. 99

Figure 5.4: Spectra shown are coherence maps depicting the intensity of oscillatory features during t_2 by their frequencies of excitation and detection. All data are from nonrephrasing spectra. (A) 36-38 cm^{-1} frequencies in S_2. The difference frequency of mode 1 and mode 2 in S_2 is 37 cm^{-1} and the difference of modes 2 and 4 is almost the same. A 37 cm^{-1} oscillatory feature is unexpected on any cross peak. (B) 51-53 cm^{-1} frequency in S_2. The difference frequency of mode 2 and mode 5 in S2 is 52 cm^{-1}. A 52 cm^{-1} frequency is unexpected on any cross peak. (C) 35-39 cm^{-1} frequency in the spectra of xyl. The difference frequency of mode 1 and mode 2 in S_2 is ~37 cm^{-1} and the difference of modes 2 and 4 is almost the same. An oscillatory frequency of 37 cm^{-1} is unexpected on any cross peak. (D) 41-43 cm^{-1} frequency in the spectra of edt. The difference frequency of mode 2 and mode 4 in edt is 42 cm^{-1}. A 42 cm^{-1} frequency is unexpected on any cross peak. 100

Figure 5.5: Top) Liouville diagrams associated with the rephasing pulse sequence, Middle) Liouville diagrams associated with the nonrephasing pulse sequence, and Bottom) Liouville pathways for both pulse sequences with t_2 oscillatory features. These pathways, where the system evolves in a coherent superposition of states during t_2, contribute to cross peaks in rephasing spectra, and to diagonal peaks in nonrephasing spectra. 102

Figure 5.6: Depiction of the molecular and laboratory frame in which the orientational response is calculated. The laboratory frame is defined by axes x, y, and z, and the

molecular frame is defined by axes a, b, and c. The relative orientation of the two frames of reference is given by the Euler angles α, β, and γ. For convenience the molecular transition dipole moments, all of which are orthogonal in this work, are taken to lie along each of the molecular axes, and the experimental electric fields are polarized along the three laboratory axes. 106

Figure 5.7: Potential Liouville pathways for the nonrephasing cross peak oscillations. In the cartoon 2D spectra orange circles represent peaks to which the Liouville diagrams above the spectra will contribute. (A) t_1 and t_3 coherence transfer. If the two states during t_3 have orthogonal transition dipole moments only one will contribute to the measured response. (B) Population-to-coherence transfer pathway. (C) Coherence-to-population pathway. The spectral features of (B) and (C) are comparable. All three of the example Liouville pathways contribute a single oscillatory frequency to both a diagonal peak and a cross peak. 108

Figure 5.8: Potential Liouville pathways for three of the anomalous rephasing cross peak frequency components. (A) Coherence-to-population transfer pathway contributing to the excited-state absorption of the (**4**, **1**) and (**2**, **1**) cross peaks which oscillates at the (**2**, **1**) difference frequency. (B) Coherence-coherence transfer pathway contributing to the (**1**, **4**) and (**1**, **5**) cross peaks and oscillating at the (**1**, **4**) and (**1**, **5**) difference frequencies. (C) Coherence-coherence transfer pathway contributing to the (**1**, **4**) cross peak and oscillating at the (**1**, **4**) and (**1**, **6**) difference frequencies. 109

Figure 5.9: (A) Coherence maps of xyl highlighting the 88-89 cm^{-1} frequency in rephasing data. Peak amplitude data for the (**4**, **1**) cross peak and the Fourier transform of the peak amplitude are shown, illustrating three frequency components at ~ 38, 73, and 88 cm^{-1}. (B) Coherence maps of the disulfide highlighting the 85-87 cm^{-1} frequency. Peak amplitude data for the (**4**, **1**) cross peak and the Fourier transform of the peak amplitude are shown, illustrating three frequency components at ~ 38, 78, and 86 cm^{-1}. 110

Figure 6.1: (A) A biomimetic model of the [FeFe]-hydrogenase active site and FeS cluster. This biomimetic compound has been shown to display reversible redox chemistry, redox-dependent isomerization, and the formation of metal hydrides, all of which produce marked changes in the carbonyl vibrational bands. (B) Photosensitized diiron hexacarbonyl catalyst for the formation of H_2. The small organic photosensitizer makes this system easily tractable for computational studies as well as experimental work. 122

Figure 6.2: A modified cytochrome c protein where the heme group has been replaced with a biomimetic diiron hexacarbonyl core. This artificial enzyme has been shown to be a modest catalyst for the production of H_2 in aqueous media. 124

Figure A1: Inhomogeneity decay of mode 2 in $[Fe(\mu\text{-}S)(CO)_3]_2$ and the dendrimer in chloroform 130

Figure A2: Inhomogeneity decay of mode 2 in $[Fe(\mu\text{-}S)(CO)_3]_2$ and the dendrimer in THF 131

Figure A3: Inhomogeneity decay of mode 2 in $[Fe(\mu\text{-}S)(CO)_3]_2$ and the dendrimer in toluene 131

Figure A4: Decay of the nonrephasing peak amplitude of mode 2 in $[Fe(\mu\text{-}S)(CO)_3]_2$ and the dendrimer in chloroform 132

Figure A5: Decay of the nonrephasing peak amplitude of mode 2 in $[Fe(\mu\text{-}S)(CO)_3]_2$ and the dendrimer in THF 132

Figure A6: Decay of the nonrephasing peak amplitude of mode 2 in $[Fe(\mu\text{-}S)(CO)_3]_2$ and the dendrimer in toluene 133

List of Abbreviations

IR: infrared

2D: two-dimensional

2D-IR: two-dimensional infrared

^{3}MLCT: triplet metal-to-ligand charge transfer

AcN: acetonitrile

BCT: (benzene)$Cr(CO)_3$

bpy: bipyridine

CO: carbonyl

DMDC: dimanganese decacarbonyl

DMF: N,N'-dimethylformamide

DPPFCr: [(1,1'-bis(diphenylphosphino)ferrocene)chromium$(CO)_4$]

edt: 1,2-ethanedithiolate

FFCF: frequency-frequency autocorrelation function

FMO: Fenna-Matthews-Olsen

FTIR: fourier-transform infrared

IVR: intramolecular vibrational relaxation

MOF: metal-organic framework

NMR: nuclear magnetic resonance

pdt: 1,3-propanedithiolate

phen: phenanthroline

ps: picosecond

RDC: $Rh(CO)_2$(acetylacetonato)

THF: tetrahydrofuran

xyl: o-xylyldithiolate

Abstract

Ultrafast two-dimensional infrared (2D-IR) spectroscopy is used in this work to study the vibrational dynamics of a series of biomimetic catalysts. We set out to investigate the vibrational dynamics of catalytic compounds in systems directly relevant to molecular reactivity, specifically reactive oxidation states, catalytically relevant self-isomerizations, dendritically-induced nano-confinement, and excitonic coherence transfer. For most of the work performed for this thesis we used diiron hexacarbonyl small-molecule mimics of the [FeFe]-hydrogenase enzyme's active site.

The vibrational dynamics of [(1,1'-bis(diphenylphosphino)ferrocene)chromium-$(CO)_4$] (DPPFCr) in its neutral, closed-shell state were compared to the vibrational dynamics of DPPFCr as a cation radical. This comparison is possible because molecular oxidation does not significantly change the vibrational displacements of the carbonyl modes, which are studied here. Molecular oxidation induces an acceleration of the vibrational relaxation of the carbonyl modes but does not significantly affect the spectral diffusion dynamics of the carbonyl groups. We attribute this to an idiosyncrasy of the non-interacting solvent used for the experiment, CH_2Cl_2, which was chosen specifically for the weak nature of its solvent-solute interactions.

Unexpectedly pronounced and slow spectral diffusion in the carbonyl modes of (μ-pdt)$[Fe(CO)_3]_2$ (pdt = 1,3-propanedithiolate) was observed in alkane solvents. The contribution of solvent-solute interactions in alkane solvents to spectral diffusion is expected to be minimal, and we related the spectral diffusion to fluctuations of the carbonyl potential induced by a catalytically-relevant mode of molecular fluxionality in (μ-pdt)$[Fe(CO)_3]_2$. Comparison with a different diiron hexacarbonyl compound, (μ-edt)$[Fe(CO)_3]_2$ (edt = 1,2-ethanedithiolate), effectively ruled out isomerization of the bridging organic disulfide group, and a Boltzmann distribution of states derived from electronic structure calculations supported our hypothesis by suggesting that a significant

distribution of molecular conformations were present in at room temperature. Other fluxional organometallic complexes $M_3(CO)_{12}$ (M=Ru, Os) displayed similar spectral diffusion. This is the first use of spectral diffusion to study molecular conformational flexibility. We also observed an unexpected dependence of the rate of intracarbonyl IVR on the chain length of the alkane solvent.

Nano-confinement has been reported on several occasions to favorably modulate the reactivity of diiron hexacarbonyl compounds, and dendritic assemblies with diiron hexacarbonyl cores were synthesized and the vibrational dynamics of the carbonyl groups were compared to the vibrational dynamics of carbonyls on similar diiron hexacarbonyl compounds without dendritic groups. Slower IVR and an additional timescale of spectral diffusion were observed in dendritic assemblies, which are hypothesized to reflect nano-modulation of the carbonyl group's first solvation shell by the dendritic groups.

Three diiron hexacarbonyl compounds with differing bridging disulfide groups (edt, pdt, and o-xylyldithiolate) are found to display unusual modulations of cross peak intensity which have previously been identified as spectral signatures of vibrational coherence transfer. Specific modulations of cross peak amplitude are observed in all three compounds, suggesting that certain coherence transfer events are common in diiron hexacarbonyl compounds, and an oscillatory frequency resulting from coherence transfer between bright and dark vibrational modes is identified.

Chapter 1
Introduction

1.1 Introduction

Traditional chemical catalysis employs relatively small compounds to accelerate the kinetics of chemical reactions. Living organisms perform the same function using enzymes, complex macromolecules which are often catalytically superior to comparable small-molecule catalysts. The catalytic superiority of enzymes over small-molecule catalysts is due to a number of reasons, including the restriction of solvent-access to the active site, lowered reorganizational energy barriers, and fine-tuning of the enzyme scaffold to participate in the reaction.[1-3] Many chemists have attempted to optimize the performance of small-molecule catalysts by incorporating elements of these biochemical factors into their catalyst design. Such research is known as biomimetic chemistry, and biomimetic design has been repeatedly shown to modulate and enhance the reactivity of small-molecule systems.[4-10]

Some good examples of biomimetic design include creating restrictive nano-environments for the catalysts to mimic the solvent restriction of a protein scaffold and modeling small molecule catalysts directly after enzyme active sites. Designing nano-confining environments for small-molecule active sites has become a central theme in biomimetic chemistry, and molecular confinement has been clearly shown to modulate the reactivity of chemical systems ranging from cyclodextrins to dendrimers.[5, 8, 11] Imitation of enzyme active sites has also been attempted, and one of the best examples of active-site mimicry in biomimetic chemistry is the work to replicate the chemical reactivity of the bacterial hydrogenase enzyme.[7, 12] In the hydrogenase enzyme chemical reactivity has been directly linked to a mode of ligand fluxionality, and biomimetic small-molecule catalysts inspired by the hydrogenase enzyme active site have shown a similar dependence of

reaction rate on the dynamic fluxionality of the carbonyl ligands. In many respects the hydrogenase enzyme and small molecule mimics of the hydrogenase enzyme active site are excellent examples of the role of nano-environmental constraint and ligand fluxionality in chemical reactivity.

Enzymes are large and complex macromolecules, and modifying small-molecule catalysts to incorporate the physical and chemical factors which contribute to the reactivity of an enzyme requires some understanding of the dynamical contributions of the enzyme scaffold to the overall reaction. One method for catalyst optimization is the empirical strategy of iteratively identifying and building upon whatever modifications are successful. A different approach is to identify the chemical and physical factors which directly contribute to chemical reactivity so that they may subsequently be incorporated into a small-molecule's design. In this work we adopt the latter approach and use two-dimensional infrared spectroscopy (2D-IR) to probe the dynamics of biomimetic small molecules and characterize key dynamical features which contribute to chemical reactivity, focusing primarily upon the role of conformational flexibility, redox processes, steric constraint on the nano-environment, and the presence of quantum coherences.

1.2 Hydrogenase enzyme and Active-Site Mimics

To clearly introduce the hydrogenase enzyme, its relevance must first be explained. Modern industrial production of molecular hydrogen is typically performed using a process known as steam reformation.[15] In this reaction natural gas or some other hydrocarbon is mixed with superheated steam and substantial amounts of H_2 and CO_2 are formed. CO_2 is a greenhouse gas, and it has been clearly implicated as a primary contributing factor to anthropogenic climate change.[16-17] An alternate method for the industrial production of hydrogen gas, one which does not create greenhouse gases as a byproduct, would be a notable achievement in the movement towards a sustainable and environmentally-conscious global economy.

A number of alternative methods for hydrogen production have been proposed, including electrolytic and photochemical water-splitting. Electrolytic water splitting occurs when a current is applied to an electrode submerged in an aqueous solution, splitting the

water into molecular dihydrogen and dioxygen. Photochemical hydrogen production refers to the photochemically-driven splitting of water into hydrogen and oxygen gas by a molecular catalyst. Both of these methods catalyze the transformation of one of the most abundant compounds on earth into dihydrogen without the creation of any environmentally undesirable byproducts. Unfortunately, both methods also suffer from significant drawbacks. Electrochemical water splitting is not as cost-effective as hydrocarbon-based methods, and the best catalyst to date is platinum, which is rare and expensive.[18] Photochemical hydrogen production has been known in principle for some time, but the field is not developed enough to rival the mainstream hydrocarbon-based methods.[19]

Some natural organisms, however, have solved the problem of hydrogen production, and perform the splitting of water and its reformation from hydrogen and oxygen using hydrogenase enzymes with active sites composed of iron, nickel, or a combination of the two.[7, 12] Not only do these enzymes employ earth-abundant elements in their catalysis, but the enzymes are highly efficient and display high turn-over numbers.

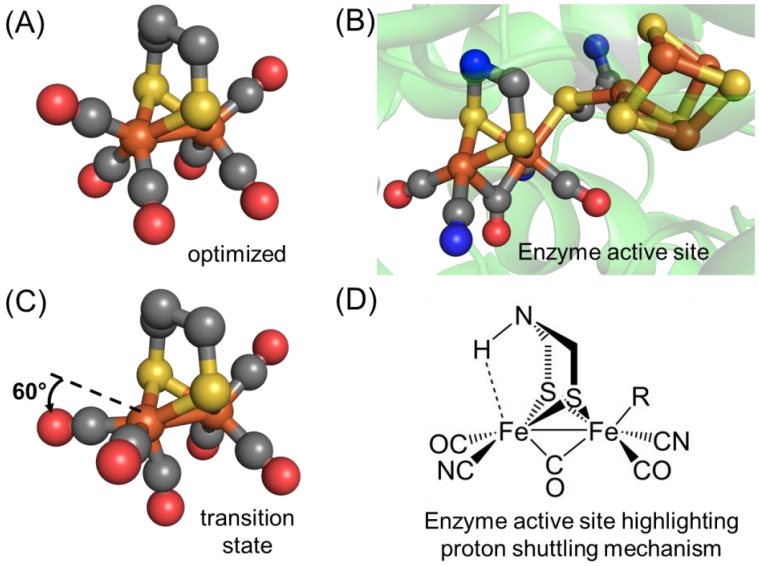

Figure 1.1: (A) (μ-pdt)[Fe(CO)$_3$]$_2$ (pdt =1,3-propanedithiolate), an archetypical [FeFe]-hydrogenase enzyme active site mimic. (B) [FeFe]-hydrogenase active site. (C) Molecular geometry of (μ-pdt)[Fe(CO)$_3$]$_2$ in the transition-state of the turnstile carbonyl isomerization, where the carbonyl ligands are rotated ~ 60° from the ground state geometry. Note the similarity of the turnstile transition state of (μ-pdt)[Fe(CO)$_3$]$_2$ to the geometry of the hydrogenase enzyme active site, especially the exposed iron atom. (D) Diagram of the proposed proton-shuttling mechanism in hydrogenase enzyme active site. The direct accessibility of the iron atom is significant to the formation of a reactive terminal hydride.

Unfortunately, they are highly air-sensitive, and this has precluded their active industrial application. However, the message of the enzymes is clear: if nature has found a way to rapidly and efficiently split water using an iron-based catalyst, it should be possible for an artificially-engineered catalyst to do the same. To meet this challenge much effort has been invested in attempting to elucidate the exact physical and chemical principles exploited by the enzymes, and in attempting to create a robust mimic of the enzyme for industrial application. At this time there has been some success in the effort, but the work is ongoing.[7-8, 10, 20-25]

Though there are many promising variants of the hydrogenase enzymes, we focus here upon a specific class of compounds designed to mimic the diiron hydrogenase enzyme's active site. The central chemical motif of these compounds is a diiron hexacarbonyl core with bridging sulfide ligands and one of such compound, (μ-pdt)$[Fe(CO)_3]_2$ (pdt =1,3-propanedithiolate), is shown in Figure 1.1A.[25] The sulfide groups are typically bridged by an organic group which may be altered to modulate the chemical reactivity and dynamics of the molecule. Substitution of one or more carbonyl ligands with phosphines to electronically enrich the diiron molecular core or with cyanides (to better mimic the enzyme active site) is common,[26-29] but the hexacarbonyl motif has remained widely used in model compouds.

In 2001 Lyon et. al. studied the rates of ligand substitution reactions in several diiron hexacarbonyl compounds and found that the rates of cyanide substitution on the diiron core showed a correlation with the activation energy of a turnstile-type rotation of the carbonyl groups on each iron atom around the Fe-Fe bond axis. The transition state of this isomerization is shown in Figure 1.1C.[13] Lyon et. al. proposed that the ligand substitution reaction involved nucleophilic attack during the turnstile carbonyl isomerization, as shown in Figure 1.2A, and noted a similarity between the geometry of the [FeFe]-hydrogenase active site and the geometry of the diiron hexacarbonyl compounds in the turnstile isomerization transition state.[12-13, 30-32] This similarity is illustrated in Figure 1.1, where both the transition state of the turnstile isomerization and the active site of hydrogenase enzyme feature a carbonyl group which is at least quasi-bridging and an exposure of one iron atom beneath the bridging disulfide ligand.

Modulation of chemical reactivity by intramolecular fluxionality or molecular flexibility is nothing new to organometallic catalysis,[33-35] but the biochemical relevance of the diiron hexacarbonyl motif has brought the fluxionality of the carbonyl ligands in this

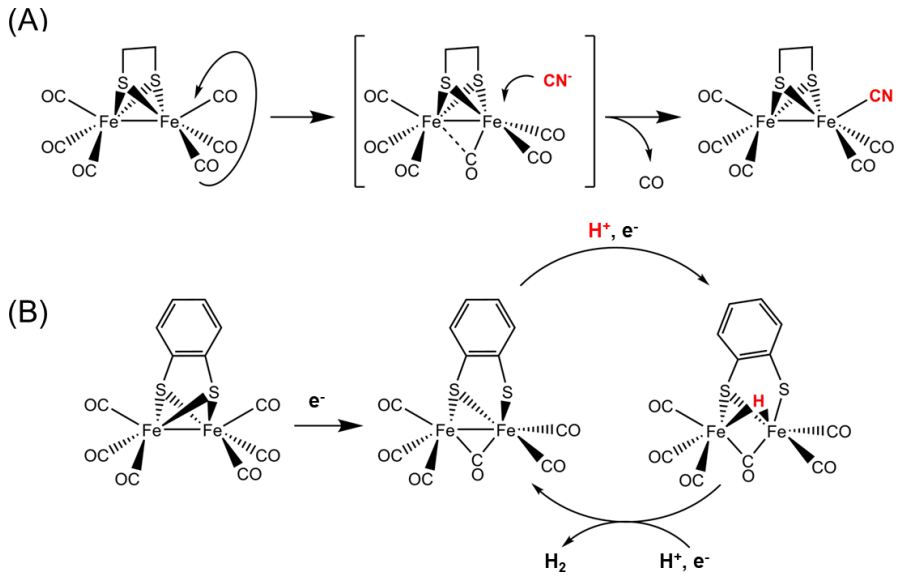

Figure 1.2: (A) Reaction mechanism proposed by Lyon et. al. for the nucleophilic substitution of CO by cyanide in (μ-edt)[Fe(CO)$_3$]$_2$ (edt =1,2-ethanedithiolate). The reaction is initiated by a turnstile-type isomerization of the carbonyl groups on one iron atom and nucleophilic substitution occurs in the transition state of the carbonyl isomerization.[13] (B) Reaction mechanism proposed by Felton et. al. for the electrochemical production of H_2 by (μ-bdt)[Fe(CO)$_3$]$_2$ (bdt =1,2-benzenedithiolate). The catalyst is prepared by reduction of (μ-bdt)[Fe(CO)$_3$]$_2$ and a bridging hydride is formed as a key intermediate in the catalytic mechanism.[14] Both of these mechanisms involve a turnstile-type reorganization of the carbonyl groups on one of the iron atoms.

class of compounds significant attention. Subsequent studies have underscored the significance of the turnstile mode of fluxionality to the reaction mechanisms compounds with a biomimetic diiron core, including C≡O ligand migration and molecular redox chemistry.[36-40] The redox processes of biomimetic diiron complexes have been the subject of significant investigation due to their perceived potential as hydrogen-activating and proton-reducing catalysts. Redox processes in biomimetic diiron complexes are highly dependent upon the ligands in the first coordination sphere of the diiron core, but most of the proposed mechanisms involve a bridging hydride and a redox-induced re-organization of the first coordination sphere of the diiron core which often includes a turnstile rotation of the non-bridging ligands.[14, 41-43] An example of this is shown in Figure 1.2B, where the mechanism of electrochemical H_2 production by (μ-bdt)[Fe(CO)$_3$]$_2$ (bdt

= 1,2-benzenedithiolate) is shown. Here molecular reduction breaks one of the bridging sulfide bonds and induces a turnstile rotation of the carbonyl groups on one iron, causing the formation of a bridging carbonyl group. Additional reduction and protonation of (μ-bdt)$[Fe(CO)_3]_2$ create a bridging hydride which reacts with a proton donor upon additional reduction to create H_2.[14]

While conformational mobility of the first coordination sphere plays a crucial role in the reactivity of this class of biomimetic diiron compounds, there are other factors which are known to enhance its catalytic efficiency. Modulation of chemical reactivity by nanoconfinement has been reported in multiple diiron hexacarbonyl reaction systems, including cyclodextrins,[44] polymers,[21, 45] and dendrimers.[22] Darensbourg's group reported a cyclodextrin-diiron hexacarbonyl host-guest complex,[46] and subsequent study by Cheng et. al showed that the host-guest complex outperformed the unencapsulated guest as a photochemical catalyst for the production of H_2 in aqueous media.[44] Covalent attachment of a diiron pentacarbonyl compound to poly(acrylic acid) and simple addition of chitosan to a reaction mixture catalyzed by a biomimetic diiron hexacarbonyl led to excellent catalytic production of H_2.[21, 45] Both groups attributed the catalytic performance of their system to a polymeric modulation of the catalyst's nano-environment. Similarly, a poly(aryl ether) dendrimer with a biomimetic diiron hexacarbonyl core showed exceptional catalytic production of H_2 which increased with the generation of the poly(aryl ether) dendrimer, suggesting a positive modulation of the catalytic process by the nano-environment induced by the dendrimer.[22]

Diiron hexacarbonyl mimics of the hydrogenase enzyme active site are thus exceptionally promising compounds for biomimetic investigation. They represent a catalytically relevant system where the dynamic interplay between ligand fluxionality, nanoconfinement, and chemical reactivity is widely recognized, easily tunable, and as-yet incompletely understood, and where insight gathered from the small-molecule biomimics may be directly compared to the chemical reactivity and dynamics of the hydrogenase enzyme active site. Fortuitously, this class of compounds invariable contains carbonyl

ligands, whose strong vibrational bands in the mid-IR are ideal probes for spectroscopic investigation.

1.3 Metal Carbonyls and Two-Dimensional Infrared Spectroscopy

All organic and organometallic compounds have vibrational frequencies in the mid-IR. Most vibrations of organic and organometallic functional groups lie in the frequency

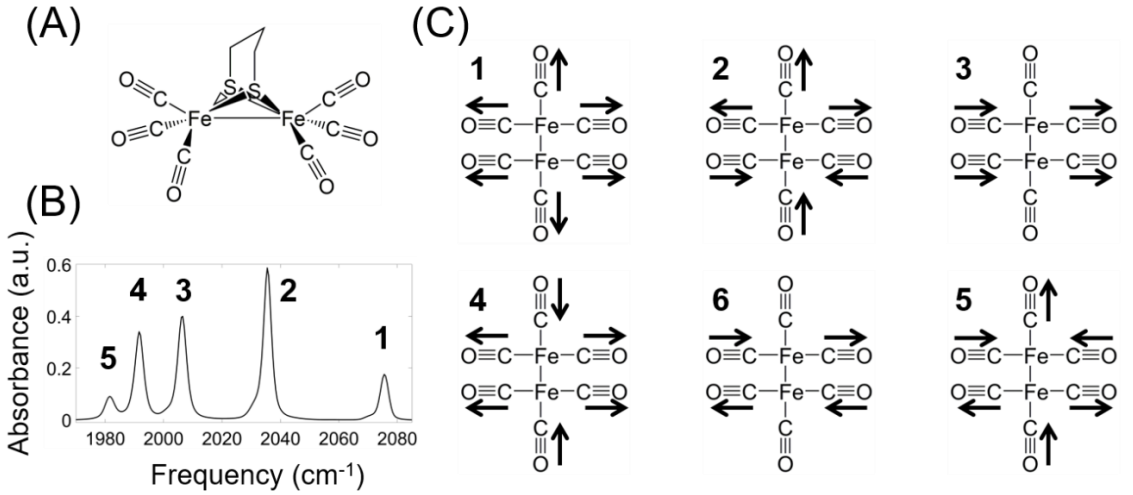

Figure 1.3: (A) (μ-1,3-propanedithiolate)[Fe(CO)$_3$]$_2$, an archetypical [FeFe]-hydrogenase enzyme active site mimic. (B) Infrared spectrum of the carbonyl vibrational modes of (μ-1,3-propanedithiolate)[Fe(CO)$_3$]$_2$ in hexane, with vibrational frequencies numbered from highest to lowest. (C) Atomic displacements for the carbonyl vibrations of the diiron hexacarbonyl molecules used in this work. Vibrational modes are numbered from highest to lowest frequency, corresponding to the numbering of the spectrum in (B), and are referred to by their numbering scheme in the remainder of this work. Mode 6 is not IR active.

ranges of 10-1800 cm^{-1} and 2800-3600 cm^{-1},[47] and the vibrational spectrum of a molecule or of a mixture contains rich information on not only what functional groups are represented in the sample but also on the molecular environment experienced by those functional groups. One chemical group with highly distinct vibrational frequencies is a carbon monoxide bonded to a transition metal atom. Such complexes are known as metal carbonyls, and their vibrational frequencies lie between 1900-2300 cm^{-1}.[48-51] Very few other vibrational frequencies lie in this region of the infrared spectrum, which makes metal carbonyl vibrations ideal for diagnostic use, since their peaks are rarely convoluted by other vibrations and are easy to identify. Carbon monoxide bonds to transition metal atoms in two bonding modes. The first is by donating electron density to the metal atom through

the carbon's σ molecular orbital, which is known as σ-donation. The second is by receiving electron density from the metal's d-orbitals into the carbon monoxide's π*-antibonding orbital, which is known as π-backbonding. Both bonding forms occur, but π-backbonding has the greatest effect upon the frequency of the carbonyl vibration – increased occupancy of the π*-antibonding orbital weakens the carbon-oxygen bond, and red shifts the frequency of the corresponding vibration.[48-54] This relationship causes changes in the electronic structure of the metal or in the bonding mode of the carbonyl to be directly reflected in its frequency, which in turn greatly augments the capacity of a carbonyl stretch's use as a diagnostic standard. Metal carbonyl vibrations are convenient for infrared spectroscopic study because of the strength of the carbonyl stretching modes. In diiron hexacarbonyl mimics of the hydrogenase enzyme active site the carbonyl stretching modes form a distinctive pattern in the IR, which is exemplified in Figure 1.2. The highest frequency mode corresponds with a completely symmetric vibration in which all six carbonyls are equally displaced. The second highest frequency mode corresponds to a symmetric stretching of all of the carbonyl groups, but the carbonyl groups attached to each Fe atom are displaced out of phase with the carbonyl groups on the other Fe atom by π radians. It is on these two vibrational modes that we focus our study; these two modes have relatively strong vibrations and are reasonably spectrally isolated even in a wide variety of solvents and chemical modifications. The frequencies of the other vibrational modes tend to broaden and overlap in all but the most nonpolar solvents, making it difficult to analyze them without ambiguity. The strength of the carbonyl vibrations in this class of molecule and their relative abundance makes them ideal for use as probes in spectroscopic investigations, specifically for nonlinear spectroscopy such as two-dimensional infrared spectroscopy (2D-IR).

1.4 Experimental Details and Experimental Observables

1.4.1 Experimental Set-up.

Two-dimensional infrared spectroscopy is a nonlinear third-order process where a sequence of three experimental pulses interact with the sample to produce a third-order response which is Fourier-transformed to create a 2D spectrum. The geometry of our

pulse sequence and its time-dependent components are depicted in Figure 1.3. Our experimental set-up begins with a regeneratively amplified titanium:sapphire laser system

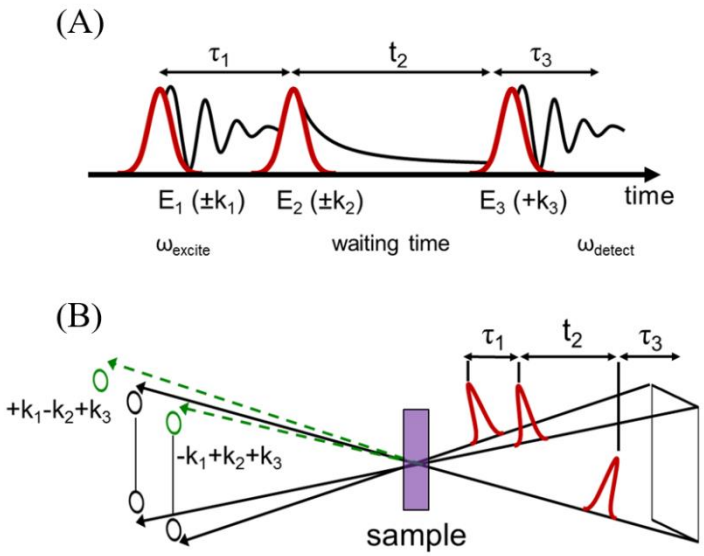

Figure 1.4: (A) Depiction of the experimental pulse sequence, with pulses $\mathbf{k_1}$, $\mathbf{k_2}$, and $\mathbf{k_3}$, and the time intervals between them, t_1, t_2, and t_3. (B) Depiction of the spatial alignment of the three pulses in a box geometry and the background-free direction of the signal field.

which produces experimental pulses of ~ 1 mJ energy and 100 fs bandwidth with a center frequency of 800 nm and a 1 kHz repetition rate. A white light continuum is generated from a YAG crystal with these pulses, and the white light continuum is mixed with the output of the regenerative amplifier on two crystals of β-barium borate (BBO). Although only a single BBO would be required for this experimental set-up, the addition of a second BBO allows independent tuning of the excitation and detection frequencies for the subsequent experiment. The output of each BBO is difference-frequency mixed on a GaSe crystal (referred to here as a DFG) to produce experimental pulses centered at 2000 cm^{-1}, although the pulse frequencies are adjustable and are typically tuned to the optimal frequency for which system is being studied. The output of each DFG is split into two pulses, creating four in total. Three of these are overlapped on the sample cell in a box geometry, where the pulses are directed onto the sample from three different directions, forming together three of the four vertices that would define a square. The fourth pulse is directed around the sample for later use as a local oscillator. The three pulses which interact with the sample and the time delays after each are traditionally denoted as $\mathbf{k_1}$-$\mathbf{k_3}$ and t_1-t_3,

respectively. The first two pulses, $\mathbf{k_1}$ and $\mathbf{k_2}$, vibrationally excite all of the modes within the pulse's bandwidth, and the third pulse, $\mathbf{k_3}$, acts as a detection pulse to generate the signal field, which radiates in a background-free direction. The signal field is overlapped with the local oscillator and both are upconverted into visible frequencies on a Mg-doped lithium niobate crystal (LiNbO3) using a highly chirped pulse from the regenerative amplifier.[55] The upconverted signal field is then steered into the spectrometer and detected on a 1340 x 100 CCD array which is synchronized to the 1 kHz repetition rate of the laser. To create a 2D spectrum the time delay between $\mathbf{k_1}$ and $\mathbf{k_2}$ is scanned and Fourier transformed to generate the excitation axis, and the detection axis is read directly from the spectrometer. The time resolution of the 2D experiment is controlled by stepping t_2 and measuring a 2D spectrum at each desired waiting time. We collect two sets of 2D-IR data, which are referred to as "rephasing" and "nonrephasing" spectra. The difference between the two sets arises from differing experimental pulse sequences, which are defined as $-\mathbf{k_1}+\mathbf{k_2}+\mathbf{k_3}$ and $+\mathbf{k_1}-\mathbf{k_2}+\mathbf{k_3}$ for the rephasing and nonrephasing pulse sequences, respectively.[56] Here the first pulse to interact with the sample is swapped in the two sequences while $\mathbf{k_3}$ is the third pulse to interact with the sample in both the rephasing and nonrephasing sequences. The resulting data set consists of a set of time-ordered 2D spectra, and contains a wealth of chemical and dynamical information, among which are the timescales of vibrational relaxation, energy randomization/IVR, and spectral diffusion, each of which will be discussed in detail below.

1.4.2 Vibrational Relaxation.

The relaxation of a vibrational mode refers to the time-dependent dissipation of the mode's vibrational energy into that vibration's bath modes.[57-58] These bath modes are typically other vibrational modes of the same molecule, solvent modes of comparable frequency, or low-frequency phonon modes of the solvent.[59-60] A vibration which is strongly coupled to its bath modes will typically relax much faster than a similar mode which is more weakly coupled to its bath modes, and the relaxation of a vibrational mode may in principle contain a significant amount of information regarding the molecule and its molecular environment. In practice, this information is often difficult to unambiguously interpret due to the large number of contributing factors.[60-62] The timescales of vibrational

relaxation vary greatly from system to system and may range from several picoseconds[63] to hundreds of picoseconds.[64] In most of the systems studied here the vibrational relaxation tends to take place of the timescale of 30-80 ps, and the decay of a peak's amplitude is typically well fitted by a sum of two or more exponential decays. In many cases one of these decays is significantly faster than the other, and this is considered to represent a fast IVR process, while the slower timescale is interpreted as arising from the dissipation of the vibrational energy into the bath modes of that vibration.[26, 61-62, 65-66]

1.4.3 Cross Peaks and IVR.

Cross peaks in a 2D spectrum represent vibrational energy which was excited at one frequency and detected at another. This typically arises from one of two scenarios. The first is a scenario of chemical exchange, where the state of the system and its corresponding vibrational structure was altered between the excitation and detection pulses.[56, 67-68] The second scenario is that of multiple vibrations which share a ground state. Where this is the case, cross peaks between such vibrations are observed in the 2D spectra and the dynamics of those cross peaks reflect the process of fast energy randomization between those vibrational modes after excitation.[26, 56, 65, 69-70] While this process is a stochastic randomization of vibrational energy and distinct in some ways from the cascade of vibrational energy into lower-frequency bath modes which is traditionally referred to as IVR, it is in fact part of the initial phase of the IVR process,[58] and the two terms are sometimes used interchangeably in 2D-IR spectroscopy.[65] One common way to extract the timescale of this process is to divide the amplitude of the cross peak by the amplitude of the diagonal peak at the same detection frequency.[65, 71] Since the cross peak represents vibrational excitation of the same mode as that on the diagonal, the operation of division cancels out all the timescales shared by both peaks and isolates the timescales in which the dynamics of the two peaks are different. These timescales are considered to represent the dynamics of energy randomization between modes which share a ground state.

To illustrate this operation, consider a system of two strongly coupled vibrational modes, **a** and **b**, where the vibrational relaxation of a may be fit to the sum of two exponential functions, one of which decays much faster than the other. The cross peak excited at **b** and detected at **a** will also be well fit by two exponential functions, one of

which is also much faster than the other. The ratio of these two fits is shown in Equation 1.1,

$$\frac{AC(t)}{AD(t)} = \frac{a * e^{-\left(\frac{t_2}{m}\right)} + b * e^{-\left(\frac{t_2}{n}\right)}}{c * e^{-\left(\frac{t_2}{p}\right)} + d * e^{-\left(\frac{t_2}{n}\right)}} \tag{1.1}$$

Where *AC* and *AD* are the amplitudes of the cross peak and the diagonal peak, respectively, *m* and *p* are the time constants of the fast decays of the cross peak and diagonal peak, respectively, *n* is the time constant of the slow decay of both peaks, and *a*, *b*, *c*, and *d* are the respectively amplitudes the those fit components. At a large enough waiting time the fast decays will contribute negligibly to the total peak amplitude, leaving only the slow decays, as detailed in Equation 1.2,

$$\lim_{t \to n} \frac{AC(t)}{AD(t)} = \lim_{t \to n} \frac{a * e^{-\left(\frac{t_2}{m}\right)} + b * e^{-\left(\frac{t_2}{n}\right)}}{c * e^{-\left(\frac{t_2}{p}\right)} + d * e^{-\left(\frac{t_2}{n}\right)}} = \frac{b * e^{-\left(\frac{t_2}{n}\right)}}{d * e^{-\left(\frac{t_2}{n}\right)}} = \frac{b}{d} \tag{1.2}$$

Thus, the timescale required for the ratio of cross peak and diagonal peak amplitude to approach a single consistent value is a measure of the timescale in which the fast decay components of both peaks contribute significantly to the amplitude of their respective peaks, and in which both fast decay components are differ from each other. This operation is exemplified in Figure 1.4, where Figure 1.4a depicts model decays of diagonal and cross peak amplitude, and the ratio of the two is shown in Figure 1.4b. In principle, the final

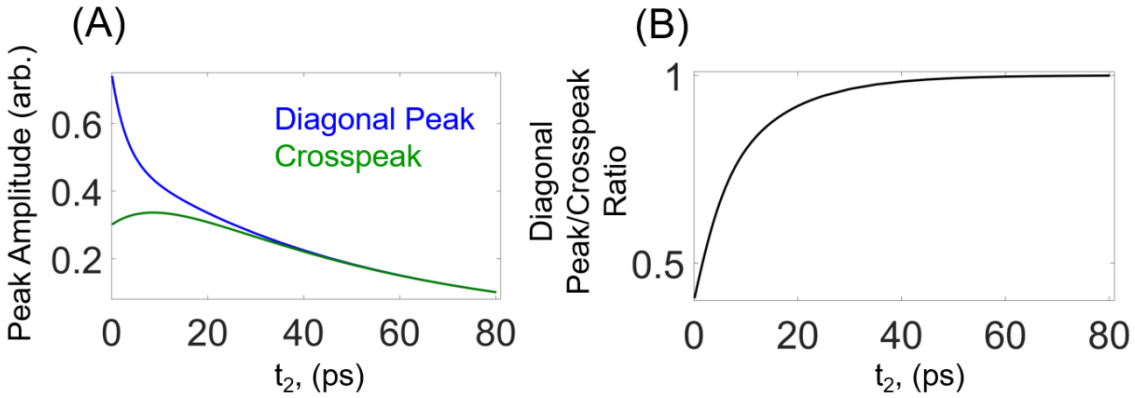

Figure 1.5: (A) Model peak amplitude decays for a diagonal peak, displaying a biphasic monotonic decay of peak amplitude, and a cross peak, displaying an increased in peak amplitude during early waiting times followed by a decrease in in peak amplitude. (B) Ratio of the time-dependent amplitudes of the diagonal and cross peak. The ratio begins to approach a value of one after ~ 40 ps, and visual inspection of 3a will show a corresponding similarity of the diagonal and cross peak on the same timescale.

ratio of the initial amplitudes of the slow decay timescale may contain information relevant to the dynamics of the system, and the mechanism of the self-isomerization of $Fe(CO)_5$ was determined in part through use of this final ratio.[71] However, the independent tuning of our excitation and detection pulses and their finite spectral bandwidth complicates such an analysis, and in this work we limit our focus to the timescale required for the decay of the fast components of the vibrational relaxation, which is in principle unaffected by the tuning of our experimental set-up.

In systems where there are multiple vibrational modes which share a ground state some of the peaks in a 2D spectrum will oscillate as a function of t_2. The positions of peaks with oscillations depend upon the experimental pulse sequence: in rephasing spectra oscillatory features will occur on the cross peaks, and in nonrephasing spectra oscillatory features will be present on diagonal peaks.[56, 72] These oscillatory features will be discussed in greater detail in Chapter 5. We mention them here simply because in most of our 2D data these oscillatory features will be evident at short waiting times, and we emphasize that they arise not from experimental noise but from dynamics intrinsic to the vibrational system and experimental setup.

1.4.4 Spectral Diffusion.

The spectral intensity of a vibrational mode is typically dependent upon its transition dipole moment, but the spectral width of the mode arises from two distinct physical mechanisms, which are referred to the "homogeneous" and "inhomogeneous" broadening of the peak.[73] The homogeneous broadening of a spectral peak depends upon its dephasing timescale –vibrations with long dephasing timescales give rise to very narrow peaks, and vibrations with short dephasing times have much broader peaks. The second type of spectral broadening, inhomogeneous broadening, describes peak breadth which arises from a distribution of peaks with slightly differing center frequencies, each of which with its own homogeneous width. To illustrate this difference, consider a system in which the sample has a single vibrational frequency, and exists in a single microstate. This system is depicted in Figure 1.5a. In this scenario the vibration would have no inhomogeneous broadening, since only one microstate contributes to the peak, and the width of the peak would depend solely on the dephasing time of that microstate. Now consider the same

sample in a different system, one in which the sample exists in a number of different microstates, each of which slightly affects the frequency of the vibration in a different way. This system exhibits both homogeneous and inhomogeneous broadening, and is depicted in Figure 1.5b. The vibrational peak associated with this system, while appearing to be a single peak, is in fact the sum of the peaks associated with each of the system's microstates, each of which is broadened by its own respective dephasing time. Both broadening

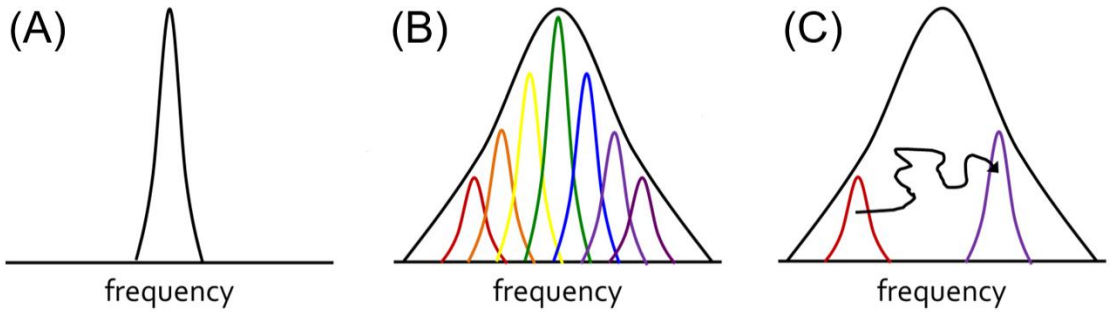

Figure 1.6: (A) A single homogeneously broadened peak, corresponding to the spectral response of a system with a single microstate. (B) A single inhomogeneously broadened peak, corresponding to the spectral response of a system with multiple microstates, each of which with a slightly differing frequency. (C) A fluctuation of frequency within the inhomogeneously broadened system corresponding to a change in microstate experienced by the sample. The timescale required for a system to sample all of its available microstates is described by the frequency-frequency autocorrelation function (FFCF).

mechanisms contain different information about the system – the homogeneous broadening represents the dephasing time of the vibration, and inhomogeneous broadening reflects the inhomogeneity of the system's microstates.

Since the inhomogeneous broadening of a system directly reflects the system's microstates, the dynamics associated with the fluctuations of those microstates are reflected in the timescale required for the system to sample all of the microstates available to it. This process of microstate-sampling is known as "spectral diffusion," and the timescale of a system's spectral diffusion is given by its frequency-frequency autocorrelation function (FFCF).[74-75] The FFCF measures the effect of both inter- and intra-molecular processes on the system's frequency, and the timescale of the FFCF will reflect, to some degree, the timescale of those dynamical processes. In our experiments we

do not measure the actual FFCF, but instead what is known as the inhomogeneity index,[56, 75] which is proportional to the normalized FFCF according to Equation 1.3,[75]

$$C(t_2) = \sin\left(\frac{\pi * II(t_2)}{2}\right) \tag{1.3}$$

Where $C(t_2)$ is the frequency-frequency autocorrelation function and $II(t_2)$ is the inhomogeneity index. The inhomogeneity index is a measurement which requires the collection of both rephasing and nonrephasing data sets, because the contribution of inhomogeneous broadening to a peak is included in rephasing data sets but is absent from nonrephasing data sets. This allows isolation of the dynamical timescale associated with the inhomogeneity of sample according to Equation 1.4,

$$II(t_2) = \frac{R(t_2) - NR(t_2)}{R(t_2) + NR(t_2)} \tag{1.4}$$

Where $R(t_2)$ is the amplitude of the peak in the rephasing spectrum, and $NR(t_2)$ is the amplitude of the same peak in the nonrephasing spectrum. The spectral diffusion of a vibrational mode has been linked to many microscopic and macroscopic experimental observables, including the viscosity of a series of linear alcohol solutions,[76] the response of the solvent's dielectric continuum to photoexcitation of a catalyst,[77] the nucleophilicity of the solvent,[78] and the dynamics of dynamics of constrained and bulk water.[63, 79-80]

1.5 Outline

The remainder of this thesis focuses upon investigation of the dynamics of systems affected by catalytically relevant phenomena which are ubiquitous in chemistry and vital to the reactivity of chemical and biochemical systems. With one exception, explained in its own chapter, these investigations will be performed using variants of the diiron hexacarbonyl systems described in 1.2.

Chapter 2 will describe an investigation of a chemically oxidized system, where a comparison is made between the dynamics observed in the oxidized system and same system in its unoxidized state. We find that the relaxation of the system's vibrational modes is significantly faster when the system is oxidized and that the rate of energy randomization and IVR between the carbonyl stretching modes of the system is correspondingly faster

when the system is oxidized than when it is in its neutral state. Interestingly enough, although the initial inhomogeneity of the system is noticeably increased by chemical oxidation, the timescale of spectral diffusion is relatively unaffected by the oxidation. We ascribe this to an idiosyncrasy of the solvent-solute interactions in our system, and note similarities observed between the dynamics our system in an oxidized state and those previously reported for similar molecules in electronically excited charge-transfer states.

Chapter 3 will describe our discovery of significant spectral diffusion in the vibrations of a diiron hexacarbonyl variant in a nonpolar alkane solvent. We discuss the apparent solvent-insensitivity of the spectral diffusion, and relate the spectral diffusion to a catalytically relevant mode of conformational mobility. Although this mode of conformational mobility occurs on a timescale inaccessible to our experimental methodology, we suggest that the spectral diffusion of our vibrational mode reflects the conformational mobility of our sample molecules within their ground-state conformation, and discuss other examples of conformationally mobile molecular systems where spectral diffusion is apparent in alkane solvents. These experiments represent, to the best of our knowledge, the first use of the spectral diffusion observable to report on the conformational flexibility of molecular system.

Chapter 4 will describe our investigation of the effect of steric bulk on the dynamics of a diiron hexacarbonyl variant in polar solvents by encapsulation of the diiron hexacarbonyl core within a dendritic assembly. We find significant dynamical changes induced in our system by the presence of the dendritic assembly, and discuss the similarity in trends we observe to those previously reported in studies of solvent-dependent dendritic conformation. This study represents, to the best of our knowledge, the first use 2D-IR to study the dynamics of a dendritic assembly.

Chapter 5 will describe our investigation into apparent signatures of vibrational coherence transfer in several diiron hexacarbonyl variants. Drawing upon previous investigations of vibrational coherence transfer in similar systems, we report the observation of trends in our data which suggest the presence of specific and unique pathways of coherence-coherence and coherence-population transfer in the vibrational dynamics of these systems. We discuss these observations in the light of the excitonic

nature of these systems, and the relevance of this information to studies of light-harvesting supramolecular assemblies in bacteria.

Chapter 6, the concluding chapter of this work, will summarize the work described here and discuss directions for future research into the central themes of this work.

References:

1. Gray, H. B.; Malmstrom, B. G.; Williams, R. J. P., Copper Coordination in Blue Proteins. *J Biol Inorg Chem* **2000,** *5*, 551-559.

2. Gray, H. B.; Winkler, J. R., Electron Transfer in Proteins. *Annu Rev Biochem* **1996,** *65*, 537-561.

3. Miesfeld, R. L.; McEvoy, M. M., *Biochemistry*. First edition. ed.; W.W. Norton & Company: New York, 2017.

4. Breslow, R., Biomimetic Chemistry and Artificial Enzymes - Catalysis by Design. *Accounts Chem Res* **1995,** *28*, 146-153.

5. Breslow, R.; Dong, S. D., Biomimetic Reactions Catalyzed by Cyclodextrins and their Derivatives. *Chem Rev* **1998,** *98*, 1997-2011.

6. Wiester, M. J.; Ulmann, P. A.; Mirkin, C. A., Enzyme Mimics Based Upon Supramolecular Coordination Chemistry. *Angew Chem Int Edit* **2011,** *50*, 114-137.

7. Schilter, D.; Camara, J. M.; Huynh, M. T.; Hammes-Schiffer, S.; Rauchfuss, T. B., Hydrogenase Enzymes and Their Synthetic Models: The Role of Metal Hydrides. *Chem Rev* **2016,** *116*, 8693-8749.

8. Zhao, M.; Wang, H. B.; Ji, L. N.; Mao, Z. W., Insights into Metalloenzyme Microenvironments: Biomimetic Metal Complexes with a Functional Second Coordination Sphere. *Chem Soc Rev* **2013,** *42*, 8360-8375.

9. Dydio, P.; Reek, J. N. H., Supramolecular control of selectivity in transition-metal catalysis through substrate preorganization. *Chem Sci* **2014,** *5*, 2135-2145.

10. Bistri, O.; Reinaud, O., Supramolecular Control of Transition Metal Complexes in Water by a Hydrophobic Cavity: a Bio-Inspired Strategy. *Org Biomol Chem* **2015,** *13*, 2849-2865.

11. Hecht, S.; Frechet, J. M. J., Dendritic Encapsulation of Function: Applying Nature's Site Isolation Principle from Biomimetics to Materials Science. *Angew Chem Int Edit* **2001,** *40*, 74-91.

12. Lubitz, W.; Ogata, H.; Rudiger, O.; Reijerse, E., Hydrogenases. *Chem Rev* **2014,** *114*, 4081-4148.

13. Lyon, E. J.; Georgakaki, I. P.; Reibenspies, J. H.; Darensbourg, M. Y., Coordination Sphere Flexibility of Active-Site Models for Fe-Only Hydrogenase: Studies in Intra- and Intermolecular Diatomic Ligand Exchange. *J Am Chem Soc* **2001,** *123*, 3268-3278.

14. Felton, G. A. N.; Vannucci, A. K.; Chen, J. Z.; Lockett, L. T.; Okumura, N.; Petro, B. J.; Zakai, U. I.; Evans, D. H.; Glass, R. S.; Lichtenberger, D. L., Hydrogen generation from weak acids: Electrochemical and computational studies of a diiron hydrogenase mimic. *J Am Chem Soc* **2007,** *129*, 12521-12530.

15. Veras, T. D.; Mozer, T. S.; dos Santos, D. D. R. M.; Cesar, A. D., Hydrogen: Trends, production and characterization of the main process worldwide. *Int J Hydrogen Energ* **2017,** *42*, 2018-2033.

16. Cox, P. M.; Betts, R. A.; Jones, C. D.; Spall, S. A.; Totterdell, I. J., Acceleration of global warming due to carbon-cycle feedbacks in a coupled climate model (vol 408, pg 184, 2000). *Nature* **2000,** *408*, 750-750.

17. Doney, S. C.; Fabry, V. J.; Feely, R. A.; Kleypas, J. A., Ocean Acidification: The Other CO2 Problem. *Annu Rev Mar Sci* **2009,** *1*, 169-192.

18. Ursua, A.; Gandia, L. M.; Sanchis, P., Hydrogen Production From Water Electrolysis: Current Status and Future Trends (vol 100, pg 410, 2012). *P Ieee* **2012,** *100*, 811-811.

19. Nikolaidis, P.; Poullikkas, A., A comparative overview of hydrogen production processes. *Renew Sust Energ Rev* **2017,** *67*, 597-611.

20. Wang, M.; Chen, L.; Sun, L. C., Recent progress in electrochemical hydrogen production with earth-abundant metal complexes as catalysts. *Energ Environ Sci* **2012,** *5*, 6763-6778.

21. Jian, J. X.; Liu, Q.; Li, Z. J.; Wang, F.; Li, X. B.; Li, C. B.; Liu, B.; Meng, Q. Y.; Chen, B.; Feng, K.; Tung, C. H.; Wu, L. Z., Chitosan Confinement Enhances Hydrogen Photogeneration from a Mimic of the Diiron Subsite of [FeFe]-hydrogenase. *Nat Commun* **2013,** *4,* 1-9.

22. Yu, T. J.; Zeng, Y.; Chen, J. P.; Li, Y. Y.; Yang, G. Q.; Li, Y., Exceptional Dendrimer-Based Mimics of Diiron Hydrogenase for the Photochemical Production of Hydrogen. *Angew Chem Int Edit* **2013,** *52*, 5631-5635.

23. Rauchfuss, T. B., Diiron Azadithiolates as Models for the [FeFe]-Hydrogenase Active Site and Paradigm for the Role of the Second Coordination Sphere. *Accounts Chem Res* **2015,** *48*, 2107-2116.

24. Chang, C. H.; Chen, M. H.; Du, W. S.; Gliniak, J.; Lin, J. H.; Wu, H. H.; Chan, H. F.; Yu, J. S. K.; Wu, T. K., A Ruthenium-Based Biomimetic Hydrogen Cluster for Efficient Photocatalytic Hydrogen Generation from Formic Acid. *Chem-Eur J* **2015,** *21*, 6617-6622.

25. Li, Y. L.; Rauchfuss, T. B., Synthesis of Diiron(I) Dithiolato Carbonyl Complexes. *Chem Rev* **2016,** *116*, 7043-7077.

26. Kaziannis, S.; Wright, J. A.; Candelaresi, M.; Kania, R.; Greetham, G. M.; Parker, A. W.; Pickett, C. J.; Hunt, N. T., The Role of CN and CO Ligands in the Vibrational

Relaxation Dynamics of Model Compounds of the [FeFe]-hydrogenase Enzyme. *Phys Chem Chem Phys* **2011,** *13*, 10295-10305.

27. Galinato, M. G. I.; Whaley, C. M.; Lehnert, N., Vibrational Analysis of the Model Complex (mu-edt[$Fe(CO)_3$]$_2$ and Comparison to Iron-Only Hydrogenase: The Activation Scale of Hydrogenase Model Systems. *Inorg Chem* **2010,** *49*, 3201-3215.

28. Gao, W. M.; Ekstrom, J.; Liu, J. H.; Chen, C. N.; Eriksson, L.; Weng, L. H.; Akermark, B.; Sun, L. H., Binuclear Iron-Sulfur Complexes with Bidentate Phosphine Ligands as Active Site Models of Fe-hydrogenase and their Catalytic Proton Reduction. *Inorg Chem* **2007,** *46*, 1981-1991.

29. Ghosh, S.; Hogarth, G.; Hollingsworth, N.; Holt, K. B.; Kabir, S. E.; Sanchez, B. E., Hydrogenase Biomimetics: $Fe_2(CO)_4$(mu-dppf)(mu-pdt) (dppf=1,1 '-bis(Diphenylphosphino)Ferrocene) both a Proton-Reduction and Hydrogen Oxidation Catalyst. *Chem Commun* **2014,** *50*, 945-947.

30. Liu, T. B.; Darensbourg, M. Y., A Mixed-Valent, Fe(II)Fe(I), Diiron Complex Reproduces the Unique Rotated State of the [FeFe]hydrogenase Active Site. *J Am Chem Soc* **2007,** *129*, 7008-7009.

31. Hsieh, C. H.; Erdem, O. F.; Harman, S. D.; Singleton, M. L.; Reijerse, E.; Lubitz, W.; Popescu, C. V.; Reibenspies, J. H.; Brothers, S. M.; Hall, M. B.; Darensbourg, M. Y., Structural and Spectroscopic Features of Mixed Valent (FeFeI)-Fe-II Complexes and Factors Related to the Rotated Configuration of Diiron Hydrogenase. *J Am Chem Soc* **2012,** *134*, 13089-13102.

32. Munery, S.; Capon, J. F.; De Gioia, L.; Elleouet, C.; Greco, C.; Petillon, F. Y.; Schollhammer, P.; Talarmin, J.; Zampella, G., New Fe-I-Fe-I Complex Featuring a Rotated Conformation Related to the [2Fe](H) Subsite of [Fe-Fe] Hydrogenase. *Chem-Eur J* **2013,** *19*, 15458-15461.

33. Bianchini, C.; Caulton, K. G.; Chardon, C.; Doublet, M. L.; Eisenstein, O.; Jackson, S. A.; Johnson, T. J.; Meli, A.; Peruzzini, M.; Streib, W. E.; Vacca, A.; Vizza, F., Mechanism of Acetylene Cyclotrimerization Catalyzed by the Fac-Irp3+ Fragment - Relationship between Fluxionality and Catalysis. *Organometallics* **1994,** *13*, 2010-2023.

34. Boese, R.; Huffman, M. A.; Vollhardt, K. P. C., Unique Reactivity of Heterodinuclear Pentacarbonyl(Fulvalene)Molybdenumruthenium with Alkynes - Fluxionality, Rearrangements, Structures, and 1st Reversible Conversion of a Side-on - to a Semi-Bridging Alkenylidene Ligand. *Angewandte Chemie-International Edition in English* **1991,** *30*, 1463-1465.

35. Ragone, F.; Poater, A.; Cavallo, L., Flexibility of N-Heterocyclic Carbene Ligands in Ruthenium Complexes Relevant to Olefin Metathesis and Their Impact in the First Coordination Sphere of the Metal. *J Am Chem Soc* **2010,** *132*, 4249-4258.

36. Wang, N.; Wang, M.; Liu, T. B.; Li, P.; Zhang, T. T.; Darensbourg, M. Y.; Sun, L. C., CO-migration in the ligand substitution process of the chelating diphosphite diiron complex (mu-pdt)[Fe(CO)$_3$][Fe(CO){(EtO)$_2$PN(Me)P(OEt}$_2$]. *Inorg Chem* **2008,** *47*, 6948-6955.

37. Li, B.; Liu, T. B.; Singleton, M. L.; Darensbourg, M. Y., Influence of Sulf-Oxygenation on CO/L Substitution and Fe(CO)$_3$ Rotation in Thiolate-Bridged Diiron Complexes. *Inorg Chem* **2009,** *48*, 8393-8403.

38. Bethel, R. D.; Crouthers, D. J.; Hsieh, C. H.; Denny, J. A.; Hall, M. B.; Darensbourg, M. Y., Regioselectivity in Ligand Substitution Reactions on Diiron Complexes Governed by Nucleophilic and Electrophilic Ligand Properties. *Inorg Chem* **2015,** *54*, 3523-3535.

39. Blank, J. H.; Moncho, S.; Lunsford, A. M.; Brothers, E. N.; Darensbourg, M. Y.; Bengali, A. A., Ligand Displacement Reaction Paths in a Diiron Hydrogenase Active Site Model Complex. *Chem-Eur J* **2016,** *22*, 12752-12760.

40. Felton, G. A. N.; Petro, B. J.; Glass, R. S.; Lichtenberger, D. L.; Evans, D. H., One- to Two-Electron Reduction of an [FeFe]-Hydrogenase Active Site Mimic: The Critical Role of Fluxionality of the [2Fe2S] Core. *J Am Chem Soc* **2009,** *131*, 11290-11291.

41. Greco, C.; Zampella, G.; Bertini, L.; Bruschi, M.; Fantucci, P.; De Gioia, L., Insights into the mechanism of electrocatalytic hydrogen evolution mediated by $Fe_2(S_2C_3H_6)(CO)_6$: The simplest functional model of the Fe-hydrogenase active site. *Inorg Chem* **2007,** *46*, 108-116.

42. Wang, M.; Chen, L.; Li, X. Q.; Sun, L. C., Approaches to efficient molecular catalyst systems for photochemical H_2 production using [FeFe]-hydrogenase active site mimics. *Dalton T* **2011,** *40*, 12793-12800.

43. Camara, J. M.; Rauchfuss, T. B., Combining acid-base, redox and substrate binding functionalities to give a complete model for the [FeFe]-hydrogenase. *Nat Chem* **2012,** *4*, 26-30.

44. Cheng, M. L.; Wang, M.; Zhang, S.; Liu, F. Y.; Yang, Y.; Wan, B. S.; Sun, L. C., Photocatalytic H_2 Production using a Hybrid Assembly of an [FeFe]-hydrogenase Model and CdSe Quantum Dot Linked through a Thiolato-Functionalized Cyclodextrin. *Faraday Discuss* **2017,** *198*, 197-209.

45. Wang, F.; Liang, W. J.; Jian, J. X.; Li, C. B.; Chen, B.; Tung, C. H.; Wu, L. Z., Exceptional Poly(acrylic acid)-Based Artificial [FeFe]-Hydrogenases for Photocatalytic H_2 Production in Water. *Angew Chem Int Edit* **2013,** *52*, 8134-8138.

46. Singleton, M. L.; Reibenspies, J. H.; Darensbourg, M. Y., A Cyclodextrin Host/Guest Approach to a Hydrogenase Active Site Biomimetic Cavity. *J Am Chem Soc* **2010,** *132*, 8870-8871.

47. Ball, D. W., *Physical chemistry*. Thomson-Brooks/Cole: Pacific Grove, CA, 2003.

48. Hartwig, J. F., *Organotransition Metal Chemistry : from Bonding to Catalysis*. University Science Books: Sausalito, Calif., 2010.

49. Housecroft, C. E.; Sharpe, A. G., *Inorganic chemistry*. 2nd ed.; Pearson Prentice Hall: Upper Saddle River, N.J., 2005.

50. Huheey, J. E.; Keiter, E. A.; Keiter, R. L., *Inorganic chemistry : principles of structure and reactivity*. 4th ed.; HarperCollins College Publishers: New York, NY, 1993.

51. Willner, H.; Aubke, F., Homoleptic metal carbonyl cations of the electron-rich metals: Their generation in superacid media together with their spectroscopic and structural characterization. *Angew Chem Int Edit* **1997,** *36*, 2403-2425.

52. Goldman, A. S.; KroghJespersen, K., Why do cationic carbon monoxide complexes have high C-O stretching force constants and short C-O bonds? Electrostatic effects, not sigma-bonding. *J Am Chem Soc* **1996,** *118*, 12159-12166.

53. Lupinetti, A. J.; Fau, S.; Frenking, G.; Strauss, S. H., Theoretical analysis of the bonding between CO and positively charged atoms. *J Phys Chem A* **1997,** *101*, 9551-9559.

54. Hocking, R. K.; Hambley, T. W., Database analysis of transition metal carbonyl bond lengths: Insight into the periodicity of pi back-bonding, sigma donation, and the factors affecting the electronic structure of the TM-C O moiety. *Organometallics* **2007,** *26*, 2815-2823.

55. Nee, M. J.; McCanne, R.; Kubarych, K. J.; Joffre, M., Two-dimensional infrared spectroscopy detected by chirped pulse upconversion. *Opt Lett* **2007,** *32*, 713-715.

56. Khalil, M.; Demirdoven, N.; Tokmakoff, A., Coherent 2D IR spectroscopy: Molecular structure and dynamics in solution. *J Phys Chem A* **2003,** *107*, 5258-5279.

57. Elsaesser, T.; Kaiser, W., Vibrational and Vibronic Relaxation of Large Polyatomic-Molecules in Liquids. *Annu Rev Phys Chem* **1991,** *42*, 83-107.

58. Uzer, T.; Miller, W. H., Theories of Intramolecular Vibrational-Energy Transfer. *Phys Rep* **1991,** *199*, 73-146.

59. Owrutsky, J. C.; Raftery, D.; Hochstrasser, R. M., Vibrational-Relaxation Dynamics in Solutions. *Annu Rev Phys Chem* **1994,** *45*, 519-555.

60. Stratt, R. M.; Maroncelli, M., Nonreactive Dynamics in Solution: The Emerging Molecular View of Solvation Dynamics and Vibrational Relaxation. *J Phys Chem* **1996,** *100*, 12981-12996.

61. Tokmakoff, A.; Sauter, B.; Fayer, M. D., Temperature-Dependent Vibrational-Relaxation in Polyatomic Liquids - Picosecond Infrared Pump-Probe Experiments. *J Chem Phys* **1994,** *100*, 9035-9043.

62. Yan, S. X.; Seidel, M. T.; Zhang, Z. Y.; Leong, W. K.; Tan, H. S., Ultrafast vibrational relaxation dynamics of carbonyl stretching modes in Os-3(CO)(12). *J Chem Phys* **2011,** *135*.

63. King, J. T.; Ross, M. R.; Kubarych, K. J., Water-Assisted Vibrational Relaxation of a Metal Carbonyl Complex Studied with Ultrafast 2D-IR. *J Phys Chem B* **2012,** *116*, 3754-3759.

64. Heilweil, E. J.; Cavanagh, R. R.; Stephenson, J. C., Population Relaxation of Co(V=1) Vibrations in Solution Phase Metal-Carbonyl-Complexes. *Chem Phys Lett* **1987,** *134*, 181-188.

65. Anna, J. M.; King, J. T.; Kubarych, K. J., Multiple Structures and Dynamics of $[CpRu(CO)_2]_2$ and $[CpFe(CO)_2]_2$ in Solution Revealed with Two-Dimensional Infrared Spectroscopy. *Inorg Chem* **2011,** *50*, 9273-9283.

66. Delor, M.; Sazanovich, I. V.; Towrie, M.; Spall, S. J.; Keane, T.; Blake, A. J.; Wilson, C.; Meijer, A. J. H. M.; Weinstein, J. A., Dynamics of Ground and Excited State Vibrational Relaxation and Energy Transfer in Transition Metal Carbonyls. *J Phys Chem B* **2014,** *118*, 11781-11791.

67. Fayer, M. D., Dynamics of Liquids, Molecules, and Proteins Measured with Ultrafast 2D IR Vibrational Echo Chemical Exchange Spectroscopy. *Annu Rev Phys Chem* **2009,** *60*, 21-38.

68. Anna, J. M.; Ross, M. R.; Kubarych, K. J., Dissecting Enthalpic and Entropic Barriers to Ultrafast Equilibrium Isomerization of a Flexible Molecule Using 2DIR Chemical Exchange Spectroscopy. *J Phys Chem A* **2009,** *113*, 6544-6547.

69. King, J. T.; Anna, J. M.; Kubarych, K. J., Solvent-Hindered Intramolecular Vibrational Redistribution. *Phys Chem Chem Phys* **2011,** *13*, 5579-5583.

70. Yang, F.; Zhao, J.; Wang, J. P., Two-Dimensional Infrared Study of C^{13}-Natural Abundant Vibrational Transition Reveals Intramolecular Vibrational Redistribution Rather than Fluxional Exchange in $Mn(CO)_5Br$. *J Phys Chem B* **2016,** *120*, 1304-1311.

71. Cahoon, J. F.; Sawyer, K. R.; Schlegel, J. P.; Harris, C. B., Determining transition-state geometries in liquids using 2D-IR. *Science* **2008,** *319*, 1820-1823.

72. Hamm, P.; Zanni, M. T., *Concepts and Methods of 2D Infrared Spectroscopy*. Cambridge University Pres: Cambridge ; New York, 2011.

73. Mukamel, S., *Principles of Nonlinear Optical Spectroscopy*. Oxford University Press: New York, 1995.

74. Kwak, K.; Park, S.; Finkelstein, I. J.; Fayer, M. D., Frequency-frequency correlation functions and apodization in two-dimensional infrared vibrational echo spectroscopy: A new approach. *J Chem Phys* **2007,** *127,* 124503.

75. Roberts, S. T.; Loparo, J. J.; Tokmakoff, A., Characterization of Spectral Diffusion from Two-Dimensional Line Shapes. *J Chem Phys* **2006,** *125,* 084502.

76. King, J. T.; Baiz, C. R.; Kubarych, K. J., Solvent-Dependent Spectral Diffusion in a Hydrogen Bonded "Vibrational Aggregate". *J Phys Chem A* **2010,** *114*, 10590-10604.

77. Kiefer, L. M.; King, J. T.; Kubarych, K. J., Equilibrium Excited State Dynamics of a Photoactivated Catalyst Measured with Ultrafast Transient 2DIR. *J Phys Chem A* **2014,** *118*, 9853-9860.

78. Kiefer, L. M.; Kubarych, K. J., Solvent-Dependent Dynamics of a Series of Rhenium Photoactivated Catalysts Measured with Ultrafast 2DIR. *J Phys Chem A* **2015,** *119*, 959-965.

79. King, J. T.; Arthur, E. J.; Brooks, C. L.; Kubarych, K. J., Site-Specific Hydration Dynamics of Globular Proteins and the Role of Constrained Water in Solvent Exchange with Amphiphilic Cosolvents. *J Phys Chem B* **2012,** *116*, 5604-5611.

80. King, J. T.; Arthur, E. J.; Brooks, C. L.; Kubarych, K. J., Crowding Induced Collective Hydration of Biological Macromolecules over Extended Distances. *J Am Chem Soc* **2014,** *136*, 188-194.

Chapter 2

Oxidation-State Dependent Vibrational Dynamics Probed with 2D-IR

The work presented in this chapter has been published in the following paper:

Eckert, P. A.; Kubarych, K. J., Oxidation-State-Dependent Vibrational Dynamics Probed with 2D-IR. *J Phys Chem A* **2017,** 121, 2896-2902.

2.1 Introduction

Although the significant role of the solvent in determining the kinetics and thermodynamics of chemical reactions is well known, reaction optimization remains a largely empirical process due to the inability to predict solvent effects.[1] Ultrafast spectroscopy has traditionally addressed this problem by studying the solvation dynamics of model dye systems as well as photochemistry and photophysics in a vast array of solvents.[2-5] Polar solvation is largely dominated by changes in charge density on the solute atoms, which induces a solvent response that likely evolves as a reaction proceeds from reactants to the transition state and ultimately to the products.[3, 6] Despite extensive progress in understanding microscopic solvation dynamics and structure, there is currently no practical solution to the challenges faced by chemists in, for example, optimizing chemical reaction conditions.

Though by no means a resolution to the long-standing puzzle of understanding solvent dependent chemistry, here we adopt a new strategy that isolates the dynamical consequences of making changes in charge distributions without causing substantial geometrical distortions. Using two distinct redox states of the same complex, we are able to study two different chemical systems whose ground-state electronic structure can be chemically altered without changing the molecular geometry. Comparing our results to

analogous transient two-dimensional spectroscopy on a different organometallic complex, we observe redox state dependent vibrational relaxation and intramolecular vibrational redistribution. We not find a significant redox state dependence of the solvation dynamics as reported by the spectral diffusion; we speculate that this insensitivity is likely due to an idiosyncrasy of the dichloromethane solvent required for the redox chemistry. Previous results from Khalil et al.[7] and from Massari et al.[8-12] have found various dependencies on solvent, as well as on ligand substitution. Taken together we expect a more comprehensive view to emerge regarding the nature of vibrational and solvation dynamics in transition metal complexes.

We report a study of the inter- and intramolecular affects induced by oxidation to a radical cation using the molecule [1,1'-bis(diphenylphosphino)ferrocene]tetracarbonyl chromium (DPPFCr, **Fig. 2.1A-C**). The DPPF ligand is commonly encountered in organometallic catalysis,[13-16] and the carbonyl ligands offer a localized probe with a strong and background-free transition frequency. DPPFCr is not itself a commonly used catalyst, but it offers a good model of a class of common catalysts, and other organometallic DPPF complexes have been investigated for use in energy storage.[17-18] We find significant changes in intramolecular dynamics induced by oxidation to a cation radical state, exhibiting similarities and differences when compared to ultrafast studies of electronic state dependent spectral dynamics in rhenium bipyridyl CO_2 reduction photocatalysts.

The role of solvation in modulating or directing chemical reactivity is widely appreciated, though often understood largely at the level of empirical correlations. It is still a challenge to link fine-grained molecular details of solute-solvent interactions while maintaining the utility of essentially continuum, macroscopic properties. Some key characteristics, such as polarity, are not even well defined without resorting to some sort of internal standard, which is itself a molecule with specific structure and specific interactions.[19-20] Due to the successful development of spectroscopic probes of solvation based on measuring dynamic Stokes shifts, it has become natural to consider polar solvation from the perspective of a time-domain relaxation following optical excitation that shifts charge density within the solute, eliciting a response from the solvent. The optical response in that case remains the transition energy gap between the nonstationary

excited electronic state and the ground electronic state, which finds itself in an ever more nonequilibrium environment as the solvation proceeds, governed to some extent by the excited state solute's charges. The reliance upon electronic transitions necessarily links the two surfaces' dynamics, making it difficult to track dynamics on either one independently. To the extent that linear response seems to hold in many cases, it would appear that the intrinsic equilibrium dynamics of the two electronic states are very similar.

The Kubarych group has recently examined the equilibrium solvation dynamics of a rhenium(I) transition metal complex that photocatalyzes the reduction of CO_2. Using transient two-dimensional infrared (2D-IR) spectroscopy, they found the vibrational spectral diffusion—a measure largely of solvation dynamics—to be electronic state dependent.[21] The spectral diffusion of the CO stretch vibrations is roughly three-fold slower on the triplet metal-to-ligand charge-transfer (^{3}MLCT) state than it is in the singlet ground state. For these measurements they used the solvent tetrahydrofuran (THF), which is commonly used in CO_2 photocatalysis. They attributed the slowdown in spectral diffusion to the substantial reduction in the molecular dipole moment, from 14.1 D in the ground state to 5.8 D in the ^{3}MLCT state. Using simple arguments based on dielectric friction using the Nee-Zwanzig description, they found a qualitative agreement with previous analyses of fluorescence Stokes shift results by Maroncelli et al.[2] The decreased dipole moment of the excited state leads to a reduced coupling to the solvent dielectric continuum, resulting in reduced drag. Reduced friction slows down sampling of available microscopic configurations that comprise the inhomogeneously broadened band. To test the molecular dipole dependence, they altered the substituents on the aromatic bipyridine ligand, but found no change regardless of the electron withdrawing or donating character of the substituted functional groups.[22] They concluded that the relevant changes in electrostatics are those local to the CO ligands, rather than due to charge redistribution on the whole complex.

In parallel to the Kubarych group's work on photoinduced intramolecular charge transfer, others have been implementing electrochemical cells compatible with ultrafast 2D-IR spectroscopy.[23-24] This is a long-standing goal, and has been solved by two clever uses of surfaces, either leveraging the attenuated total reflectance mode common in FTIR

spectroscopy, or as a mirror. The conductive surfaces can serve as electrodes to modulate the local electric field, enabling oxidation and reduction of surface-bound solutes. In work by Hamm et al., CO bound on to a metal surface at different electrochemical potentials was found to exhibit a band-center shift, but not a change in line width or in spectral diffusion dynamics.[24] The lack of a field dependence implies both the solvation dynamics and the mapping of local electrostatics to the oscillator's frequency is not significantly influenced by the electrochemical potential.

Detailed solution-phase investigation of the vibrational changes accompanying a change in redox state are complicated by the response of most molecular systems to redox events. Changes in the molecular electronic structure are frequently accompanied by a dissociation of the molecule.[25-26] Compounds which do not dissociate after a redox event often undergo a distortion of their molecular geometry in order to support the new molecular charge, and remain highly reactive to other molecular species in their charged state.[25-26] One example of this such a response to redox events may be found in the class of diiron hexacarbonyl compounds discussed in the introduction. The response of diiron carbonyl compounds to redox events is highly dependent upon the ligands in the first coordination sphere of the diiron core, but most diiron carbonyl compounds undergo molecular organization upon both oxidation and reduction.[27-29] Since the vibrational modes of a molecule are fundamentally dependent upon its geometric and electronic structure, a comparison of the molecular vibrations before and after an oxidation or reduction is often impossible, if only because the vibrations pre- and post-oxidation differ so fundamentally that the concept of a comparison becomes somewhat poorly defined. However, in the case of comparable vibrational structure before and after the oxidation event, the question of the effect of oxidation upon those vibrations is not only meaningful, but also of significant interest due to the ubiquity of oxidation and reduction events in chemical reactivity

In the present work, we sought to identify a system where we could modulate the formal charge of a complex by chemical oxidation or reduction, and compare the spectral dynamics of the two oxidation states. Ideally, we would choose a molecule where there are only negligible structural changes upon either oxidation or reduction. Indeed, a previous

study of metallocarbonyl radicals has been performed, but the radicals in this study were created by cleaving a parent piano-stool metal carbonyl dimer complex into two monomers, making direct comparison of the vibrational modes between the neutral dimer and radical monomers difficult.[30] To this end, we investigate DPPFCr, which can be oxidized from DPPFCr(0) to DPPFCr(I) using tris-(4-bromphenyl)aminiumyl hexachloroantimonate (TBAH). Here we find significant changes in the frequencies of the carbonyl bands as well as their line widths, but we do not find a substantial oxidation state dependence to the spectral diffusion dynamics. Interestingly, the intramolecular vibrational redistribution and vibrational energy relaxation do exhibit significant oxidation state dependences, which we are able to rationalize qualitatively by considering the computed anharmonic mode couplings. There are several noteworthy similarities between the two oxidation states of DPPFCr and the two electronic states of $ReCl(CO)_3bpy$, such as the change in dipole moment and the mode-specific frequency shifts due to ligand-specific changes in partial charges among the carbonyl units. Nevertheless, we do not recapitulate the change in spectral diffusion dynamics, though the solvent we must use, dichloromethane, is particularly weakly coordinating (i.e. low donicity), and we have previously found donicity to be a key factor determining the time scale for spectral diffusion.

2.2 Experimental Procedures

All chemical manipulations in this study were performed in a glove box under an atmosphere of continuously purged N_2, and all compounds used in this study were purchased from Sigma Aldrich and used as received, except for the dichloromethane solvent, which was kept dry over molecular sieves.

The DPPFCr was chemically oxidized according to the procedure outlined by Oh et al.[31] In the glove box a CH_2Cl_2 solution of tris(4-bromophenyl)aminiumyl hexachloroantimonate (TBAH) was added dropwise to an equimolar CH_2Cl_2 solution of DPPFCr. The mixture was stirred for several minutes and slowly assumed the vibrant purple color reported for the oxidized DPPFCr species. To ensure an oxygen-free solution,

the sample cell was prepared in the glove box, and taken directly to the 2D-IR experimental set-up.

The experimental 2D-IR set-up described in Chapter 1.3 was employed in this experiment, as was the Jasco 4100 FTIR.

Electronic structure calculations were performed using the Gaussian 09 software package.[32] The functional B3LYP and the an all-electron basis set 6-31G(d,p) were used to calculate the geometry and vibrations of DPPFCr in its neutral closed-shell state and in its open-shell cation-radical state. All calculations were performed in a vacuum without

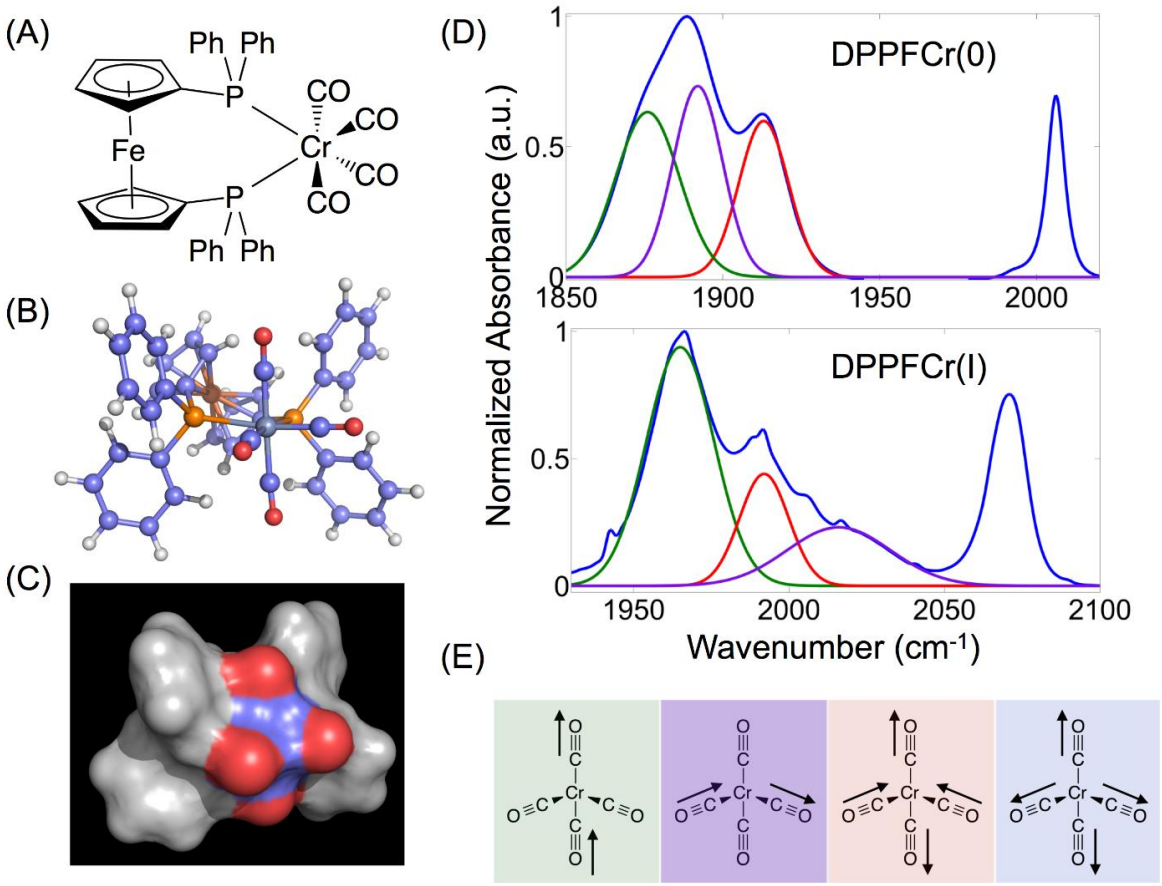

Figure 2.1. (A-C) Schematic representation, DFT-optimized geometry, and space-filling representation of DPPFCr. Note that in the space-filling representation the carbonyl groups are somewhat enclosed by the four phenyl groups. (D) FTIR spectra of the four carbonyl stretching modes of DPPFCr in neutral (top) and oxidized (bottom) electronic states. Note that the x-axes are shifted by roughly 100 cm^{-1} due to the change in electronic structure, and that gaussian fits have been added to the spectra to clarify the overlapping vibrational bands. (E) Mode assignments based on quantum chemical calculations. This figure was adapted from the journal article in which these results were published.

implicit solvent. Natural Population Analysis was used to determine the change in atomic population caused by molecular oxidation.

2.3 Results

The optimized geometry of DPPFCr, geometric displacements associated with each vibrational mode, and the FTIR spectra of DPPFCr's carbonyl vibrations in the neutral and cation radical states are shown in Figure 2.1. For the remainder of this work DPPFCr in its neutral for will be denoted as "DPPFCr(0)" and in its oxidized form as "DPPFCr(I)."

There are several notable spectral changes associated with the oxidation event, particularly a pronounced and non-uniform blue shifting of the carbonyl vibrational modes

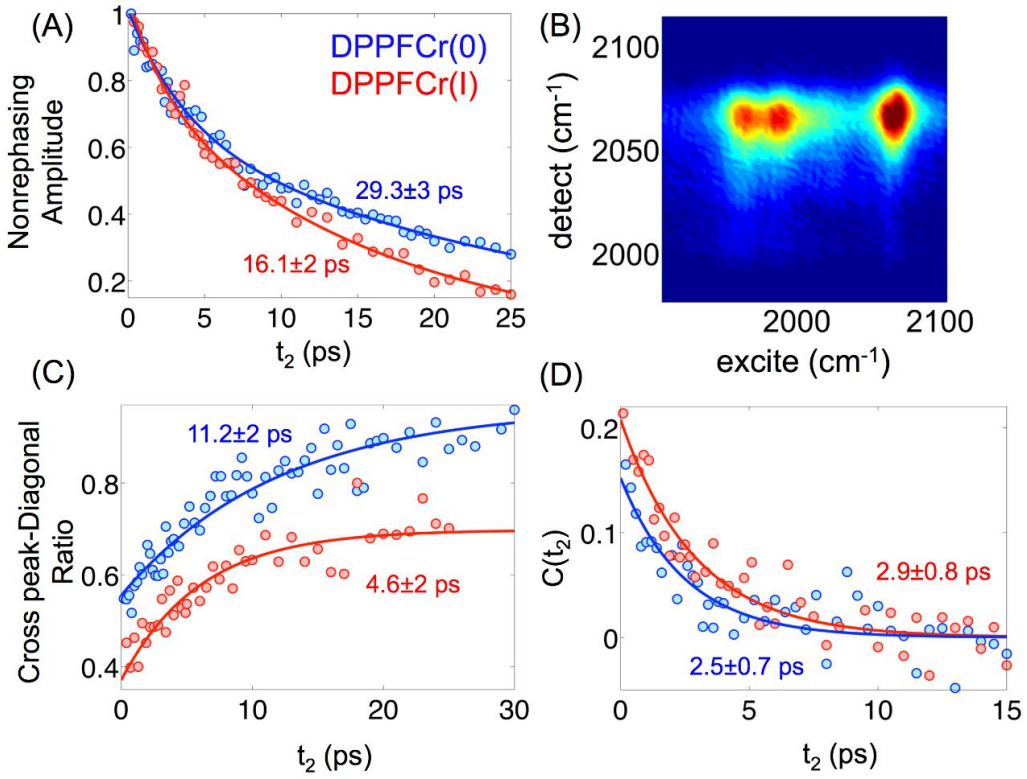

Figure 2.2. A) Normalized peak amplitude of mode 1 in CH_2Cl_2 for DPPFCr(0) and DPPFCr(I). Vibrational lifetimes given by the fits are listed in the figure. B) 2D-IR nonrephasing spectrum of mode 1, DPPFCr(I), in CH_2Cl_2, 3.7 ps after excitation. C) Ratio of the amplitudes of the (ω_{excite}=mode 2, ω_{detect}=mode 1) cross peak and the diagonal mode 1 peak in CH_2Cl_2. The timescale for intramolecular vibrational randomization for DPPFCr(0) and DPPFCr(I) are given as 11.2±2 ps and 4.6±2 ps, respectively. D) Spectral diffusion data for mode 1 of DPPFCr(0) and DPPFCr(I) in CH_2Cl_2, with the respective time-constants of 2.5±0.7ps and 2.9 ±0.8 ps. This figure was adapted from the journal article in which these results were published.

upon oxidation. The highest frequency mode, predicted to be a symmetric stretching of all four carbonyl ligands, blue shifts by around 60 cm^{-1}, while the second to lowest frequency mode in the neutral form blue shifts by roughly 120 cm^{-1} upon oxidation, and in fact switches place in the mode frequency ordering with the vibrational mode which second highest in frequency in the neutral form.

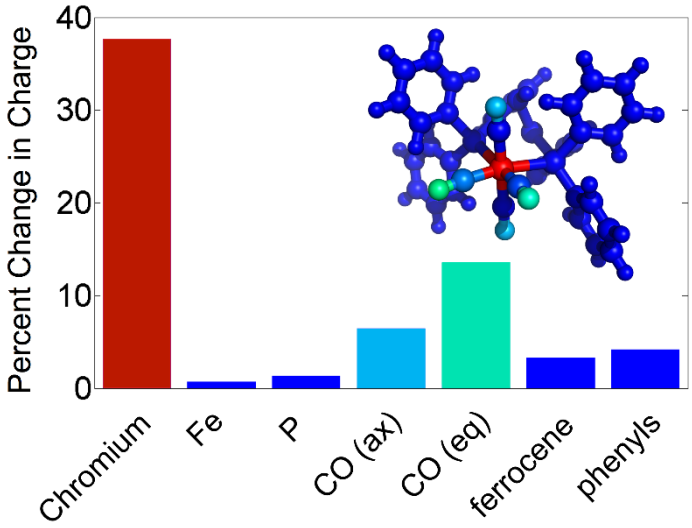

Figure 2.3. Changes in the partial charges on various atoms and groups in DPPFCr(I) as a percentage of the DPPFCr(0) charges. All charges become more positive since there is a net loss of one electron on the complex. The Cr charge changes the most, followed by the equatorial and the axial carbonyls, respectively. The charge decrease of the equatorial carbonyls is probably associated with the larger frequency shifts of the mode involving only these carbonyl groups. This figure was adapted from the journal article in which these results were published.

The vibrational relaxation and spectral diffusion of the highest frequency mode are shown in Figure 2.2, along with a 2D spectrum of the highest frequency mode and its cross peaks in the oxidized state and the cross peak ratios of the highest frequency mode and the second-highest frequency mode in the neutral state.

The vibrational relaxation of the highest frequency mode is visibly faster in the oxidized state than in the neutral, and a similar change is apparent in the timescale of IVR between the modes which are highest and second highest frequency in the neutral state. In contrast to this marked change, the spectral diffusion of mode shows a timescale that remains relatively unchanged in the oxidized state, although the y-intercept of the function, which represents the initial inhomogeneity of the sample, is noticeably higher in the oxidized state than in DPPFCr(I) than in DPPFCr(0), which is in good agreement with the broadening of the highest frequency mode upon oxidation evident in the FTIR spectra.

Figure 2.3 shows the change in atomic population of each of DPPFCr's functional groups caused by molecular oxidation, as computed with electronic structure methods.

As indicated by electronic structure calculations, the molecular oxidation is localized on the chromium atom and the carbonyl ligands, of which the equatorial pair is most significantly affected. The DPPF ligand is observed to be essentially unaffected by the oxidation event, which is in good agreement with our spectroscopic data.

2.4 Discussion

The changes observed in the FTIR spectrum of DPPFCr upon chemical oxidation are an excellent example of the sensitivity of carbonyl vibrational frequencies to the electron density of the metal to which they are bonded. As discussed in 1.2, metal carbonyl ligands participate in two bonding modes, but the most spectrally significant of those two is π-backbonding, in which electron density from the metal's d-orbitals is donated into the π*-antibonding carbon monoxide molecular orbital.[33] When the carbon monoxide group bonds to an electron-rich metal center a significant amount of electron density is donated to the π*-antibonding orbital, and this weakens the carbon-oxygen bond and causes the vibration frequency of the carbon monoxide to red shift.[34] The molecular oxidation dramatically reduces the electron density of the chromium atom to which the carbonyl groups are bonded, and this in turn reduces the electron density available for donation into the carbonyl π*-antibonding orbitals, which is reflected in a stronger carbon-oxygen bond and a corresponding blue shift in the carbonyl vibrational frequencies. This experimental trend is in excellent agreement with the results of our electronic structure calculations, for if the molecular oxidation were in fact delocalized over a larger fraction of the molecule the corresponding loss of electron density on the chromium would be lower, and the effect on the carbonyl vibrational frequencies would be less pronounced.

Interestingly, the vibrational band which our calculations attribute to an out-of-phase stretching of the equatorial carbonyl groups is very affected by the oxidation, blue shifting twice as much as the highest frequency mode, broadening dramatically and becoming much weaker. Our calculations also predict that the pair of equatorial carbonyls is much more affected by the oxidation than the axial pair, and the disproportionate

response of this vibration to the redox event provides support for the experimental relevance of our electronic structure calculations. Changes in the relative ordering of vibrational modes in molecular electronic states have been reported for other metal carbonyl complexes.[21, 35]

The data on vibrational relaxation and IVR both display similar trends, and have a unifying interpretation. The relaxation of a vibrational mode arises from a cascading process of energy transfer to vibrational modes of lower frequency.[36-37] Typically the rate of energy transfer depends upon the several factors, including the mode coupling and the energy difference between the two modes.[38-39] Our electronic structure calculations indicate that although molecular oxidation does typically affect the frequency of the vibrational modes which are un-altered by the redox event, the difference frequency between the carbonyl stretching modes and lower frequency modes closest to them in frequency is not significantly altered. The faster inter-carbonyl IVR is compatible with the hypothesis that the coupling of the carbonyl vibrational modes is significantly increased by the redox event, and if the coupling of the carbonyl modes with modes of significantly lower frequency were also increased the vibrational relaxation of the carbonyl modes would be expected to accelerate, as is experimentally observed.

A similar but much more dramatic increase in vibrational relaxation has been reported for molecules in ^{3}MLCT electronic excited states. In [Re(CO)$_3$(bipyridine)]Cl the vibrational relaxation of the carbonyl stretching modes accelerates ~ 10-fold in the ^{3}MLCT state,[21, 40] and a comparable acceleration has been reported for [Re(phenanthroline)$_2$(NCS)$_2$].[41] In both of these compounds electronic excitation is followed by the formation of a transient positive charge on the metal atom to which the carbonyls and SCN ligands are bound, causing a state similar to that induced by chemical oxidation of the DPPFCr. We note that in all three cases, despite the physical differences between a charge transfer in an electronic excited state and a molecular oxidation in the ground state, the reduction of electron density on the central metal atom is accompanied by an acceleration if vibrational relaxation timescales.

The spectral diffusion of a vibrational mode is caused by fluctuations in a mode's potential due to a number of factors, including electrostatic fluctuations of the local

environment.[42-44] In polar and interacting solvents, solvent-solute interactions exert a noticeable influence on the spectral diffusion of solvent-accessible carbonyl ligands.[22, 45] Since the polarity of a solute is critical in solvation, any change in its dipole moment could reasonably be expected to modify the solvent-solute interactions of the system, and thus influence the spectral diffusion of the solute's vibrational modes. Oxidation does induce a 3-fold change in DPPFCr's dipole moment, reducing it from 7.5 D to 2.5 D, but the timescale of spectral diffusion for the carbonyl ligands is largely unaffected. Recent work has shown that the carbonyl ligands in $[Re(CO)_3(bpy)]Cl$ derivatives are insensitive to the dipole moment of the entire complex, and suggested that the highly localized CO stretching modes primarily report the dynamics of the immediately adjacent solvation environment.[22] In DPPFCr, where the effect of oxidation is localized on the carbonyl ligands and the metal to which they are bonded, any change in the solvation environment is expected to be greatest in the solvent adjacent to the carbonyl groups. However, the experimentally measured timescales of spectral diffusion are very similar for both oxidation state.

We hypothesize that two contributions, steric hindrance and solvent nucleophilicity, contribute to the redox state insensitivity of the carbonyl modes of DPPFCr. In a set of experiments on derivatives of $[Mo(CO)_4(phenanthroline)]$, the presence of side groups on the 2 and 9 phenanthroline carbons significantly reduced the rate of reactions with acetonitrile, indicating that even slight steric bulk near the metal center in the equatorial plane of the complex significantly impedes crucial intermolecular interactions.[46] In DPPFCr, the equatorial plane on both sides of the metal center is occupied by bulky, flexible phenyl rings. These side groups significantly restrict solvent accessibility to the metal center.

The second contributing factor is the donicity of the solvent. The nucleophilicity of a solvent is related to a parameter known as the donor number, which is defined as the enthalpy of complex formation between $SbCl_5$ and the molecule of interest in a dilute solution of dichloroethane.[47] A high donor number signifies the presence of strong complexation, and a low donor number signifies weak complexation.[47] The donor number of a solvent has been shown to directly correlate with the timescale of spectral diffusion

for carbonyl modes in derivatives of $[Re(CO)_3(bpy)]Cl$. The solvent used in this study, dichloromethane, has a donor number of 1 kcal/mol, much lower than the donor numbers of other common organic solvents like acetonitrile and THF, which are 14 and 20 kcal/mol, respectively.[48] In light of the low basicity of dichloromethane, the oxidation-insensitivity of the spectral diffusion timescales in both oxidation states may be a reflection of the idiosyncratically non-interacting nature of the solvent. The high reactivity of DPPFCr(I) to other polar solvents makes this hypothesis difficult test.

The overall picture that emerges from our data is that of a strongly metal-centered oxidation which does not significantly alter the total molecular geometry, but does induce changes in intramolecular vibrational coupling. Metal carbonyls are typically sensitive to the local solvation environment, so the insensitivity of the spectral diffusion to the oxidation suggests either that the carbonyls are very shielded by the phenyl side groups, or that the local solvation environment is insignificantly affected by the oxidation. Dichloromethane was chosen as a solvent specifically because it does not react with the cation radical generated by the molecular oxidation, so some element of solvent insensitivity to the change caused by oxidation is expected.

Recent studies of electronically excited molecular catalysts provide an interesting comparison to our ground electronic state results. In the studies of molecular catalysts, the molecule is photoexcited to the first triplet excited state and its vibrational dynamics are probed in the excited state and compared to those in the ground state. While in the excited state, a triplet metal-to-ligand charge transfer causes the formation of a transient positive charge on the metal atom and a corresponding negative charge on the organic ligand. Several studies on derivatives of $[Re(CO)_3(bpy)]Cl$ and of $[Ru(phen)_2(NCS)_2]$ report a significantly faster vibrational relaxation of the C≡O and NCS ligands in ^{3}MLCT state than in the ground electronic state.[21, 40-41] The accelerated vibrational relaxation is solvent insensitive in the case of $[Re(CO)_3(bpy)]Cl$ derivatives, and the effect is attributed to enhanced intramolecular vibrational couplings;[40, 49] similar solvent studies have not been reported for $Ru(phen)_2(NCS)_2$. Measurements of spectral diffusion for $[Re(CO)_3(bpy)]Cl$ have been performed largely in nucleophilic solvents such as THF, acetonitrile and DMSO.[21-22, 50]

A comparison of spectral diffusion trends between $[Re(CO)_3(bpy)]Cl$ in the ^{3}MLCT state and DPPFCr(I) is complicated by significant difference in solvent nucleophilicities and by the steric hindrance to solvent accessibility in DPPFCr – no similar side groups are present in $[Re(CO)_3(bpy)]Cl$. Both DPPFCr and the $[Re(CO)_3(bpy)]Cl$ derivatives are minimally distorted by, and both show accelerated vibrational relaxation upon oxidation and electronic excitation, respectively. The two molecules are chemically distinct, but a commonality for both is the reduction of electron density on the transition metal to which the carbonyls are bonded. It has been previously suggested that change in electron density of the transition metal atom induces electrostatic interactions between the oxidized metal center and the carbonyl group which enhance coupling of the low-frequency metal-carbon and high-frequency C≡O stretches and accelerate the vibrational relaxation of the carbonyl stretching modes.[41]

Although oxidation in the ground electronic state and formation of a ^{3}MLCT state are very different phenomena, they result in similar changes to the electronic structure. Observation of similar trends in IVR and vibrational lifetimes for the carbonyl ligands in both states suggests that these aspects of the vibrational dynamics of carbonyl ligands are driven largely by intramolecular couplings, which is consistent with standard descriptions.[51] The absence of oxidation state dependent solvation dynamics, however, is unexpected, especially in light of the large molecular dipole moment change. Nevertheless we have previously found a lack of dependence on overall molecular dipole moment change in the rhenium bipyridyl complexes, though in that study the partial charges on the CO ligands were essentially unchanged by chemical substitution. Here, the CO ligands do exhibit changes in partial charge, so we might have expected some influence on spectral diffusion dynamics. Thus we speculate that the very low donicity of the DCM solvent idiosyncratically determines the solvation, and were we able to prepare both stable oxidation states in a higher donicity solvent, we would expect a dynamical consequence of the oxidation state. This hypothesis will be investigated in future work, and perhaps will be accessible using novel spectroelectrochemical approaches.

2.5 Conclusion

We report an investigation of the effects of chemical oxidation of a molecular catalyst using 2D-IR spectroscopy. With electronic structure calculations and by comparing vibrational modes which are structurally unaltered by the oxidation, we find enhanced intramolecular coupling in the cation radical, whereas we see no significant change in spectral diffusion dynamics. We hypothesize that the insensitivity of the FFCF to molecular oxidation is due to a combination of low solvent nucleophilicity and the steric effect of large side-groups, both of which dampen the coupling between the solvent and solute. The trends in vibrational lifetime and IVR in the cation radical resemble those observed in excited ^{3}MLCT states of other transition metal complexes. This work shows how electronic structure changes and charge redistribution initiated by electronic absorption can be modeled to some extent using ground state species in conjunction with chemical modifications. Using oxidation and reduction to alter solute-solvent coupling will likely become a powerful tool for studying structure and dynamics as well as chemical reactivity, especially when controlled using electrochemistry rather than relying upon chemical redox reactions.

References

1. Santanilla, A. B.; Regalado, E. L.; Pereira, T.; Shevlin, M.; Bateman, K.; Campeau, L. C.; Schneeweis, J.; Berritt, S.; Shi, Z. C.; Nantermet, P.; Liu, Y.; Helmy, R.; Welch, C. J.; Vachal, P.; Davies, I. W.; Cernak, T.; Dreher, S. D., Nanomole-scale high-throughput chemistry for the synthesis of complex molecules. *Science* **2015,** *347*, 49-53.

2. Maroncelli, M.; Fleming, G. R., Comparison of Time-Resolved Fluorescence Stokes Shift Measurements to a Molecular Theory of Solvation Dynamics. *J Chem Phys* **1988,** *89*, 875-881.

3. Asbury, J. B.; Wang, Y. Q.; Lian, T. Q., Time-Dependent Vibration Stokes Shift During Solvation: Experiment and Theory. *B Chem Soc Jpn* **2002,** *75*, 973-983.

4. Fleming, G. R.; Cho, M. H., Chromophore-Solvent Dynamics. *Annu Rev Phys Chem* **1996,** *47*, 109-134.

5. Castner, E. W.; Maroncelli, M.; Fleming, G. R., Subpicosecond Resolution Studies of Solvation Dynamics in Polar Aprotic and Alcohol Solvents. *J Chem Phys* **1987,** *86*, 1090-1097.

6. Baiz, C. R.; Kubarych, K. J., Ultrafast Vibrational Stark-Effect Spectroscopy: Exploring Charge-Transfer Reactions by Directly Monitoring the Solvation Shell Response. *J Am Chem Soc* **2010,** *132*, 12784-12785.

7. Brookes, J. F.; Slenkamp, K. M.; Lynch, M. S.; Khalil, M., Effect of Solvent Polarity on the Vibrational Dephasing Dynamics of the Nitrosyl Stretch in an Fe-II Complex Revealed by 2D IR Spectroscopy. *J. Phys. Chem. A* **2013,** *117*, 6234-6243.

8. Huber, C. J.; Anglin, T. C.; Jones, B. H.; Muthu, N.; Cramer, C. J.; Massari, A. M., Vibrational Solvatochromism in Vaska's Complex Adducts. *J. Phys. Chem. A* **2012,** *116*, 9279-9286.

9. Jones, B. H.; Huber, C. J.; Massari, A. M., Solvation Dynamics of Vaska's Complex by 2D-IR Spectroscopy. *J. Phys. Chem. C* **2011,** *115*, 24813-24822.

10. Jones, B. H.; Huber, C. J.; Massari, A. M., Solvent-Mediated Vibrational Energy Relaxation from Vaska's Complex Adducts in Binary Solvent Mixtures. *J. Phys. Chem. A* **2013,** *117*, 6150-6157.

11. Jones, B. H.; Huber, C. J.; Spector, I. C.; Tabet, A. M.; Butler, R. L.; Hang, Y.; Massari, A. M., Correlating solvent dynamics and chemical reaction rates using binary solvent mixtures and two-dimensional infrared spectroscopy. *J. Chem. Phys.* **2015,** *142*, 212441.

12. Jones, B. H.; Massari, A. M., Origins of Spectral Broadening in Iodated Vaska's Complex in Binary Solvent Mixtures. *J. Phys. Chem. B* **2013,** *117*, 15741-15749.

13. Bandoli, G.; Dolmella, A., Ligating Ability of 1,1 '-bis(diphenylphosphino)ferrocene: a Structural Survey (1994-1998). *Coordin Chem Rev* **2000,** *209*, 161-196.

14. Fihri, A.; Meunier, P.; Hierso, J. C., Performances of Symmetrical Achiral Ferrocenylphosphine Ligands in Palladium-Catalyzed Cross-Coupling Reactions: A Review of Syntheses, Catalytic Applications and Structural Properties. *Coordin Chem Rev* **2007,** *251*, 2017-2055.

15. Zeng, M. F.; Du, Y. J.; Shao, L. J.; Qi, C. Z.; Zhang, X. M., Palladium-Catalyzed Reductive Homocoupling of Aromatic Halides and Oxidation of Alcohols. *J Org Chem* **2010,** *75*, 2556-2563.

16. Qi, C. Z.; Sun, X. D.; Lu, C. Y.; Yang, J. Z.; Du, Y. J.; Wu, H. J.; Zhang, X. M., Palladium Catalyzed Reductive Homocoupling Reactions of Aromatic Halides in Dimethyl Sulfoxide (DMSO) Solution. *Journal of Organometallic Chemistry* **2009,** *694*, 2912-2916.

17. Young, D. J.; Chien, S. W.; Hor, T. S. A., 1,1 '-Bis(diphenylphosphino)ferrocene in Functional Molecular Materials. *Dalton T* **2012,** *41*, 12655-12665.

18. Lee, T. K. M.; Cheng, E. C. C.; Zhu, N. Y.; Yam, V. W. W., Hexanuclear Gold(I) Phosphide Complexes as Platforms for Multiple Redox-Active Ferrocenyl Units. *Chem-Eur J* **2014,** *20*, 304-310.

19. Reichardt, C., Solvatochromic Dyes as Solvent Polarity Indicators. *Chem Rev* **1994,** *94*, 2319-2358.

20. Reichardt, C., Solvatochromic Dyes as Empirical Indicators of Solvent Polarity. *Chimia* **1991,** *45*, 322-324.

21. Kiefer, L. M.; King, J. T.; Kubarych, K. J., Equilibrium Excited State Dynamics of a Photoactivated Catalyst Measured with Ultrafast Transient 2DIR. *J Phys Chem A* **2014,** *118*, 9853-9860.

22. Kiefer, L. M.; Kubarych, K. J., Solvent-Dependent Dynamics of a Series of Rhenium Photoactivated Catalysts Measured with Ultrafast 2DIR. *J Phys Chem A* **2015,** *119*, 959-965.

23. El Khoury, Y.; van Wilderen, L. J. G. W.; Bredenbeck, J., Ultrafast 2D-IR Spectroelectrochemistry of Flavin Mononucleotide. *J Chem Phys* **2015,** *142,* 212146.

24. Lotti, D.; Hamm, P.; Kraack, J. P., Surface-Sensitive Spectro-Electrochemistry Using Ultrafast 2D ATR IR Spectroscopy. *J Phys Chem C* **2016,** *120*, 2883-2892.

25. Dessy, R. E.; Bares, L. A., Organometallic Electrochemistry. *Accounts of Chemical Research* **1972,** *5*, 415-421.

26. Dessy, R. E.; Stary, F. E.; King, R. B.; Waldrop, M., Organometallic Electrochemistry .4. Transition Series. *J Am Chem Soc* **1966,** *88*, 471-476.

27. Gloaguen, F.; Rauchfuss, T. B., Small molecule mimics of hydrogenases: hydrides and redox. *Chem Soc Rev* **2009,** *38*, 100-108.

28. Borg, S. J.; Behrsing, T.; Best, S. P.; Razavet, M.; Liu, X. M.; Pickett, C. J., Electron transfer at a dithiolate-bridged diiron assembly: Electrocatalytic hydrogen evolution. *J Am Chem Soc* **2004,** *126*, 16988-16999.

29. Chong, D. S.; Georgakaki, I. P.; Mejia-Rodriguez, R.; Samabria-Chinchilla, J.; Soriaga, M. P.; Darensbourg, M. Y., Electrocatalysis of hydrogen production by active site analogues of the iron hydrogenase enzyme: structure/function relationships. *Dalton T* **2003**, 4158-4163.

30. Kania, R.; Stewart, A. I.; Clark, I. P.; Greetham, G. M.; Parker, A. W.; Towrie, M.; Hunt, N. T., Investigating the Vibrational Dynamics of a $17e^-$ Metallocarbonyl Intermediate Using Ultrafast Two Dimensional Infrared Spectroscopy. *Phys Chem Chem Phys* **2010,** *12*, 1051-1063.

31. Ohs, A. C.; Rheingold, A. L.; Shaw, M. J.; Nataro, C., Electrochemistry of Group VI Metal Carbonyl Compounds Containing 1,1 '-bis(diphenylphosphino)ferrocene. *Organometallics* **2004,** *23*, 4655-4660.

32. Frisch, M. J.; Trucks, G. W.; Schlegel, H. B.; Scuseria, G. E.; Robb, M. A.; Cheeseman, J. R.; Scalmani, G.; Barone, V.; Mennucci, B.; Petersson, G. A.; Nakatsuji, H.; Caricato, M.; Li, X.; Hratchian, H. P.; Izmaylov, A. F.; Bloino, J.; Zheng, G.; Sonnenberg, J. L.; Hada, M.; Ehara, M.; Toyota, K.; Fukuda, R.; Hasegawa, J.; Ishida, M.; Nakajima, T.; Honda, Y.; Kitao, O.; Nakai, H.; Vreven, T.; Montgomery Jr., J. A.; Peralta, J. E.; Ogliaro, F.; Bearpark, M. J.; Heyd, J.; Brothers, E. N.; Kudin, K. N.; Staroverov, V. N.; Kobayashi, R.; Normand, J.; Raghavachari, K.; Rendell, A. P.; Burant, J. C.; Iyengar, S. S.; Tomasi, J.; Cossi, M.; Rega, N.; Millam, N. J.; Klene, M.; Knox, J. E.; Cross, J. B.; Bakken, V.; Adamo, C.; Jaramillo, J.; Gomperts, R.; Stratmann, R. E.; Yazyev, O.; Austin, A. J.; Cammi, R.; Pomelli, C.; Ochterski, J. W.; Martin, R. L.; Morokuma, K.; Zakrzewski, V. G.; Voth, G. A.; Salvador, P.; Dannenberg, J. J.; Dapprich, S.; Daniels, A. D.; Farkas, Ö.; Foresman, J. B.; Ortiz, J. V.; Cioslowski, J.; Fox, D. J. *Gaussian 09*, Gaussian, Inc.: Wallingford, CT, USA, 2009.

33. Cotton, F. A.; Wilkinson, G.; Gaus, P. L., *Basic Inorganic Chemistry*. 3rd ed.; J. Wiley: New York, 1995.

34. Goldman, A. S.; KroghJespersen, K., Why Do Cationic Carbon Monoxide Complexes Have High C-O Stretching Force Constants and Short C-O bonds? Electrostatic Effects, not Sigma-Bonding. *J Am Chem Soc* **1996,** *118*, 12159-12166.

35. Bredenbeck, J.; Helbing, J.; Hamm, P., Labeling Vibrations by Light: Ultrafast Transient 2D-IR Spectroscopy Tracks Vibrational Modes during Photoinduced Charge Transfer. *J Am Chem Soc* **2004,** *126*, 990-991.

36. Burin, A. L.; Tesar, S. L.; Kasyanenko, V. M.; Rubtsov, I. V.; Rubtsov, G. I., Semiclassical Model for Vibrational Dynamics in Polyatomic Molecules: Investigation of Internal Vibrational Relaxation. *J Phys Chem C* **2010,** *114*, 20510-20517.

37. Uzer, T.; Miller, W. H., Theories of Intramolecular Vibrational-Energy Transfer. *Phys Rep* **1991,** *199*, 73-146.

38. Heilweil, E. J.; Cavanagh, R. R.; Stephenson, J. C., Population Relaxation of Co(v=1) Vibrations in Solution Phase Metal-Carbonyl-Complexes. *Chem Phys Lett* **1987,** *134*, 181-188.

39. Heilweil, E. J.; Cavanagh, R. R.; Stephenson, J. C., Population Relaxation of Co-Stretching Vibrations for Carbon-Monoxide on Metal-Clusters. *Journal of the Electrochemical Society* **1988,** *135*, C386-C386.

40. Delor, M.; Sazanovich, I. V.; Towrie, M.; Spall, S. J.; Keane, T.; Blake, A. J.; Wilson, C.; Meijer, A. J. H. M.; Weinstein, J. A., Dynamics of Ground and Excited State Vibrational Relaxation and Energy Transfer in Transition Metal Carbonyls. *J Phys Chem B* **2014,** *118*, 11781-11791.

41. Fedoseeva, M.; Delor, M.; Parker, S. C.; Sazanovich, I. V.; Towrie, M.; Parker, A. W.; Weinstein, J. A., Vibrational Energy Transfer Dynamics in Ruthenium Polypyridine Transition Metal Complexes. *Phys Chem Chem Phys* **2015,** *17*, 1688-1696.

42. Eckert, P. A. K., K. J., Dynamic Flexibility of Hydrogenase Active Site Models Studied with 2D-IR Spectroscopy. *J Phys Chem A* **2017,** *121*, 608-615.

43. Nilsen, I. A.; Osborne, D. G.; White, A. M.; Anna, J. M.; Kubarych, K. J., Monitoring Equilibrium Reaction Dynamics of a Nearly Barrierless Molecular Rotor using Ultrafast Vibrational Echoes. *J Chem Phys* **2014,** *141,* 134313.

44. Khalil, M.; Demirdoven, N.; Tokmakoff, A., Coherent 2D IR spectroscopy: Molecular structure and dynamics in solution. *J Phys Chem A* **2003,** *107*, 5258-5279.

45. King, J. T.; Baiz, C. R.; Kubarych, K. J., Solvent-Dependent Spectral Diffusion in a Hydrogen Bonded "Vibrational Aggregate". *J Phys Chem A* **2010,** *114*, 10590-10604.

46. Johnson, R.; Madhani, H.; Bullock, J. P., Electrochemical Oxidation of $Mo(CO)_4(LL)$ and $Mo(CO)_3(LL)(CH_3CN)$: Generation, Infrared Characterization, and Reactivity of $[Mo(CO)_4(LL)]^+$ and $[Mo(CO)_3(LL)(CH_3CN)]^+$ (LL=2,2 '-bipyridine, 1,10-phenanthroline and Related Ligands). *Inorg Chim Acta* **2007,** *360*, 3414-3423.

47. Gutmann, V., Solvent Effects on Reactivities of Organometallic Compounds. *Coordin Chem Rev* **1976,** *18*, 225-255.

48. Cataldo, F., *A Revision of the Gutmann Donor Numbers of a Series of Phosphoramides Including TEPA*. European Chemical Bulletin: 2015; Vol. 4.

49. Kiefer, L. M.; King, J. T.; Kubarych, K. J., Equilibrium Excited State Dynamics of a Photoactivated Catalyst Measured with Ultrafast Transient 2DIR. *J Phys Chem A* **2014**, *118*, 9853-9860.

50. Kiefer, L. M.; King, J. T.; Kubarych, K. J., Dynamics of Rhenium Photocatalysts Revealed through Ultrafast Multidimensional Spectroscopy. *Accounts of Chemical Research* **2015,** *48*, 1123-1130.

51. Owrutsky, J.; Raftery, D.; Hochstrasser, R., Vibrational Relaxation Dynamics In Solutions. *Annu. Rev. Phys. Chem.* **1994,** *45*, 519-555.

Chapter 3

Dynamic Flexibility of Hydrogenase Active Site Models Studied with 2D-IR

The work presented in this chapter has been published in the following papers:

Eckert, P. A.; Kubarych, K. J., Dynamic Flexibility of Hydrogenase Active Site Models Studied with 2D-IR Spectroscopy. *J Phys Chem A* **2017,** *121*, 608-615.

3.1 Introduction

As discussed in Chapter 1.3, the hydrogenase enzyme represents one of nature's challenges to molecular scientists, the challenge to engineer an efficient catalyst for the splitting of water from an earth-abundant and environmentally-benign element. To meet this challenge, physical scientists have extensively studied the hydrogenase enzyme and small-molecule mimics of its active site in an attempt to elucidate the physical principles leverage by the enzyme to achieve its highly effective performance.[1-8] A key facet of this investigation which remains incomplete is to characterize the minimal aspects of the protein matrix needed to enable catalytic activities in mimics that rival the much more complicated macromolecular assembly. There seem to be clear structural and energetic aspects of the protein environment which govern, for example, redox potentials and the proton shuttling mechanism.[9-10] Comparing the structures of model complexes with that of the natural [FeFe] hydrogenase (FeFe-hyd) active site, it is apparent that the enzyme's geometry is considerably distorted from those of the mimics, with a specific exposure of one of the iron atoms which is lacking in most of the small-molecule mimics.[11] From a dynamical perspective, recent studies of natural enzymes have found evidence for ligand flexibility at the active site.[12] In proposed mechanisms of model complexes, several studies have implicated the flexibility of the carbonyl ligands in promoting a reactive transition

state conformation, suggesting a role for dynamics in modulating the small-molecule reactivity.[13-16] The role for dynamical fluctuations is not clear, though several macromolecular constructs involving constraints imposed by cyclodextrins, dendrimers and polymers have demonstrated increased activity relative to similar compounds lacking said constraints.[17-19]

In this chapter, by investigating two related models of the FeFe-hyd active site, we address directly the issue of the molecule's flexibility in the absence of a complex interacting environment. Using 2D-IR spectroscopy we find a distinctive signature of flexibility revealed by significant spectral diffusion dynamics in nonpolar, alkane solvents. Thanks to their solubility in alkane solvents, these complexes enable spectral dynamics measurements to report on intramolecular structural fluctuations without the overwhelming solvation contribution typical in polar solvents.

(μ-pdt)[Fe(CO)$_3$]$_2$ (pdt = 1,3-propanedithiolate) (**Fig. 1A**) is an archetypical FeFe-hyd small-molecule mimic, one of the first of many small-molecule mimics investigated in

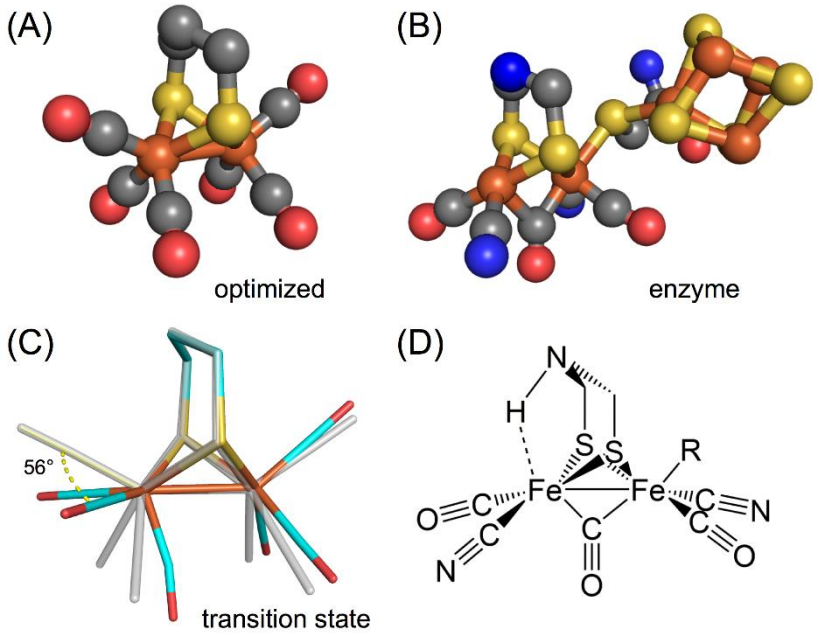

Figure 3.1: (A) The DFT optimized structure of μ-pdt-[Fe(CO)$_3$]$_2$ is essentially two-fold symmetric with respect to the carbonyl ligands. (B) The crystallographic hydrogenase enzyme active site reveals an open coordinate site where hydrogen has been shown to bind [PDB: 3C8Y] (C) The transition-state (colors) geometry superposed on the (gray) fully optimized structure shows a conformation resembling that of the enzyme. (D) A depiction of the pendant amine shuttling a proton to iron active site highlights the interrelationship between the bridge and the open coordination site. This figure was adapted from the journal article in which these results were published.

the attempt to replicate the catalytic activity of the enzyme.[13] Such mimics have been studied extensively spectroscopically. A full review of this literature is beyond the scope of this manuscript, but it includes characterization of electronic state relaxation using time-resolved vibrational spectroscopy,[20-21] carbonyl dissociation and geminate rebinding,[20-24] protonation dynamics,[6, 25] ground-state vibrational dynamics,[6, 22-26] intramolecular vibrational energy transfer,[27] and electronically induced charge transfer from an organometallic photosensitizer.[2, 28]

A comparison of the fully optimized (computational methods are described below) configurations of the diiron mimics with the hydrogenase active site reveals a subtle difference: the optimized geometries of the mimics typically position the carbonyls of both iron centers in the same orientation, resulting in an "eclipsed" geometry when viewed along the Fe–Fe bond axis. In contrast, the ligands of the distal iron of the enzyme active site are rotated 60° away from the eclipsed configuration, exposing the iron center directly beneath the bridging dithiolate ligand (**Fig. 1C**). It has been suggested that the configurational difference between the hydrogenase active site and the small-molecule mimics is a dynamic one where the carbonyl ligands on the small-molecule mimics are fluxional, switching places on the iron in a concerted "turnstile"-type rotation.[13] The transition-state geometry of this rotation resembles the geometry of the enzyme active site (**Fig. 1B**).[13] This fluxional motion is potentially spectroscopically accessible, and studies of carbonyl photodissociation and rebinding to hydrogenase mimics show vibrational peak shifts which can be attributed to turnstile-type rotation around the Fe–Fe bond axis while the carbonyl rebinds to the metal center.[22-23] A similar isomerization was suggested in a photochemical investigation of a mimic with a bridging hydride ligand.[29] These interpretations are facilitated by the fact that photodissociation generates multiple distinct isomers in solution with spectral marker bands. It is somewhat more challenging to isolate dynamics in stable complexes since fluctuations involve a single species with indistinguishable initial and final conformations connected by turnstile-like motion.

The precise role of the dithiolate linker in the enzyme active site remains open, but electronic structure calculations and synthetic efforts to recreate the enzyme strongly support the hypothesized identity of the bridging group as an azadithiolate.[9] The pendant

amine group of the azadithiolate has been hypothesized to facilitate catalysis by transporting protons to and from the exposed iron, as illustrated in **Fig. 1D**. This mechanism assigns the orientation of the ligands in the enzyme active site a key role in the catalytic cycle, since an "eclipsed" configuration of the ligands would sterically inhibit proton transport via the pendant amine. Experimental and computational studies of active site mimics suggest that a rotation of the carbonyl ligands into the transition-state geometry is a key step in general reaction mechanisms for this type of molecule regardless of the nature of the bridging dithiolate group.[14-15, 30-31] Coordination sphere mobility appears to be a central factor in reactivity, and the hydrogenase enzyme, by stabilizing the reactive 60°-rotated geometry, exemplifies a natural exploitation of this dynamic ligand mobility.

In light of the structural differences between the enzyme and the mimics, we consider two related FeFe-hyd model compounds, differing only in the dithiolate linker, to assess the degree to which these compounds are flexible. Ultrafast two-dimensional infrared (2D-IR) spectroscopy can uncover molecular flexibility most clearly when the spectral dynamics induced by solvation are negligible, which is possible using weakly perturbing nonpolar liquids such as alkanes. In nonpolar liquids, frequency fluctuations result chiefly from intramolecular distortions that anharmonically couple to the spectroscopic vibrational modes. Using 2D-IR to study (μ-edt)$[Fe(CO)_3]_2$ and (μ-pdt)$[Fe(CO)_3]_2$, (edt = ethanedithiolate) in alkane solvents, we find a clear signature of fluctuations on a picosecond timescale. A potential energy surface derived from quantum chemical calculations supports the attribution of the spectral dynamics to turnstile motion of the carbonyl ligands. These results demonstrate that dynamical coordination sphere mobility is experimentally accessible on the picosecond timescale using ultrafast 2D-IR spectroscopy even when the full barrier crossing process is too slow to observe within the vibrational lifetime. To further test our hypothesis that the spectral dynamics we observe arise from intramolecular dynamical fluctuations we perform similar measurements on a series of organometallic compounds known for their conformational mobility, $M_3(CO)_{12}$ (M = Fe, Ru, Os), and find similar spectral dynamics, supporting our hypothesis. We also observe a surprising trend in the intramolecular vibrational redistribution among the

carbonyl modes, which exhibits a solvent dependence despite the lack of any solvent dependent spectral diffusion or vibrational energy relaxation.

3.2 Experimental Methods

All chemical reactions were performed under a nitrogen atmosphere using standard Schlenk line techniques. Reagents were ordered from Sigma Aldrich and used as received. (μ-pdt)[Fe(CO)$_3$]$_2$ was received as a generous gift from Dr. Nicolai Lehnert and used as received. (μ-edt)[Fe(CO)$_3$]$_2$ was prepared according to the literature procedure.[13]

The experimental set-up described in Chapter 1.3 was used here without any significant modification.

Electronic structure calculations were performed using the Gaussian 09 package.[32] For calculations focused upon (μ-pdt)[Fe(CO)$_3$]$_2$ the BVP86 functional was employed, iron atoms were treated with the SDD pseudopotential, and the remaining atoms were treated with the all-electron basis set 6-311G(d). For calculations focused on variants of [Cr(benzene)(CO)$_3$] (BCT) the BVP86 functional was used and, the chromium atoms were treated with an SDD pseudopotential, and the remaining atoms were treated with an all-electron 6-31G(d,p) basis set.

3.3 Results

Figure 3.2a shows the FTIR spectra of (μ-pdt)[Fe(CO)$_3$]$_2$ in *n*-hexane, *n*-undecane, and *n*-hexadecane. It is clear that, apart from a slight change in the breadth of the peaks, the length of the solvent alkane has little effect upon the vibrational spectrum of the molecule. Figure 3.2b shows the structure of (μ-pdt)[Fe(CO)$_3$]$_2$ and uses arrows to represent the vibrational displacements associated with mode 2, upon which the current work focuses. Figure 3c shows an absolute-value 2D-IR spectrum of the carbonyl stretching modes of (μ-pdt)[Fe(CO)$_3$]$_2$. The quantity of peaks contained in the spectrum illustrate the richness of the data – in principle, the vibrational lifetimes and spectral diffusion timescales for each of the carbonyl stretching modes may be extracted from the spectra, as well as the rates of pair-wise IVR for all five bright vibrational modes. However, in this work we focus upon mode 2 and its cross peak with mode 3. Further exploration

of the cross peaks in the 2D-IR spectra of this class of diiron hexacarbonyl compound is reserved for Chapter 5.

Figure 3.3a depicts the spectral diffusion of mode 2 in *n*-hexane, *n*-undecane, and *n*-hexadecane, offset for clarity of viewing purposes. We note the presence of pronounced oscillatory features in the early waiting time – these are the coherences between mode 2

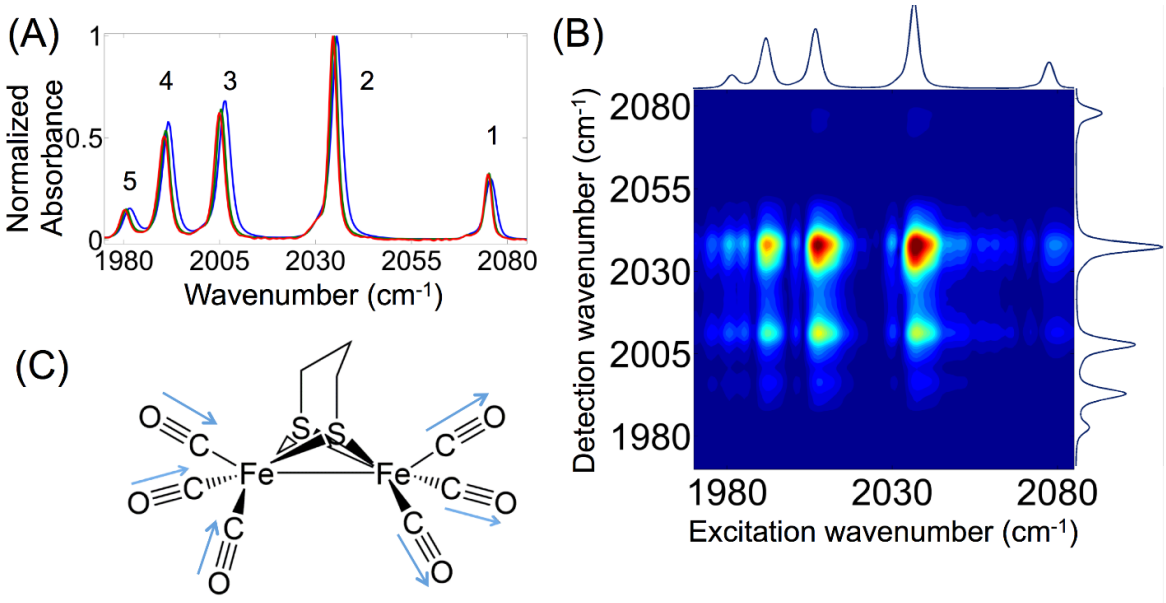

Figure 3.2: (A) FTIR of μ-pdt-$[Fe(CO)_3]_2$ in hexane, undecane, and hexadecane. The mode numbering scheme detailed in Chapter 1.3 is recapitulated here. (B) Absolute value 2D-IR rephasing spectrum of μ-pdt-$[Fe(CO)_3]_2$ in hexane, tuned to mode 2. The intense cross peaks reflect coupling between the carbonyl modes. (C) Structure of (μ-pdt)$[Fe(CO)_3]_2$ with arrows indicating the out-of-phase symmetric carbonyl displacements of mode 2. This figure was adapted from the journal article in which these results were published.

and the other bright modes in the spectrum, and are an unavoidable aspect of data collected with our experimental set-up. To minimize the effect of these coherent oscillatory features we find a moving average of each data series and superpose it on the raw data along with the best fit to our data. Each data series is well fit by a single exponential decay, and the time constants of each decay are within error and essentially indistinguishable.

Figure 3.3b shows a comparison of the spectral diffusion of (μ-pdt)$[Fe(CO)_3]_2$ and (μ-edt)$[Fe(CO)_3]_2$ in a solvent of *n*-undecane. The spectral diffusion of (μ-edt)$[Fe(CO)_3]_2$ is slightly slower than that of (μ-pdt)$[Fe(CO)_3]_2$, but the difference is marginal. Figure 3.3c shows a comparison of the vibrational lifetimes of mode 2 of (μ-pdt)$[Fe(CO)_3]_2$ in *n*-

hexane, *n*-undecane, and *n*-hexadecane, all of which are well fit by a biexponential decay model. Although the fast decay component of each data series differ slightly, indicating

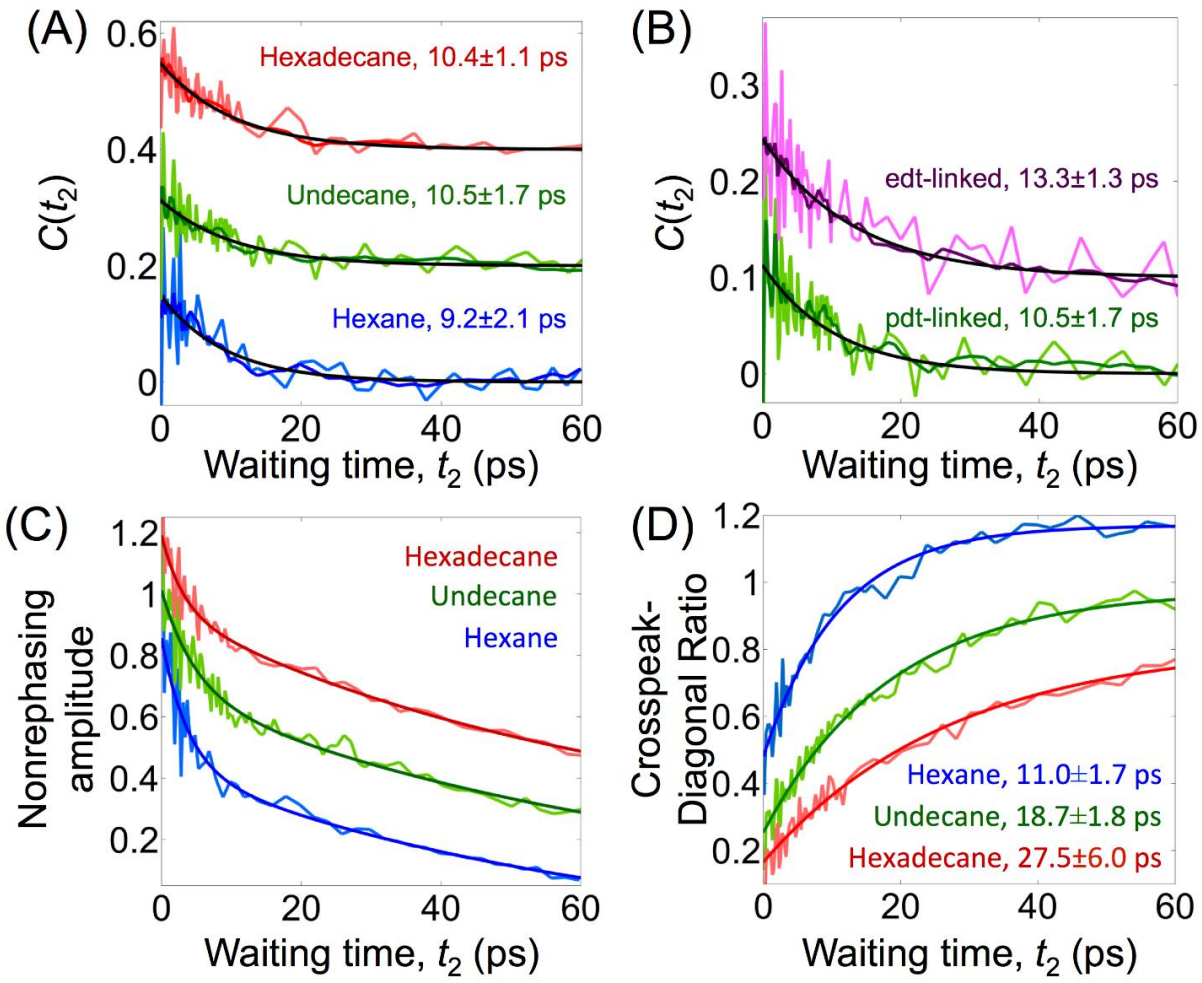

Figure 3.3: (In all panels, curves are offset for clarity) (A) Frequency-fluctuation correlation functions, $C(t_2)$, for (μ-pdt)[Fe(CO)$_3$]$_2$ in hexane, undecane, and hexadecane yield essentially indistinguishable decay constants. The oscillatory features appearing during the first 15 ps result from vibrational coherences among the excited CO modes. The data has been offset for clarity of display. (B) A comparison of the FFCFs for (μ-pdt)[Fe(CO)$_3$]$_2$ and (μ-edt)[Fe(CO)$_3$]$_2$ in undecane shows a slight slowdown in the case of the edt linker. The data has been offset for clarity of display. (C) The nonrephasing signal amplitude obtained by integrating the peak 2 diagonal of (μ-pdt)[Fe(CO)$_3$]$_2$ in hexane, undecane, and hexadecane shows indistinguishable long-time decays due to vibrational energy relaxation. The data have been offset for clarity of display. (D) Ratios of crosspeak (ω_{excite} = 2015 cm^{-1}, ω_{detect} = 2038 cm^{-1}) and mode 2 amplitudes for (μ-pdt)[Fe(CO)$_3$]$_2$ in hexane, undecane, and hexadecane show significant solvent-dependent IVR timescales. The IVR timescales depend linearly on solvent carbon chain length: $\tau_{IVR} = n \times 1.65$ ps + 0.92 ps. The data have been offset for clarity of display. This figure was adapted from the journal article in which these results were published.

different fast IVR dynamics during the first several picoseconds post-excitation, the slow component of the fit is essentially indistinguishable between the three solvents, indicating that the overall process of IVR, as reflected by the relaxation of the carbonyl vibration, is

unaffected by the solvent. Finally, Figure 3.3d shows the cross peak IVR timescales of the cross peak excited at mode 3 and detected at mode 2, (ω_1 = 2010 cm^{-1}, ω_3 = 2038 cm^{-1}) , which display an almost linear dependence upon the chain length of the alkane solvent.

Figure 3.4 shows the result of a series of electronic structure calculations. The molecular geometries of a series of variants of BCT were optimized, and for each the hydrogen on the 1, 3, and 5 carbons was replaced with an electron-withdrawing functional

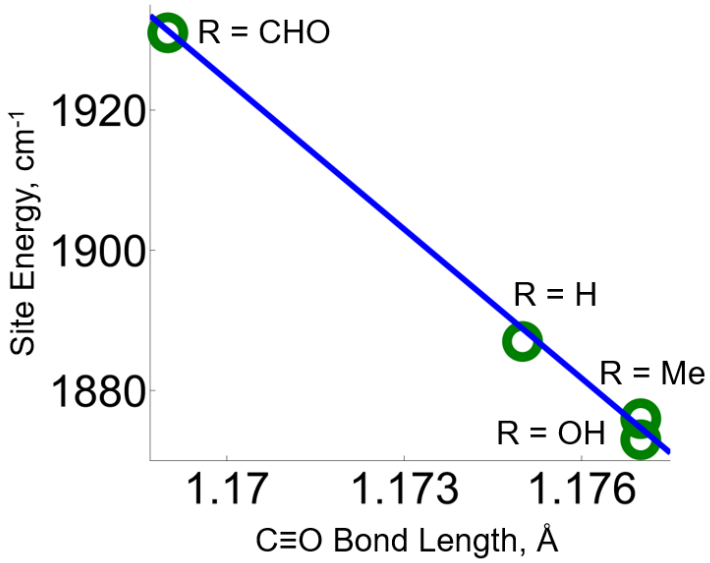

Figure 3.4: Plot of C≡O site energy vs. C≡O bond length in a series of variants of BCT which were symmetrically tri-substituted at the 1, 3, and 5 positions. The R groups are labeled on the plot. The line of best fit is given by (Site Energy, cm^{-1}) = (-7081 $\frac{\text{cm}^{-1}}{\text{Å}}$) × (C≡O Bond Length, Å) + 10280 cm^{-1}. This figure was adapted from the journal article in which these results were published.

group. The vibrational frequency of each local carbonyl mode is identical for symmetric variants of BCT, and the vibrational frequency of the local carbonyl mode for each molecule was plotted against the C≡O bond length of the optimized geometry. The data series, shown in Figure 3.4, shows a clear inverse correlation, suggesting that as the C≡O bond length of a carbonyl local mode increases its vibrational frequency will undergo a corresponding decrease.

3.4 Discussion

Spectral diffusion is caused by fluctuations in the potential energy surface of a vibrational mode.[33-34] In polar solvents and complex surroundings, these fluctuations are

typically caused by variations in the local electrostatic environment and intermolecular interactions, of which hydrogen bonding is a common example. We have catalogued the spectral diffusion dynamics of several metal carbonyl complexes in various solvents, and sometimes find a trend that can be explained by the solvent's macroscopic dynamical properties, such as viscosity. For example, in an alcohol (methanol to 1-hexanol) series we found a linear relationship between the timescale of metal carbonyl spectral diffusion and solvent viscosity for $Mn_2(CO)_{10}$, $CpMn(CO)_3$, and $CpMn(CO)_3$ complexed to cyclodextrin.[35-36] In a rhenium photocatalyst, on the other hand, we found a distinct *lack* of viscosity dependence across the solvents THF, DMSO, and acetonitrile, but a clear linear correlation with the donor number (i.e. nucleophilicity).[37] These kinds of intermolecular origins for spectral diffusion are largely absent in alkane solvents because they are nonpolar. Interactions with nonpolar liquids are largely collisional, or mediated by polarizability, and solvent fluctuations do not induce significant electrostatic fluctuations that generally dominate spectral diffusion.[37-38] The hypothesis of an intermolecular origin for the frequency fluctuations is further weakened by the insensitivity of the spectral diffusion timescale to solvent viscosity. **Figure 3A** shows the FFCF decays of μ-pdt-$[Fe(CO)_3]_2$ in hexane, undecane, and hexadecane, which have viscosities of 0.300, 1.098, and 3.03 cP. Though the viscosities and alkane chain lengths of the solvents are appreciably different, the timescales of spectral diffusion are indistinguishable. The lack of solvent dependence suggests a primarily intramolecular origin for the apparent spectral fluctuations. We previously observed a similar intramolecular origin for spectral diffusion due to the torsional dynamics of the piano stool complex BCT, which also exhibits solvent-independent spectral diffusion in alkanes.[39]

The complex (μ-pdt)$[Fe(CO)_3]_2$ is a flexible molecule, and has two primary modes of fluxionality. One type of motion involves the propane linking group "flipping" from one side of the molecule to the other along the Fe-Fe bond axis with an activation energy of 9.63±0.24 kcal/mol, as determined by Crouthers et. al using temperature-dependent NMR.[16] The other is a "turnstile"-type rotation of one $Fe(CO)_3$ group roughly around the Fe-Fe bond axis, with an activation energy of 9.86±0.24 kcal/mol, based on variable-temperature NMR measurements.[16] Both have similar energy barriers, and both could

conceivably induce fluctuations in the carbonyl vibrational mode frequencies. To determine whether such a flipping of the propyl linking group contributes to carbonyl spectral diffusion, we synthesized (μ-edt)[Fe(CO)$_3$]$_2$, which is a variant with no flexible methylene linkage. Spectral diffusion in mode 2 of (μ-edt)[Fe(CO)$_3$]$_2$ is nevertheless apparent (Fig. 3B), exhibiting a spectral diffusion timescale of 13.3±1.3 ps in undecane, which is about 30% slower than the timescale of the propyl-linked variant. We note that the energy barrier to rotation of the Fe(CO)$_3$ rotor in the ethyl-linked mimic is ~2 kcal/mol higher than that of the propyl-linked mimic.[40] The slightly longer timescale of spectral diffusion in the ethyl-linked mimic thus provides strong indirect support for the hypothesis that the spectral diffusion of the carbonyl bands is significantly influenced by twisting dynamics of the Fe(CO)$_3$ rotors as well as implying that fluxionality of the propyl linker is not primarily responsible for the spectral diffusion.

Chemical modification of (μ-pdt)[Fe(CO)$_3$]$_2$ to inhibit any turnstile-type rotation is substantially more complicated than changing the propyl linker, so to determine the nature of the energy barrier to turnstile-type rotation, we turn to computational modeling. We

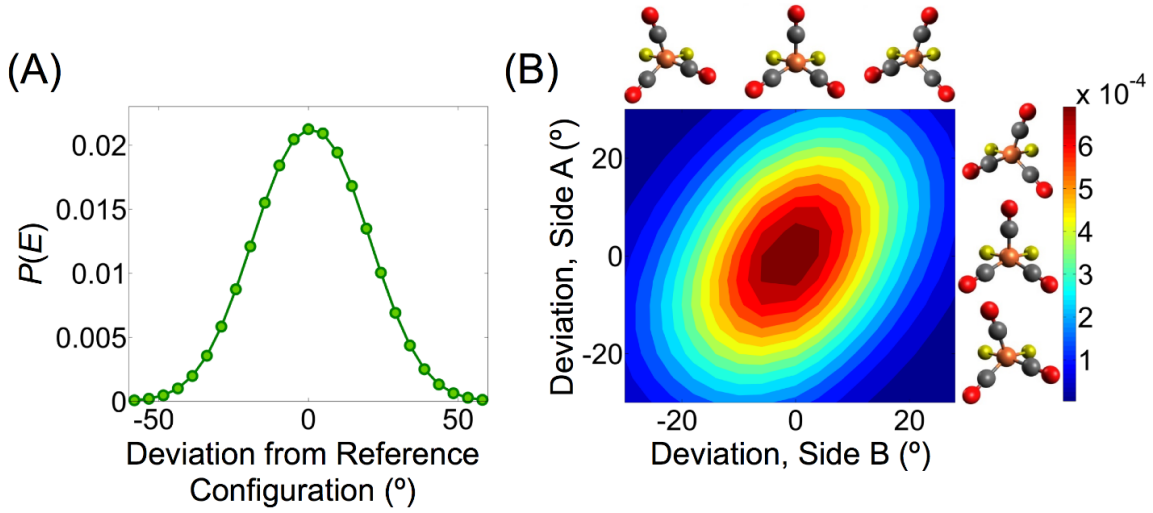

Figure 3.5: (A) The Boltzmann distribution of torsional angles for (μ-pdt)[Fe(CO)$_3$]$_2$ as a function of Fe(CO)$_3$ rotor twist shows significant structural distortion is present at room temperature. (B) Boltzmann distribution of conformations as a function of both Fe(CO)$_3$ rotor twists indicate that the two angles are correlated. This figure was adapted from the journal article in which these results were published.

performed a relaxed energy scan of the turnstile dihedral with geometry optimization starting at the transition state, passing through the optimized geometry, and ending at the

next transition state. All other degrees of freedom were fully optimized. The Boltzmann distribution of states can be calculated according to Eq. 3.1,

$$P(E) = \frac{e^{\frac{-E}{k_B T}}}{\int e^{\frac{-E}{k_B T}} dE} \tag{3.1}$$

where E is the potential energy of the molecule, $P(E)$ is the probability of occupying state E, k_B is Boltzmann's constant, and T is 298 K. The one- and two-dimensional Boltzmann distribution of states are shown in **Figure 5**, where the eclipsed carbonyl configuration is denoted as the "reference" configuration. The Boltzmann distribution for (μ-pdt)[Fe(CO)$_3$]$_2$ (Fig. 5A) has a second moment of almost 20° from the reference "eclipsed" configuration, indicating that there is substantial thermal population of many possible geometries. At equilibrium, the complex therefore samples among these thermally accessible conformations. Although simplistic harmonic frequency calculations cannot capture the fluctuations in the CO stretching vibrations as the conformations are sampled, it is reasonable to expect that the CO frequencies will change as the ligands fluctuate.

To determine whether the molecular rotations influence the stretching frequency of the carbonyls on (μ-pdt)[Fe(CO)$_3$]$_2$, we considered the C≡O bond length for three carbonyls on (μ-pdt)[Fe(CO)$_3$]$_2$. An empirical relationship between bond length and vibrational frequency known as Badger's rule exists for some diatomics,[41] and while no such simple linear mapping is known for carbonyl ligands, there is typically a direct relationship between CO bond lengths and frequencies in metal carbonyls. Carbonyl ligands bond to metal atoms by receiving electron density from the metal into π* antibonding orbitals, so an elongation or contraction of C≡O bond length during the rotation implies a change in the electronic coupling between the carbonyl unit and the metal atom, and a corresponding modulation of the vibrational potential energy surface.[42-43]

Structural changes accompanying the rotation to the transition state are depicted in **Fig. 6**. Relative to the optimized, eclipsed structure, the transition state structure shows elongation of the rotating carbonyls, and contraction of the non-rotating ligands. As expected for back bonding, the Fe-C distance changes are anti-correlated with the CO

distance changes. That is, the Fe-C bonds shorten for the rotating ligands, whereas they lengthen for the non-rotating ligands. The effect of the rotation is to break the energetic symmetry of the CO units. Since there is a general rule for metal carbonyls that shorter CO distances indicate higher frequencies, the non-rotating COs are expected to blue shift, whereas the rotating COs red shift with respect to the reference optimized geometry.

Although we cannot be certain of the extent of the frequency shifts, we can compare with model compounds where we alter the metal-carbonyl bonding remotely by

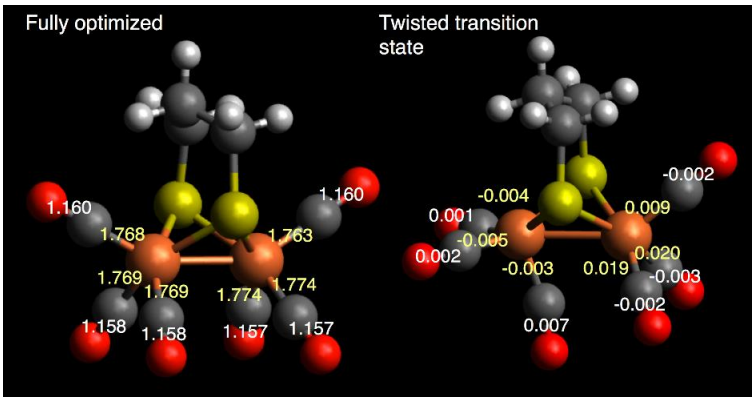

Figure 3.6: (left) The fully optimized structure with bond distances depicted in units of Å; Fe-C are in yellow and C-O are in white. (right) The twisted transition state structure showing the changes in the bond distances relative to the optimized geometry (twisted – optimized). This figure was adapted from the journal article in which these results were published.

modulating the electron withdrawing nature of an aromatic ligand without causing qualitative changes to the metal carbonyl structure. An ideal possibility for such analysis is BCT, which can be substituted with electron-donating and electron-withdrawing organic groups on the benzene ring to modulate the electron density of the chromium atom. This modulation was performed for several variants of BCT, and the tricarbonyl site was modeled as a vibrational aggregate. Vibrational energies for the C≡O local modes, corresponding to aggregate site energies, were found by preparing the three-site Hamiltonian presented in Equation 3.2,

$$H = \begin{pmatrix} s & j & j \\ j & s & j \\ j & j & s \end{pmatrix} \tag{3.2}$$

where the site energy of each carbonyl is represented with an *s* on the diagonal of the matrix, and each site coupling is represented by an off-diagonal *j*, since each site is identical

due to the symmetry of the molecule. For such systems the Hamiltonian is analytically soluble, with eigenvalues given by Equations 3.3-3.4,

$$\epsilon_{1,2} = s + j \tag{3.3}$$

$$\epsilon_3 = s + 2j \tag{3.4}$$

The Hamiltonian given in Equation 3.2 was solved for each variant of BCT, and results are shown in Figure 3.4. The carbonyl local mode frequencies blue shift by ~ 7 cm^{-1} for each 1 mÅ of bond contraction. Given that in the transition state we find a roughly 15 cm^{-1} frequency shift of the modes that resemble 1 and 2 from the optimized geometry, we can be confident that partial rotation would produce frequency shifts of several wavenumbers. This degree of conformationally-induced inhomogeneous broadening is consistent both with our FTIR spectral widths and with the observation of spectral diffusion. Based on the potential energy surface shown in Fig. 4, the carbonyls sample roughly one-third of the angle space, so we can estimate the range of frequencies to be about 5 cm^{-1}, which agrees remarkably well with our observed FTIR line widths.

Conformational mobility is not uncommon in organometallic complexes, and some degree of flexibility is expected for most molecules. If the spectral diffusion observed in (μ-pdt)$[Fe(CO)_3]_2$ is a reflection of hindered conformational flexibility, similar dynamics should be expected to characterize other flexible organometallic complexes. To further test the hypothesis that spectral diffusion in alkane solvents may reflect molecular flexibility we turn to $Ru_3(CO)_{12}$ and $Os_3(CO)_{12}$. In both of these complexes the metal atoms lie on the vertices of an equilateral triangle and four carbonyl groups are bonded to each metal atom. $Ru_3(CO)_{12}$ is conformationally mobile and the carbonyl groups on each ruthenium atom undergo exchange with an activation energy of ~ 4 kcal/mol,[44] which is a low enough energy barrier that signatures of the self-isomerization could conceivably be accessible on our experimental timescale. The activation energy for similar self-isomerization in $Os_3(CO)_{12}$, ~ 16 kcal/mol,[45] is far too high for any spectral signatures of such isomerization to be significant in our experimental timescale. $Os_3(CO)_{12}$ is sparingly soluble at best in essentially every solvent we tested, but both compounds are sufficiently soluble in alkane solvents for data acquisition using our experimental set-up.

The infrared spectra of $Ru_3(CO)_{12}$ and $Os_3(CO)_{12}$ are shown in Figure 3.7a. Both

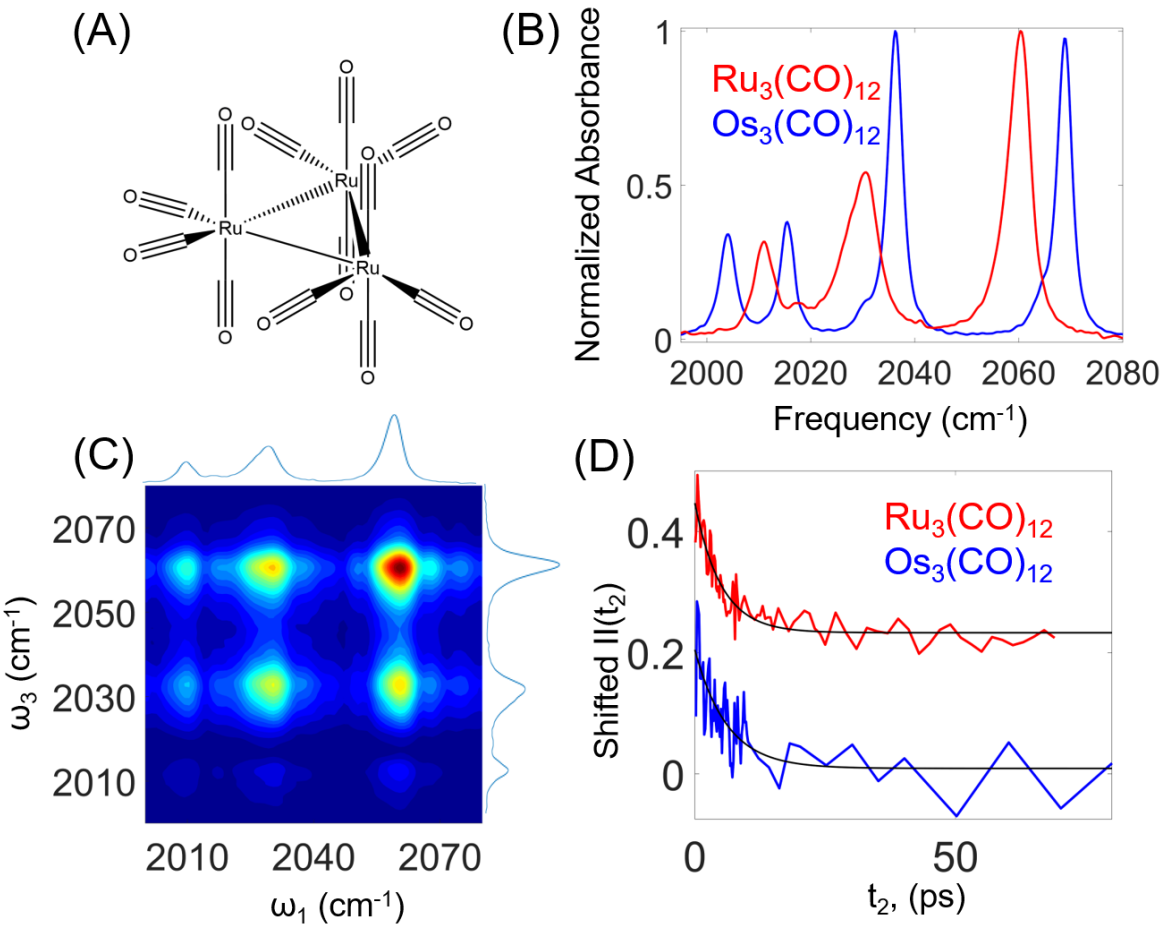

Figure 3.7: (A) Molecular geometry of $Ru_3(CO)_{12}$. $Os_3(CO)_{12}$ has the same molecular structure. (B) FTIR spectra of $Ru_3(CO)_{12}$ and $Os_3(CO)_{12}$ in dodecane and heptane, respectively. The vibrational bands investigated further are the second-highest frequency band in both spectra, at frequencies of 2031 cm^{-1} in $Ru_3(CO)_{12}$ and 2036 cm^{-1} in $Os_3(CO)_{12}$. (C) 2D-IR spectrum of $Ru_3(CO)_{12}$ in dodecane, with FTIR spectra set across from the excitation and detection axes. (D) Spectral diffusion of vibrational bands at frequencies of 2031 cm^{-1} in $Ru_3(CO)_{12}$ and 2036 cm^{-1} in $Os_3(CO)_{12}$. Although exact fitting is obfuscated by the pronounced vibrational coherences in $Os_3(CO)_{12}$, both data series are well fit by an exponential decay with a single time constant of ~ 5 ps.

compounds are predicted to have 12 carbonyl stretching vibrational modes, but many of these vibrations are dark and/or degenerate due to the high degree of molecular symmetry in both complexes. The vibrational mode selected for analysis here corresponds in both molecules to an out-of-phase stretching of all six apical carbonyl groups, and is the peak at in $Ru_3(CO)_{12}$ and at in $Os_3(CO)_{12}$. The spectral diffusion data collected for the vibrational modes at 2031 cm^{-1} in $Ru_3(CO)_{12}$ and at 2036 cm^{-1} in $Os_3(CO)_{12}$ is shown in Figure 3.7b, shifted along y-axis for clarity of viewing. Although the pronounced

vibrational coherences in $Os_3(CO)_{12}$ obfuscate the early waiting-time data, spectral diffusion is evident in both data series, and both of them are well fit by single exponential decays on the timescale of ~ 5 ps. The presence of comparable spectral diffusion dynamics in $Ru_3(CO)_{12}$ and $Os_3(CO)_{12}$, both of which are known to be conformationally mobile on very different timescales, provides support for our hypothesis that the fluctuations of the carbonyl potential observed in (μ-pdt)$[Fe(CO)_3]_2$ have an intramolecular origins, and are reflective of the flexibility of the molecule at room temperature. The comparable timescale of spectral diffusion in both the ruthenium and osmium complexes, despite the significant difference in the potential energy landscape of the molecular geometry evidenced by the much lower barrier to self-isomerization raises the question of how exactly the timescale of spectral diffusion may be mapped to the dynamical flexibility of a molecule's geometry. This question is underlined by the case of (μ-pdt)$[Fe(CO)_3]_2$ in which the 10 kcal/mol barrier to self-isomerization lies between that of $Ru_3(CO)_{12}$ and $Os_3(CO)_{12}$, which are 4 kcal/mol, and 16 kcal/mol, respectively, even though the timescale of spectral diffusion in (μ-pdt)$[Fe(CO)_3]_2$, 10 ps, is double that of both the ruthenium and osmium complexes. Further investigation toward characterizing the effect of conformational flexibility on the frequencies of molecular vibrations is clearly necessary, especially given the potential relevance conformational flexibility to molecular reactivity.

To our knowledge, the only previous measurement of carbonyl ligand spectral diffusion on a small-molecule mimic of the [FeFe]-hydrogenase active site was performed on (μ-$C(CH_3)(CH_2S)_2(CH_2S(CH_2)_2Ph)Fe_2(CO)_5$ in 1,7-heptanediol, and the spectral diffusion data was fit to a bi-exponential function with time constants of 3 and 70 ps.[26] Covalently bonding the bridging group to one of the $Fe(CO)_3$ rotors and adding a strongly interacting alcohol solvent is expected to have a complex interaction with both the overall molecular flexibility and the carbonyl spectral diffusion, which makes a detailed comparison to our data somewhat difficult. Moreover, the polar and rather complex solvent used in that study would induce significant solvation dynamics as well as inhomogeneous broadening, making it difficult to isolate the intramolecular contribution to the spectral diffusion. A mimic of the [FeFe]-hydrogenase active site has also been incorporated into a metal-organic framework (MOF) and measurements of its spectral

diffusion were used to assess the degree of flexibility of the macromolecular assembly.[46] Extremely long spectral diffusion timescales (670 and >2000 ps) were reported for the spectral diffusion of the carbonyl ligands in the absence of, and in the presence of, DMF solvent. Interestingly, for the reported control study of the small-molecule mimic when not incorporated into MOF, the timescale of spectral diffusion was 16±1 ps, which given the polar solvent and differing dithiolate linker is consistent with the 13±1 ps time constant we find for the edt-linked mimic in undecane.

A more indirect measurement of the Fe rotor's flexibility has been reported via photo-dissociation of a CO ligand from (μ-pdt)[$Fe(CO)_2$(PMe)]$_2$. Rotation of the ligands around the Fe-Fe bond axis appears to be favored during geminate rebinding of the dissociated carbonyl to the iron, as evidenced by increased population of the thermodynamically unfavored *trans*-PMe configuration following geminate rebinding.[23] This measurement does require populations of two isomeric forms, the *cis* and *trans* configurations, to monitor rotation of the $Fe(CO)_2$(PMe) rotor via isomerization.

The solvent-insensitivity of mode 2's spectral diffusion suggests that the timescale of the $Fe(CO)_3$ rotor's torsional motion is not substantially influenced by the viscosity of the alkane solvent. Vibrational relaxation of mode 2 in the alkane solvent series measured using the nonrephasing diagonal peak amplitude is shown in **Fig. 3C**. In all solvents the decay is well fit by the sum of a fast and a slow exponential decay, with a fast timescale of roughly 4 ps, and a long time-constant of roughly 60 ps. Though the degree of early-time relaxation is solvent-dependent, the long-time vibrational relaxation of mode 2 displays the same solvent-insensitivity as the spectral diffusion. However, we find different trends in the IVR of (μ-pdt)[$Fe(CO)_3$]$_2$. **Figure 3D** shows the ratio of the cross peak between modes 2 and 3 (ω_{excite} = 2015 cm^{-1}, ω_{detect} = 2038 cm^{-1}) and the diagonal peak corresponding to mode 2 (2015 cm^{-1}) in the alkane series. The time scale for energy randomization between modes 2 and 3 increases monotonically with increasing solvent alkane chain length, in contrast to the consistent vibrational relaxation and spectral diffusion of mode 2.

We previously found the experimentally determined rate of IVR between two carbonyl modes of $Mn_2(CO)_{10}$ in a series of alcohol solvents to directly correlate with the

average number of hydrogen bonds formed between a $Mn_2(CO)_{10}$ molecule and the corresponding alcohol solvent in a series of molecular dynamics simulations.[47] That study attributed the solvent-hindered IVR to a scenario where hydrogen bonding acts to trap vibrational energy within specific vibrational modes of the solute. Banno et. al. reported a similar dependence of vibrational relaxation upon the carbon number of an alkane solvent for $W(CO)_6$, which has a single, triply degenerate carbonyl stretching band. The vibrational relaxation of that band was fit to a sum of three exponential decays, and it was found that one of timescales increased monotonically with solvent carbon number in a manner quite similar to what we report.[48] Banno et. al. attribute this to a slow-down of rotational diffusion due to increased solvent viscosity. Though alkanes are much more weakly interacting than alcohols, our data suggests that even the weak van der Waals interactions and elastic collisions which dominate intermolecular interactions in alkane solvents may exert a measurable influence upon the dynamics of intramolecular vibrational energy randomization, while still not altering vibrational relaxation or the torsional twisting of the $Fe(CO)_3$ rotors. Further study is necessary to elucidate the coupling between IVR and intramolecular flexibility and hindered fluxionality.

3.5 Conclusion

We report the first 2D-IR investigation of molecular flexibility through the decay of a vibration's spectral inhomogeneity, and we relate this flexibility directly to a catalytically-relevant mode of molecular self-isomerization in small-molecule mimics of the hydrogenase enzyme active site. We observe similar spectral inhomogeneity decay in other organometallic complexes, one of which is known to the conformationally mobile on a picosecond timescale, supporting our hypothesis that conformational flexibility may indeed induce a significant spectral inhomogeneity and a decay thereof. Further work is necessary to determine exactly how the timescale of spectral inhomogeneity decay maps to the dynamics associated with the molecular flexibility it reflects. We expect that this work will be directly relevant to the study of organometallic molecules and active sites in relatively non-polar environments, like those of alkane solvents or of active site pockets in proteins and enzymes. We note also a surprising dependence of the timescale of early

intercarbonyl IVR processes on the chain-length of the alkane solvent, suggesting a close coupling of the solvent to the dynamics of the carbonyl groups which is not reflected in the vibrational relaxation or spectral diffusion of the carbonyl vibrations. Further work is also required to investigate this highly unexpected result.

References

1. Onoda, A.; Hayashi, T., Artificial Hydrogenase: Biomimetic Approaches Controlling Active Molecular Catalysts. *Curr Opin Chem Biol* **2015,** *25*, 133-140.

2. Li, P.; Amirjalayer, S.; Hartl, F.; Lutz, M.; de Bruin, B.; Becker, R.; Woutersen, S.; Reek, J. N. H., Direct Probing of Photoinduced Electron Transfer in a Self-Assembled Biomimetic [2Fe2S]-Hydrogenase Complex Using Ultrafast Vibrational Spectroscopy. *Inorg Chem* **2014,** *53*, 5373-5383.

3. Fritzsch, R.; Brady, O.; Adair, E.; Wright, J. A.; Pickett, C. J.; Hunt, N. T., Encapsulating Subsite Analogues of the [FeFe]-Hydrogenases in Micelles Enables Direct Water Interactions. *J Phys Chem Lett* **2016,** *7*, 2838-2843.

4. Ghosh, S.; Hogarth, G.; Hollingsworth, N.; Holt, K. B.; Kabir, S. E.; Sanchez, B. E., Hydrogenase Biomimetics: $Fe_2(CO)_4$(mu-dppf)(mu-pdt) (dppf=1,1 '-bis(diphenylphosphino)ferrocene) both a Proton-Reduction and Hydrogen Oxidation Catalyst. *Chem Commun* **2014,** *50*, 945-947.

5. Simmons, T. R.; Berggren, G.; Bacchi, M.; Fontecave, M.; Artero, V., Mimicking Hydrogenases: From Biomimetics to Artificial Enzymes. *Coordin Chem Rev* **2014,** *270*, 127-150.

6. Liu, Y. C.; Chu, K. T.; Huang, Y. L.; Hsu, C. H.; Lee, G. H.; Tseng, M. C.; Chiang, M. H., Protonation/Reduction of Carbonyl-Rich Diiron Complexes and the Direct Observation of Triprotonated Species: Insights into the Electrocatalytic Mechanism of Hydrogen Formation. *Acs Catal* **2016,** *6*, 2559-2576.

7. Wang, M.; Chen, L.; Sun, L. C., Recent Progress in Electrochemical Hydrogen Production with Earth-Abundant Metal Complexes as Catalysts. *Energ Environ Sci* **2012,** *5*, 6763-6778.

8. Li, Y. L.; Rauchfuss, T. B., Synthesis of Diiron(I) Dithiolato Carbonyl Complexes. *Chem Rev* **2016,** *116*, 7043-7077.

9. Schilter, D.; Rauchfuss, T. B., And the Winner is ... Azadithiolate: An Amine Proton Relay in the [FeFe] Hydrogenases. *Angew Chem Int Edit* **2013,** *52*, 13518-13520.

10. Solomon, E. I.; Szilagyi, R. K.; George, S. D.; Basumallick, L., Electronic structures of metal sites in proteins and models: Contributions to function in blue copper proteins. *Chem Rev* **2004,** *104*, 419-458.

11. Pandey, A. S.; Harris, T. V.; Giles, L. J.; Peters, J. W.; Szilagyi, R. K., Dithiomethylether as a ligand in the hydrogenase H-cluster. *J Am Chem Soc* **2008,** *130*, 4533-4540.

12. Fourmond, V.; Greco, C.; Sybirna, K.; Baffert, C.; Wang, P. H.; Ezanno, P.; Montefiori, M.; Bruschi, M.; Meynial-Salles, I.; Soucaille, P.; Blumberger, J.; Bottin, H.; De Gioia, L.; Leger, C., The Oxidative Inactivation of FeFe Hydrogenase Reveals the Flexibility of the H-cluster. *Nat Chem* **2014,** *6*, 336-342.

13. Lyon, E. J.; Georgakaki, I. P.; Reibenspies, J. H.; Darensbourg, M. Y., Coordination Sphere Flexibility of Active-Site Models for Fe-only Hydrogenase: Studies in Intra- and Intermolecular Diatomic Ligand Exchange. *J Am Chem Soc* **2001,** *123*, 3268-3278.

14. Li, B.; Liu, T. B.; Singleton, M. L.; Darensbourg, M. Y., Influence of Sulf-Oxygenation on CO/L Substitution and $Fe(CO)_3$ Rotation in Thiolate-Bridged Diiron Complexes. *Inorg Chem* **2009,** *48*, 8393-8403.

15. Lunsford, A. M.; Blank, J. H.; Moncho, S.; Haas, S. C.; Muhammad, S.; Brothers, E. N.; Darensbourg, M. Y.; Bengali, A. A., Catalysis and Mechanism of H_2 Release from Amine-Boranes by Diiron Complexes. *Inorg Chem* **2016,** *55*, 964-973.

16. Crouthers, D. J.; Denny, J. A.; Bethel, R. D.; Munoz, D. G.; Darensbourg, M. Y., Conformational Mobility and Pendent Base Effects on Electrochemistry of Synthetic Analogues of the [FeFe]-Hydrogenase Active Site. *Organometallics* **2014,** *33*, 4747-4755.

17. Yu, T. J.; Zeng, Y.; Chen, J. P.; Li, Y. Y.; Yang, G. Q.; Li, Y., Exceptional Dendrimer-Based Mimics of Diiron Hydrogenase for the Photochemical Production of Hydrogen. *Angew Chem Int Edit* **2013,** *52*, 5631-5635.

18. Li, X. Q.; Wang, M.; Zheng, D. H.; Han, K.; Dong, J. F.; Sun, L. C., Photocatalytic H_2 Production in Aqueous Solution with Host-Guest Inclusions Formed by Insertion of an FeFe-hydrogenase Mimic and an Organic Dye into Cyclodextrins. *Energ Environ Sci* **2012,** *5*, 8220-8224.

19. Tooley, C. A.; Pazicni, S.; Berda, E. B., Toward a tunable synthetic [FeFe] hydrogenase mimic: single-chain nanoparticles functionalized with a single diiron cluster. *Polym Chem-Uk* **2015,** *6*, 7646-7651.

20. Johnson, M.; Thuman, J.; Letterman, R. G.; Stromberg, C. J.; Webster, C. E.; Heilweil, E. J., Time-Resolved Infrared Studies of a Trimethylphosphine Model Derivative of [FeFe]-Hydrogenase. *J Phys Chem B* **2013,** *117*, 15792-15803.

21. Bingaman, J. L.; Kohnhorst, C. L.; Van Meter, G. A.; McElroy, B. A.; Rakowski, E. A.; Caplins, B. W.; Gutowski, T. A.; Stromberg, C. J.; Webster, C. E.; Heilweil, E. J., Time-Resolved Vibrational Spectroscopy of [FeFe]-Hydrogenase Model Compounds. *J Phys Chem A* **2012,** *116*, 7261-7271.

22. Hunt, N. T.; Wright, J. A.; Pickett, C., Detection of Transient Intermediates Generated from Subsite Analogues of [FeFe] Hydrogenases. *Inorg Chem* **2016,** *55*, 399-410.

23. Kania, R.; Frederix, P. W. J. M.; Wright, J. A.; Ulijn, R. V.; Pickett, C. J.; Hunt, N. T., Solution-Phase Photochemistry of a [FeFe]hydrogenase Model Compound: Evidence of Photoinduced Isomerisation. *J Chem Phys* **2012,** *136,* 044521.

24. Caplins, B. W.; Lomont, J. P.; Nguyen, S. C.; Harris, C. B., Vibrational Cooling Dynamics of a [FeFe]-Hydrogenase Mimic Probed by Time-Resolved Infrared Spectroscopy. *J Phys Chem A* **2014,** *118*, 11529-11540.

25. Wang, W. G.; Rauchfuss, T. B.; Bertini, L.; Zampella, G., Unsensitized Photochemical Hydrogen Production Catalyzed by Diiron Hydrides. *J Am Chem Soc* **2012,** *134*, 4525-4528.

26. Bonner, G. M.; Ridley, A. R.; Ibrahim, S. K.; Pickett, C. J.; Hunt, N. T., Probing the Effect of the Solution Environment on the Vibrational Dynamics of an Enzyme Model System with Ultrafast 2D-IR Spectroscopy. *Faraday Discuss* **2010,** *145*, 429-442.

27. Kaziannis, S.; Wright, J. A.; Candelaresi, M.; Kania, R.; Greetham, G. M.; Parker, A. W.; Pickett, C. J.; Hunt, N. T., The Role of CN and CO Ligands in the Vibrational Relaxation Dynamics of Model Compounds of the [FeFe]-hydrogenase Enzyme. *Phys Chem Chem Phys* **2011,** *13*, 10295-10305.

28. Samuel, A. P. S.; Co, D. T.; Stern, C. L.; Wasielewski, M. R., Ultrafast Photodriven Intramolecular Electron Transfer from a Zinc Porphyrin to a Readily Reduced Diiron Hydrogenase Model Complex. *J Am Chem Soc* **2010,** *132*, 8813-8815.

29. Frederix, P. W. J. M.; Adamczyk, K.; Wright, J. A.; Tuttle, T.; Ulijn, R. V.; Pickett, C. J.; Hunt, N. T., Investigation of the Ultrafast Dynamics Occurring during Unsensitized Photocatalytic H_2 Evolution by an [FeFe]-Hydrogenase Subsite Analogue. *Organometallics* **2014,** *33*, 5888-5896.

30. Barton, B. E.; Zampella, G.; Justice, A. K.; De Gioia, L.; Rauchfuss, T. B.; Wilson, S. R., Isomerization of the Hydride Complexes $[HFe_2(SR)_2(PR_3)_x(CO)_{6-x}]^+$ (x=2, 3, 4) Relevant to the Active Site Models for the [FeFe]-hydrogenases. *Dalton T* **2010,** *39*, 3011-3019.

31. Bethel, R. D.; Crouthers, D. J.; Hsieh, C. H.; Denny, J. A.; Hall, M. B.; Darensbourg, M. Y., Regioselectivity in Ligand Substitution Reactions on Diiron Complexes Governed by Nucleophilic and Electrophilic Ligand Properties. *Inorg Chem* **2015,** *54*, 3523-3535.

32. Frisch, M. J.; Trucks, G. W.; Schlegel, H. B.; Scuseria, G. E.; Robb, M. A.; Cheeseman, J. R.; Scalmani, G.; Barone, V.; Mennucci, B.; Petersson, G. A.; Nakatsuji, H.; Caricato, M.; Li, X.; Hratchian, H. P.; Izmaylov, A. F.; Bloino, J.; Zheng, G.; Sonnenberg, J. L.; Hada, M.; Ehara, M.; Toyota, K.; Fukuda, R.; Hasegawa, J.; Ishida, M.; Nakajima, T.; Honda, Y.; Kitao, O.; Nakai, H.; Vreven, T.; Montgomery Jr., J. A.; Peralta, J. E.; Ogliaro, F.; Bearpark, M. J.; Heyd, J.; Brothers, E. N.; Kudin, K. N.; Staroverov, V. N.; Kobayashi, R.; Normand, J.; Raghavachari, K.; Rendell, A. P.; Burant, J. C.; Iyengar, S. S.; Tomasi, J.; Cossi, M.; Rega, N.; Millam, N. J.; Klene, M.; Knox, J. E.; Cross, J. B.; Bakken, V.; Adamo, C.; Jaramillo, J.; Gomperts, R.; Stratmann, R. E.; Yazyev, O.; Austin, A. J.; Cammi, R.; Pomelli, C.; Ochterski, J. W.; Martin, R. L.; Morokuma, K.; Zakrzewski, V. G.; Voth, G. A.; Salvador, P.; Dannenberg, J. J.; Dapprich, S.; Daniels, A. D.; Farkas, Ö.; Foresman, J. B.; Ortiz, J. V.; Cioslowski, J.; Fox, D. J. *Gaussian 09*, Gaussian, Inc.: Wallingford, CT, USA, 2009.

33. Khalil, M.; Demirdoven, N.; Tokmakoff, A., Coherent 2D IR Spectroscopy: Molecular Structure and Dynamics in Solution. *J Phys Chem A* **2003,** *107*, 5258-5279.

34. Hamm, P.; Zanni, M. T., *Concepts and Methods of 2D Infrared Spectroscopy*. Cambridge University Pres: Cambridge ; New York, 2011.

35. King, J. T.; Baiz, C. R.; Kubarych, K. J., Solvent-Dependent Spectral Diffusion in a Hydrogen Bonded "Vibrational Aggregate". *J Phys Chem A* **2010,** *114*, 10590-10604.

36. Osborne, D. G.; King, J. T.; Dunbar, J. A.; White, A. M.; Kubarych, K. J., Ultrafast 2DIR probe of a host-guest inclusion complex: Structural and dynamical constraints of nanoconfinement. *J Chem Phys* **2013,** *138,* 144501.

37. Kiefer, L. M.; Kubarych, K. J., Solvent-Dependent Dynamics of a Series of Rhenium Photoactivated Catalysts Measured with Ultrafast 2DIR. *J Phys Chem A* **2015,** *119*, 959-965.

38. Lamotte, M.; Joussot-Dubien, J., New Evidence for Oriented Interaction Between Normal Alkanes and Aromatic Molecules from Spectral Solvent Shifts. *Chem Phys* **1973,** *2*, 245-248.

39. Nilsen, I. A.; Osborne, D. G.; White, A. M.; Anna, J. M.; Kubarych, K. J., Monitoring Equilibrium Reaction Dynamics of a Nearly Barrierless Molecular Rotor using Ultrafast Vibrational Echoes. *J Chem Phys* **2014,** *141,* 134313.

40. Georgakaki, I. P.; Thomson, L. M.; Lyon, E. J.; Hall, M. B.; Darensbourg, M. Y., Fundamental Properties of Small Molecule Models of Fe-only Hydrogenase: Computations Relative to the Definition of an Entatic State in the Active Site. *Coordin Chem Rev* **2003,** *238*, 255-266.

41. Badger, R. M., A Relation Between Internuclear Distances and Bond Force Constants. *J Chem Phys* **1934,** *2,* 128.

42. Hartwig, J. F., *Organotransition metal chemistry : from bonding to catalysis*. University Science Books: Sausalito, Calif., 2010.

43. Housecroft, C. E.; Sharpe, A. G., *Inorganic chemistry*. 2nd ed.; Pearson Prentice Hall: Upper Saddle River, N.J., 2005.

44. Aime, S.; Dastru, W.; Gobetto, R.; Krause, J.; Milone, L., Evaluation of the Energy Barrier for Carbonyl Exchange in the Highly Fluxional $Ru_3(Co)_{12}$ System. *Organometallics* **1995,** *14*, 4435-4438.

45. Aime, S.; Gambino, O.; Milone, L.; Sappa, E.; Rosenberg, E., Stereochemically Nonrigid Carbonyl-Complexes of Group-8 B-Metal Clusters. *Inorg Chim Acta* **1975,** *15*, 53-56.

46. Nishida, J.; Tamimi, A.; Fei, H. H.; Pullen, S.; Ott, S.; Cohen, S. M.; Fayer, M. D., Structural Dynamics Inside a Functionalized Metal-Organic Framework Probed by Ultrafast 2D IR Spectroscopy. *P Natl Acad Sci USA* **2014,** *111*, 18442-18447.

47. King, J. T.; Anna, J. M.; Kubarych, K. J., Solvent-hindered Intramolecular Vibrational Redistribution. *Phys Chem Chem Phys* **2011,** *13*, 5579-5583.

48. Banno, M.; Sato, S.; Iwata, K.; Hamaguchi, H., Solvent-dependent intra- and intermolecular vibrational energy transfer of $W(CO)_6$ probed with sub-picosecond time-resolved infrared spectroscopy. *Chem Phys Lett* **2005,** *412*, 464-469.

Chapter 4

Dendritic Modulation of Vibrational Dynamics in a Biomimetic Photocatalyst Studied with 2D-IR

4.1 Introduction

One of the primary methods of biomimetic chemistry is to incorporate the steric bulk and nanoconfinement evident in enzymes into small-molecule catalysts.[1-2] Enzymes are macromolecular scaffolds built around small active sites, and the enzyme scaffold is known to significantly contribute to the reactivity of the active site by isolating it from bulk solvent, lowering the reorganizational energy of the active site, modulating the dielectric medium of the active site, and actively participating in the catalytic process.[3-4] Biomimetic attempts to incorporate nanoconfinement into catalyst design have generally followed one of two routes – confinement in some form of molecular cage, or incorporation into a macromolecular assembly.

Molecular cages have been extensively studied and tailor-made for a variety of applications. Molecular cages are classified according to the freedom of the guest molecule to leave the host. Carcerands are molecular complexes in which the guest molecule is covalently trapped,[5] and hemicarcerands are molecular complexes which permit the entry and exit of guest molecules while favoring encapsulation at room temperature. Cyclodextrins are excellent examples of biomolecular hemicarcerands, and cyclodextrins are well known to provide solubility in aqueous media to otherwise-insoluble compounds and to modulate the reactivity of encapsulated compounds.[6-7] Other artificial hemicarcerands include molecular capsules and calixarene- and resorcinarene-based cavitands.[8-14] Molecular nano-encapsulation is well known to produce biomimetic chemistry that would be otherwise impossible in aqueous media.[15-17]

Molecular incorporation into a polymeric or dendritic assembly is another widely used biomimetic strategy. Dendritic assemblies are well known to modulate and sometimes enhance the reactivity of organometallic compounds, and a variety of biomimetic modulations of chemical reactivity have been reported in dendritic assemblies.[18] These biomimetic modulations are attributed to several factors, among them the hydrophobic effect, increased stability of photocatalysts, and restricted solvent accessibility of the active site.[19] Small-molecule mimics of the hydrogenase enzyme active site are excellent examples of molecular systems which demonstrably benefit from the effects of nano-encapsulation.

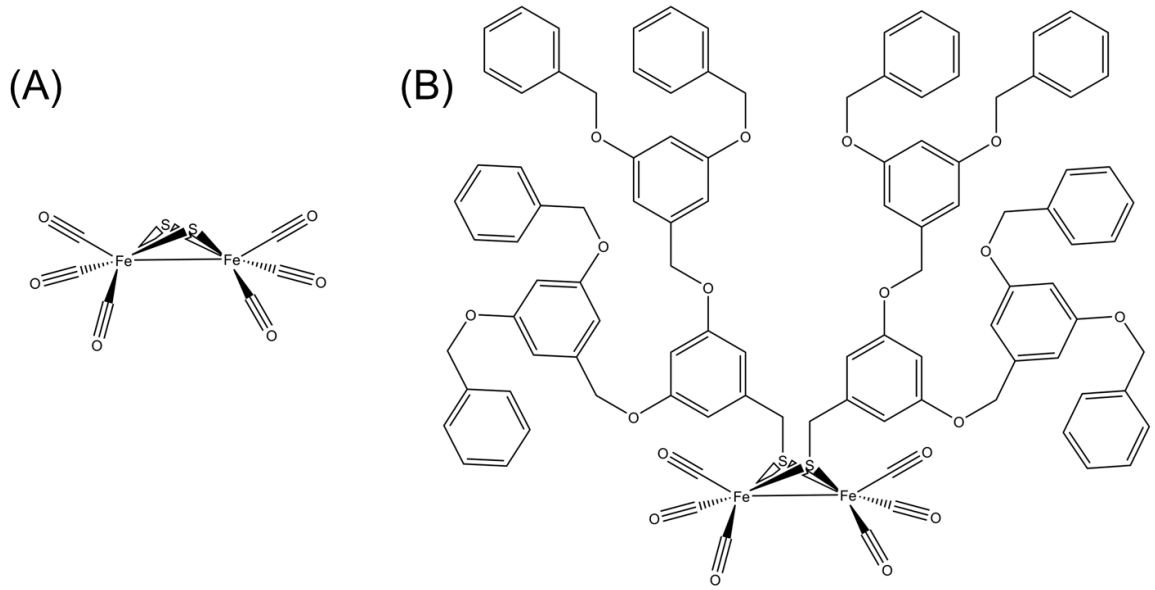

Figure 4.1: (A) $[Fe(\mu\text{-}S)(CO)_3]_2$, which we use as a reference small-molecule. (B) $[Fe(dendron)(CO)_3]_2$, where the dendrons are second-generation Frechet-type poly(aryl ether) dendrimers

Li et. al. reported that encapsulation in a cyclodextrin increased the yield of a diiron hexacarbonyl photocatalyst,[20] and encapsulation in a protein hydrogel significantly improves the reactivity and longevity of diiron hexacarbonyl compounds.[21-22] Covalent addition of a diiron hexacarbonyl catalyst to a poly(acrylic acid) polymer has been shown to catalyze significant hydrogen production in aqueous media,[23] and addition of a chitosan polymer to a reaction mixture catalyzed by a diiron hexacarbonyl compound dramatically increased the reaction yield and the lifetime of the catalyst.[24] In another study a diiron hexacarbonyl group was incorporated into a poly(aryl-ether) dendritic assembly and proved to be an excellent photocatalyst for the production of H_2.[25] The group found that

the reaction yield increased with increased dendrimer generation and suggested that the improved yield was directly due to modulation of the nano-environment by the poly(aryl-ether) dendrimers. We report here an investigation of the same system using the second-generation poly(aryl ether) dendrimer and $[Fe(\mu\text{-}S)(CO)_3]_2$ as a reference. Both are shown in Figure 4.1. In the remainder of this work we refer to the reference small molecule by its formula $[Fe(\mu\text{-}S)(CO)_3]_2$ and to the dendritic complex simply as the dendrimer. We find clear spectral signatures of nano-environmental modulation in the carbonyl vibrational modes as well as a pronounced and solvent-dependent modulation of the initial phase of the IVR process.

The conformation of poly(aryl-ether) dendrimers is known to be highly solvent-dependent, and solvents in dendrimer studies are often ranked by the solubility of the dendritic groups in that solvent. A solvent in which the dendritic groups are well solvated is classified as a good solvent for that dendritic system, and one in which the dendritic groups are only sparingly soluble is classified as a poor solvent for the same dendritic system.[26-28] The conformation of a dendritic molecule is highly dependent upon its solvent – in good solvents, the dendritic groups are well solvated, resulting in a significant increase of the complex's hydrodynamical radius with each dendrimer generation.[27] In poorer solvents the dendritic groups tend to contract around the molecular core, resulting in only a slight increase of the hydrodynamical radius with each dendrimer generation.[27] In some ways the solvent-dependence of a dendrimer's conformation is similar to biomolecules whose conformational state depends upon the solution's pH, cosolvents, and other factors, and the strong solvent-dependence of the dendrimer's conformation offers a unique experimental variable with which to control the experimental state of the dendritic system. By exploiting this conformational solvent dependence we investigate a single molecular system over a range of conformations, and by directly comparing the dynamics of a diiron hexacarbonyl group encapsulated in a dendritic assembly and the same diiron hexacarbonyl group as a small-molecule we are able to directly determine the dynamical phenomena associated with the effects of nano-confinement. Our results indicate that inclusion into a dendritic system significantly affects the interaction of the carbonyl groups

with the immediate solvation shell and reveals solvent-dependent changes in the spectral diffusion and vibrational lifetimes of the carbonyl modes.

4.2 Experimental Details

Materials: The dendritic groups were ordered from Angene Limited and used as received. The THF used to synthesize the dendrimer was distilled and stored over molecular sieves. All other solvents and reagents were ordered from Sigma Aldrich and used as received. All reactions and manipulations were performed using standard Schlenk line procedures.

Synthesis of $[Fe(\mu\text{-}S)(CO)_3]_2$: The synthetic method described by Stanley et. al.[29] was employed. Briefly, 12 mL of $Fe(CO)_5$ was added to 60 mL of methanol and 35 mL of concentrated KOH. The solution was stirred and cooled in an ice bath before 16 g of elemental sulfur were added slowly over the course of ~ 10 minutes. The solution was stirred for an hour and 140 mL of distilled H_2O, 42 g of NH_4Cl and 350 mL of hexanes were added. The reaction mixture was removed from the ice bath and left to stir for overnight. The hexanes layer was separated from the reaction mixture and the reaction mixture was extracted with hexanes until the hexane layers remained uncolored. The extractions were added to the hexanes initially removed from the reaction mixture, and the combined fractions were rotovapped away leaving the reddish-brown crude product. The crude product was purified on a silica gel column with hexanes as the eluent. Product purity was checked by ensuring that the only carbonyl vibrational frequencies in the product matched those reported in the literature.

Synthesis of dendrimer: The product was synthesized and purified according the procedure.[25]

Synthesis of $[Fe(\mu\text{-ethanethiol})(CO)_3]_2$: One gram of $Fe_2(CO)_9$ and 0.8 mL of ethanethiol were dissolved in benzene and the solution was stirred at room temperature for 12 hours. The solvent was rotovapped away to leave a reddish-brown crude product, which was purified on a silica gel column using hexanes as the mobile phase and recrystallized from petroleum ether. Product purity was verified by comparing the product carbonyl bands with those reported in the literature.

Experimental Set-up: The experimental set-up described in Chapter 1.4 was used without any modification for these experiments.

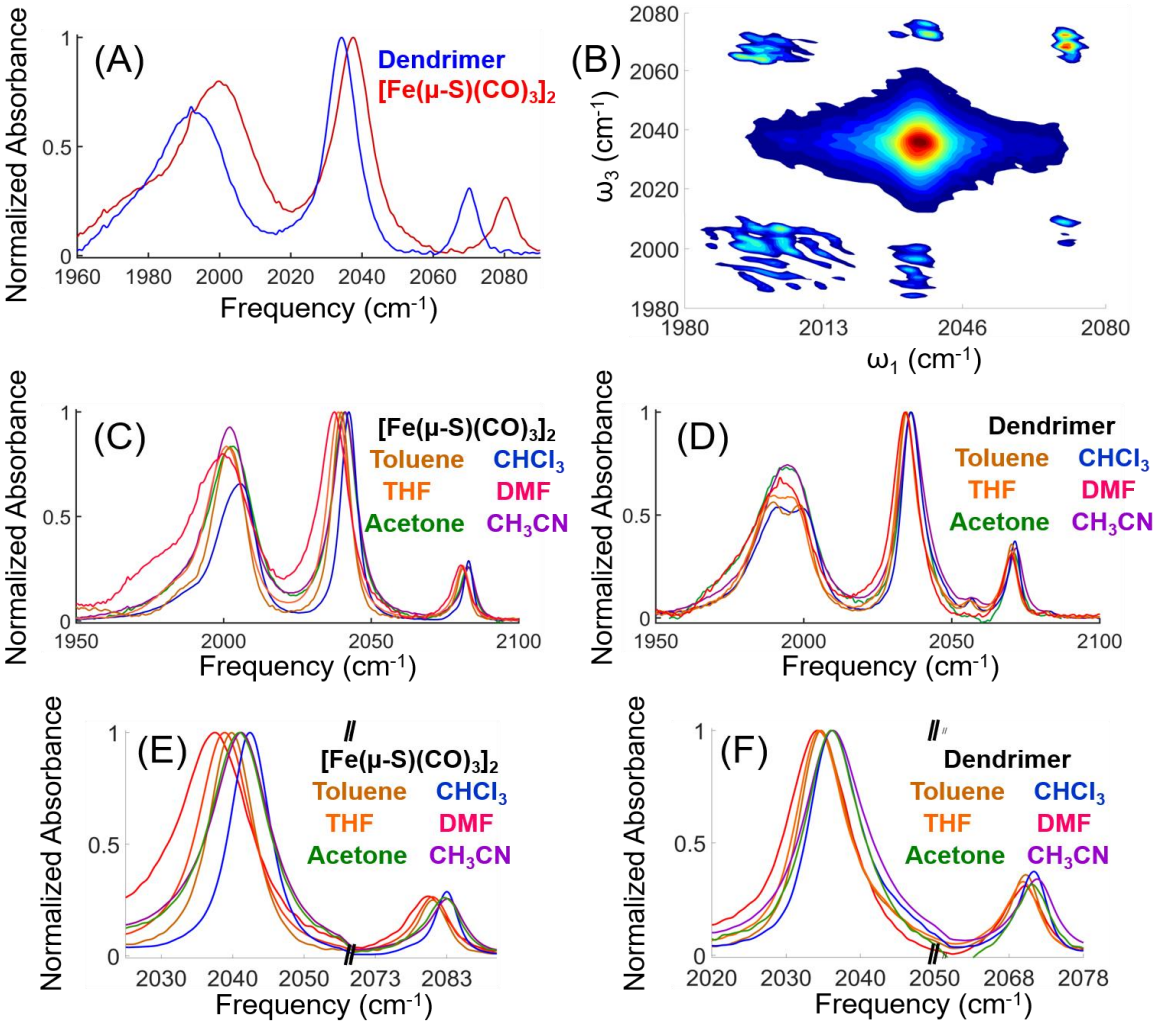

Figure 4.2: (A) Representative carbonyl vibrational spectra of $[Fe(\mu\text{-}S)(CO)_3]_2$ and the dendrimer in DMF. The vibrational frequencies of the dendrimer are uniformly red shifted from the frequencies of $[Fe(\mu\text{-}S)(CO)_3]_2$. (B) 2D-IR spectrum of the dendrimer in DMF, centered on mode 2. (C) Carbonyl vibrational spectra of $[Fe(\mu\text{-}S)(CO)_3]_2$ in all of the solvents used in this study. (D) Carbonyl vibrational spectra of the dendrimer in all of the solvents used in this study. (E) Carbonyl vibrational spectra of $[Fe(\mu\text{-}S)(CO)_3]_2$ in all of the tested solvents, focused on modes 1-2. Note that acetone, $CHCl_3$, and CH_3CN show almost identical vibrational frequencies for mode 1, which are blue shifted from the almost identical vibrational frequencies of mode 1 in toluene, THF, and DMF. (F) Carbonyl vibrational spectra of $[Fe(\mu\text{-}S)(CO)_3]_2$ in all of the tested solvents, focused on modes 1-2. Note that acetone, $CHCl_3$, and CH_3CN show almost identical vibrational frequencies for mode 1, which are blue shifted from the almost identical vibrational frequencies of mode 1 in toluene, THF, and DMF.

4.3 Results

The carbonyl vibrations of $[Fe(\mu\text{-}S)(CO)_3]_2$ and the dendrimer are shown in Figure 4.2. The addition of the dendritic group to the disulfides causes a slight red shift in the carbonyl vibrational frequencies, but the band pattern is unaffected by the organic bridging groups. The polar solvent causes modes 3-5 to broaden and overlap significantly in both the dendrimer and $[Fe(\mu\text{-}S)(CO)_3]_2$ and we focus our analysis on mode 2, as in Chapter 3.

An interesting pattern is observed in the FTIR data shown in Figure 4.2. The vibrational frequencies of mode 1 show a distinct solvent dependence in $[Fe(\mu\text{-}S)(CO)_3]_2$,

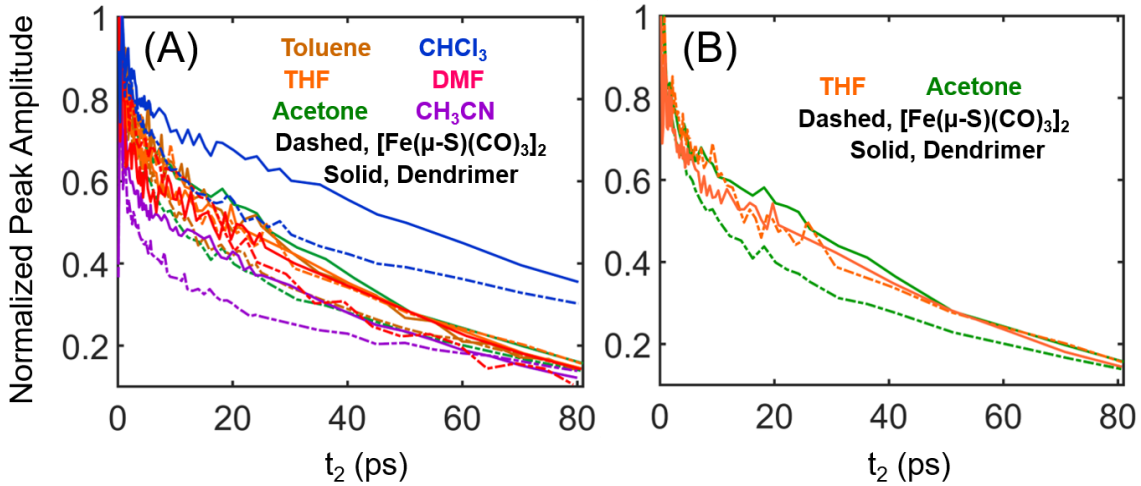

Figure 4.3: (A) Decay of mode 2's nonrephasing peak amplitude for all solvents tested and for both the dendrimer and $[Fe(\mu\text{-}S)(CO)_3]_2$. Note that the decay in peak amplitude for both compounds in all solvents except $CHCl_3$ are essentially indistinguishable after 60 ps, and in $CHCl_3$ the vibrational relaxation of both compounds appears to become similar as t_2 approaches 80 ps. (B) Decay of mode 2's nonrephasing peak amplitude in THF and acetone, representing solvents in which the early-time vibrational relaxation differs and does not differ, respectively, between the dendrimer and $[Fe(\mu\text{-}S)(CO)_3]_2$.

where the frequencies of DMF, THF, and toluene are almost identical and red shifted by ~ 2 cm^{-1} from the frequencies of acetone, acetonitrile, and chloroform. The same pattern is evident in the spectrum of the dendrimer, but in the dendrimer mode 2 displays this difference in center frequencies, and it is much less pronounced in mode 1.

Figure 4.3a shows the decay of the peak amplitude of mode 2 in the nonrephasing data for both the dendrimer and the $[Fe(\mu\text{-}S)(CO)_3]_2$. The color of the data series represents the solvent in which the data was collected, and the dendrimer is represented by a solid line while $[Fe(\mu\text{-}S)(CO)_3]_2$ is represented by a dashed line. Figure 4.3a illustrates that while there is noticeable solvent- and bridging-group-dependent variation in the peak

relaxation at early waiting times, the slower timescale for vibrational relaxation is indistinguishable between solvents and between the dendrimer and $[Fe(\mu\text{-}S)(CO)_3]_2$. The only significant outlier is the solvent chloroform, and in chloroform only the fast component of the vibrational relaxation appears to differ between the dendrimer and $[Fe(\mu\text{-}S)(CO)_3]_2$.

Figure 4.4 show the decay of the inhomogeneity indices of mode 2 in DMF, acetone, and acetonitrile. We select these three solvents to illustrate the three trends

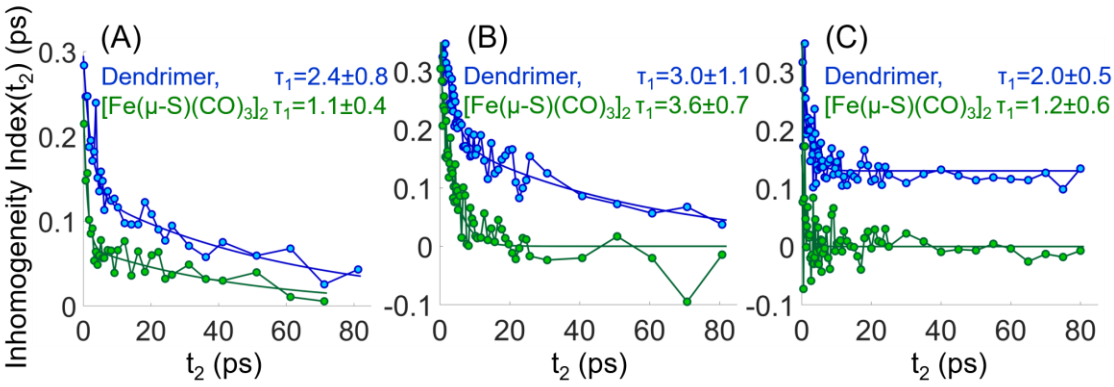

Figure 4.4: (A) Spectral diffusion of mode 2 in acetone. Note that both compounds display a decay which is best fit by a biexponential decay. (B) Spectral diffusion of mode 2 in DMF. Note that only the dendrimer is best fit with a single exponential decay. (C) Spectral diffusion of mode 2 in CH_3CN. Note that neither data series are best fit by a biexponential decay on our experimental timescale.

observed in the inhomogeneity indices of all of the solvents tested in this study. In DMF (Figure 4.4a) the inhomogeneity index of $[Fe(\mu\text{-}S)(CO)_3]_2$ is well fit by a single exponential decay with a time constant of ~ 3 ps, while in the dendrimer the inhomogeneity index is best fit to a biexponential decay. The faster of the two timescales in the decay of the inhomogeneity index of the dendrimer is indistinguishable from the single timescale of the inhomogeneity index of $[Fe(\mu\text{-}S)(CO)_3]_2$. In acetone (Figure 4.4b) the inhomogeneity indices of both the dendrimer and $[Fe(\mu\text{-}S)(CO)_3]_2$ are well fit by biexponential decay models, in which the fast timescale of $[Fe(\mu\text{-}S)(CO)_3]_2$ is significantly faster than the fast timescale in the dendrimer. Finally, in acetonitrile, both the dendrimer and $[Fe(\mu\text{-}S)(CO)_3]_2$ show inhomogeneity indices that are well fit by a single exponential decay, and the dendrimer's inhomogeneity index decaying to a static offset. The pattern of inhomogeneity indices in toluene is similar to that of DMF, while THF and chloroform match the pattern displayed by acetone where both compounds exhibit biexponential decays. Acetonitrile is

the only solvent in which both compounds show only a single decay on our experimental timescale.

4.4 Discussion

The carbonyl vibrational spectra of $[Fe(\mu\text{-}S)(CO)_3]_2$ and the dendrimer shown in Figure 4.2 are very similar in band patter but are noticeably different in frequency, with the carbonyl frequencies of the dendrimer being red shifted from the frequencies of $[Fe(\mu\text{-}S)(CO)_3]_2$. The frequencies of the dendrimer are very similar to the frequencies of $(\mu\text{-}pdt)[Fe(CO)_3]_2$ and $(\mu\text{-}edt)[Fe(CO)_3]_2$ as reported in Chapter 3, and we attribute this red shift in vibrational frequencies to increased electron density of the diiron core of the molecule arising from the organic groups bonded to the bridging sulfides. As detailed in Chapter 1.4 carbon monoxide bonds to transition metals partially through accepting electron density from the metal into the π^*-antibonding molecular orbital. An increase in the electron density of the transition metal is thus reflected by a weakening of the C≡O bond and a red shift of the C≡O vibrational frequency.[30]

We note the presence of a small peak at ~ 2060 cm^{-1} in several of the solvents, specifically toluene, chloroform, and THF. There is no predicted vibrational frequency for the dendrimer that corresponds to this peak, and there are several possible origins for it. One of these is that the small band at ~ 2060 cm^{-1} is an impurity from the synthetic process which was not completely removed by the purification. If this were the case, it would be expected to appear in all of the tested solvents, and it is noticeably absent from several, including DMF and CH_3CN.

Another possibility is that this band arises from a different isomeric form of the dendrimer. The poly(aryl-ether) dendrimer used in this study exists in two conformations, the so-called "equatorial-equatorial" and the "axial-equatorial" isomers, which describe the relative orientation of the two dendritic arms and are depicted in Figure 4.5. Roughly 85% of the dendritic sample exists in the axial-equatorial conformation.[25] To test whether the two isomeric forms might have different vibrational frequencies we synthesized $[Fe(\mu\text{-}ethanethiol)(CO)_3]_2$, which is also known to exist in axial-equatorial and equatorial-equatorial isomeric forms. Figure 4.5b shows the infrared spectrum of in $[Fe(\mu\text{-}$

ethanethiol)$(CO)_3]_2$ hexane. The frequency of mode 2 does not appear to be tangibly affected by the isomeric form of the ethanethiol groups, but modes 1 and 3-5 do show

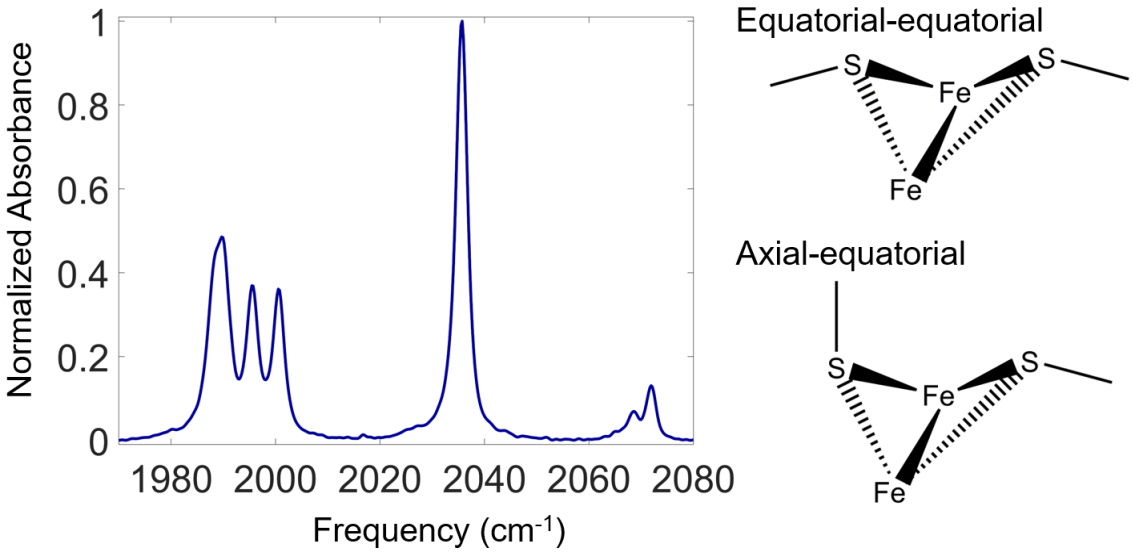

Figure 4.5: FTIR spectrum of [Fe(μ-ethanethiol)$(CO)_3]_2$ in hexanes. The double peak near 2070 cm^{-1} is due to a frequency difference of mode 1 in the two isomers, as are the four modes between 1980-2000 cm^{-1}. The axial-equatorial and equatorial-equatorial conformations are depicted to the right.

isomeric frequency differences of several wavenumbers. We find this test to be insightful but inconclusive. It does demonstrate that an isomeric frequency difference might account for additional peaks in the dendrimer's vibrational spectrum, but the frequency difference of ~ 15 cm^{-1} between mode 1 and the unidentified peak in the dendrimer's spectrum is much larger than the isomeric difference observed in the spectrum of [Fe(μ-ethanethiol)$(CO)_3]_2$. If the data gathered from [Fe(μ-ethanethiol)$(CO)_3]_2$ may be extrapolated to the dendrimer, the center frequency of mode 2 is expected to only slightly affected by any isomeric effects, and the broadening of modes 3-5 due to solvent polarity obscures the presence of any isomerically-induced changes in the frequencies of modes 3-5. Since in this analysis we focus solely upon mode 2, we find the exact origin of the unidentified peak at ~ 2060 cm^{-1} worthy of further investigation, but not crucial to the current discussion.

The most enigmatic aspect of our FTIR data is the apparent presence of what seem to be two distinct solvent-dependent frequencies for mode 1 in [Fe(μ-S)$(CO)_3]_2$ and for mode 2 in the dendrimer, and that in both cases the same solvents cause a red shift or a

blue shift of the relevant vibrational frequency. The solvents associated with a higher frequency for the vibration are CH_3CN, acetone, and chloroform, while the solvents associated with a lower vibrational frequency are DMF, toluene, and THF. This solvent-dependence of vibrational frequency does not depend upon the dendrimer, as it is present in $[Fe(\mu\text{-}S)(CO)_3]_2$, but in the dendrimer the mode most strongly affected is mode 2, and not mode 1. The two groups of solvents defined by our spectra are not similar in polarity, donicity, dielectric constant, or viscosity. For example, DMF, a polar, strongly interacting, and protic solvent consistently shifts the vibrational frequency of mode 1 in $[Fe(\mu\text{-}S)(CO)_3]_2$ and of mode 2 in the dendrimer in a manner more similar to toluene, a nonpolar, weakly interacting, aprotic solvent, than to acetone. We do note that CH_3CN, acetone, and chloroform are uniformly smaller than DMF, toluene, and THF, although whether the molecular size of the solvent is in any way significant to the consistent red shifting of the relevant frequency is unclear to us.

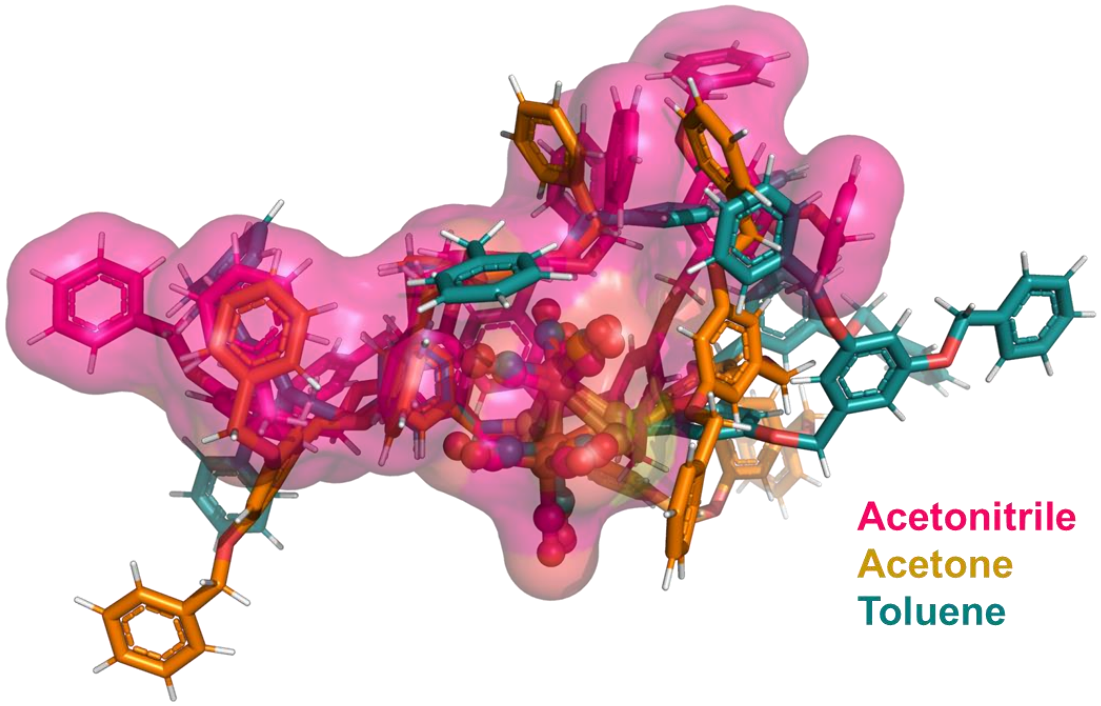

Figure 4.6: Molecular conformations for the dendrimer in acetonitrile, acetone, and toluene. Acetone and toluene show very similar conformations, but even at the low generation number of the dendrimer the conformation in acetonitrile is much more compact than in acetone or toluene. This is in good agreement with the previously published work on the conformation of poly(aryl ether) dendrimers in good and poor solvents.

As discussed in the Chapter 4.1, solvents in dendrimer studies are often classified by their capacity to solvate the dendritic groups of the molecule. Solvents in which the dendrimer is well solvated are considered to be "good" solvents, and in good solvents the dendritic portions of the complex are often extended some distance away from the center of the complex.[26-27] In contrast to the dendritic conformation in good solvents, solvents in which the dendritic groups are only sparingly soluble are considered "poor" solvents, and in poor solvents the hydrodynamical radius of the complex is typically smaller than the radius of the same complex in a good solvent due to a contraction of dendritic groups around the core of the complex. Of the solvents used in this study toluene, DMF, and THF are known to be good solvents for poly(aryl-ether) dendrimers, while acetone is known to be a "medium" quality solvent and acetonitrile a poor solvent.[26-27] To the best of our knowledge the solvent quality of chloroform for poly(aryl-ether) dendrimers has never been determined. However, in a molecular dynamics study of a poly(aryl ether) dendrimer with an $[FeS]_2$ core the dendritic groups were found to extend consistently in the explicit chloroform solvent, indicating that chloroform is a reasonably good solvent for poly(aryl ether) dendrons.[31]

The decay of the inhomogeneity in mode 2 of the dendrimer is significantly different from the inhomogeneity decay of mode 2 in $[Fe(\mu\text{-}S)(CO)_3]_2$. The most apparent difference is that the dendrimer invariably displays two pronounced timescales for the decay of the inhomogeneity index, while in $[Fe(\mu\text{-}S)(CO)_3]_2$ the inhomogeneity index is often well fit by a single exponential decay, and when an additional slow timescale is present its contribution to the total inhomogeneity is typically minimal in comparison to the contribution of the fast timescale. In solvents like DMF and chloroform the slow component of the dendrimer's inhomogeneity index decays significantly on the experimental timescale, while in other solvents like toluene the decay of the slow component of the spectral inhomogeneity is exceedingly slow. The slow decay of the spectral inhomogeneity is especially pronounced in acetonitrile, where the decay of the slow phase of the spectral inhomogeneity is so slow that it appears static on our experimental timescale. Our experimental set-up limits our t_2 measurements to ~ 90 ps, and for this reason it is not possible to reliably fit the slow phase of the dendrimer's

inhomogeneity decay. The fast phase of the inhomogeneity decay, however, may be extracted from the data. The fast timescales extracted from fitting the decay of mode 2 in the dendrimer and in $[Fe(\mu\text{-}S)(CO)_3]_2$ are listed in Table 4.1. We caution that exact fit parameters from our biexponential models are less certain than from those from our single exponential models due to contribution of the additional timescale. The extracted timescale for the fast phase of mode 2's spectral diffusion in the dendrimer is in good agreement with the data, but the confidence interval associated with that timescale is also meaningful.

As listed in Table 4.1, the timescale of the fast phase of the inhomogeneity decay of mode 2 in $[Fe(\mu\text{-}S)(CO)_3]_2$ is ~ 3 ps for all of the solvents tested except acetone and acetonitrile, where it is ~ 1 ps. For the dendrimer, the timescale of the fast decay of the spectral inhomogeneity of mode 2 is less solvent-dependent and is consistently ~ 2.5-3.5

Table 4.1: Fit values for the fast phase of the inhomogeneity decay of mode 2 in the dendrimer and $[Fe(\mu\text{-}S)(CO)_3]_2$ and the slow phase of spectral diffusion in the dendrimer, listed by solvent

Sample	Solvent					
	Acetone	CH_3CN	$CHCl_3$	Toluene	DMF	THF
$[Fe(\mu\text{-}S)(CO)_3]_2$	1.1 ± 0.4	1.2 ± 0.6	3.1 ± 0.6	3.1 ± 0.6	3.6 ± 0.7	3.0 ± 0.7
Dendrimer, τ_1	2.4 ± 0.8	2.0 ± 0.5	3.2 ± 1.3	2.7 ± 0.9	3.0 ± 1.1	2.3 ± 1.0
Dendrimer, τ_2	61 ± 20	1200 ± 4000	68 ± 28	94 ± 34	57 ± 27	93 ± 37

ps, except in acetonitrile, where it is 2 ps. There are multiple possible interpretations of this data. Acetone and acetonitrile are the poorest quality solvents tested, and the encapsulation of the diiron hexacarbonyl core by the dendritic arms is expected to be the greatest in these two solvents – the two-fold slow-down in the timescale of inhomogeneity decay observed between $[Fe(\mu\text{-}S)(CO)_3]_2$ and the dendrimer in acetonitrile and acetone may reflect a significant alteration of the carbonyl ligands' microenvironment due to nano-encapsulation by the dendritic groups.

Alternatively, the reduction in solvent-dependence of the fast phase of spectral diffusion in the dendrimer suggests a slightly different interpretation, that the poly(aryl-ether) dendritic groups exert a roughly comparable influence on the dynamics of the carbonyl ligands regardless of the solvent in which the dendrimer is solvated. This

interpretation suggests that in the case of $[Fe(\mu\text{-}S)(CO)_3]_2$ whatever solvent-dependent interactions make the fast timescale of spectral diffusion in DMF different from the fast timescale of spectral diffusion in acetone are modulated by the dendritic assembly.

These two interpretations are not mutually exclusive, and our experimental data does not appear to clearly support one over the other. The molecular similarity of acetone and acetonitrile, both of which are small molecules with defining C≡O or C≡N groups, does lend some support the hypothesis of some specific and similar set of solvation microenvironments in the case of $[Fe(\mu\text{-}S)(CO)_3]_2$. The hypothesis of similar of a similar solvation microenvironment in acetonitrile and acetone is supported by the FTIR data in which both acetonitrile and acetone caused the frequency of carbonyl vibrational modes in $[Fe(\mu\text{-}S)(CO)_3]_2$ and in the dendrimer to blue shift from the vibrational frequencies in toluene, THF, and DMF.

The exceedingly slow decay of the slow phase of spectral inhomogeneity in acetonitrile stands apart from all of the other tested solvents. Interestingly, acetonitrile is the only decidedly poor solvent for poly(aryl-ether) dendrimers tested in this study. Previous studies of poly(aryl-ether) dendrimers in acetonitrile have shown very little change in the hydrodynamical radius of the complex with increased dendrimer generation, which reflects a strong tendency of pol(aryl-ether) dendrimers to form inwardly-folding conformations in acetonitrile.[27] The correlation of solvent quality and dendritic conformation suggests that the slow phase of inhomogeneity decay observed in all of the dendritic samples is due to the dendritic modulations of solvent-carbonyl interactions. In all of the good and medium solvents the carbonyl ligands are expected to be at least partially solvent-accessible, but the dendritic groups are conformationally mobile at room temperature, and the solvation shell immediately adjacent to the dendritic groups will be in continual flux as it adjusts to the slow fluctuations of the dendritic groups. We suggest that this continuous fluctuation and reorientation of the dendrimer's immediate solvation shell is reflected in the slow decay of the dendrimer's spectral inhomogeneity which is absent in $[Fe(\mu\text{-}S)(CO)_3]_2$.

The significant slowdown of this dynamical timescale in acetonitrile indicates that the carbonyl ligands are either exposed to an environment similar to bulk acetonitrile,

where any additional slow phase of spectral decay is so slow as to be imperceptible, that the carbonyl ligands are barely exposed to the solvent, or that the solvation dynamics of the dendrimer in acetonitrile are much more affected by the dendritic groups than in any of the other tested solvents. In light of the previously-discussed proclivity of poly(aryl-ether) dendrimers to contract upon their molecular core in acetonitrile, we find that the second interpretation to be the most probable, and propose that the slow-phase of spectral diffusion in acetonitrile does indeed represent a true case of nano-confinement, in contrast to the other tested solvents, where the effect of the dendritic assembly is decidedly present but the nano-confinement of the carbonyl groups is at most partial. Similar spectral diffusion dynamics have been reported from a diiron hexacarbonyl compound covalently encapsulated in a metal-organic framework (MOF).[32] When the MOF was dry the spectral diffusion of the probe's carbonyl vibrations was fit to a biexponential decay with timescales of 7 and ~ 670 ps, while immersion of the MOF in DMF solvent slowed the spectral diffusion timescales to 23 and > 2000 ps. The dynamical slowdown was hypothesized reflect the slower dynamics of the MOF when the pores were filled with a polar, strongly interacting solvent. The nano-environmental constraint of a MOF's pores is probably much greater than that exerted by the second-generation poly(aryl ether) dendritic groups in our experiment, but the qualitative similarity of the MOFs dynamics to what we observe in our dendritic sample supports our hypothesis that our data directly reflects at least a partial nano-confinement of the diiron hexacarbonyl dendritic core.

The vibrational relaxation of mode 2, as shown in Figure 4.3, is significantly affected both by the solvent and by the presence of a dendritic assembly in early waiting times. However, by ~ 40 ps the effect of the solvent and the dendrimer becomes minimal, and the slow phase of the vibrational relaxation of the carbonyl groups is uniform with one exception, that of chloroform. However, despite the exceptionally slow vibrational relaxation of the carbonyl groups in chloroform, the peak traces of the dendrimer and of $[Fe(\mu\text{-}S)(CO)_3]_2$ appear to eventually converge in chloroform as they do in the other solvents. We suggest that the slow vibrational relaxation in chloroform is simply due to an idiosyncrasy of solvent-solute interactions within that system.

In all of the tested solvents except for DMF and THF the early vibrational relaxation of $[Fe(\mu\text{-}S)(CO)_3]_2$ is much faster than the early vibrational relaxation of the dendrimer. An example of this is provided Figure 4.3b, where acetone is used to exemplify a solvent in which such a difference is noticeably present, and THF to exemplify a solvent in which the same difference is clearly absent. Although the difference in early vibrational relaxation between the dendrimer and $[Fe(\mu\text{-}S)(CO)_3]_2$ is not present in all of the tested solvents, it does represent a majority of the sampled systems, and merits further consideration.

IVR in small molecules is often modeled using Fermi's Golden Rule, which is given in Equation 4.1:

$$\Gamma_{ij} = \frac{2\pi}{\hbar}\left|V_{ij}\right|^2 \rho_j \tag{4.1}$$

where Γ_{ij} is the probability of a transfer of vibrational energy from state i to state j, V_{ij} is the coupling of states i and j, and ρ_j is the final density of states. In systems as large as the dendrimer IVR is probably more dependent upon specific pathways of vibrational energy dissipation determined by anharmonic vibrational coupling.[33-36]

In both the dendrimer and $[Fe(\mu\text{-}S)(CO)_3]_2$ the two bridging sulfides are not constrained by a bridging group and are free to fluctuate independently of each other. In $[Fe(\mu\text{-}S)(CO)_3]_2$ these independent fluctuations are probably insignificant and unlikely to distort the square pyramidal coordination sphere of each iron atom, but in the dendrimer each bridging sulfide is directly connected to a large and otherwise un-tethered molecular group. The square pyramidal geometry of diiron hexacarbonyl core could easily be distorted by forces exerted on the sulfides by the dendritic groups. A significant distortion of the square pyramidal coordination geometry of the two iron atoms could conceivably alter the coupling of the carbonyl vibrations to lower frequency vibrations of the diiron hexacarbonyl group, and thus indirectly slow the rate of intramolecular IVR. The two solvents in which no difference is observed in the vibrational relaxation of the dendrimer and of $[Fe(\mu\text{-}S)(CO)_3]_2$ are THF and DMF, both of which are good solvents in which significant conformational distortions of the molecule are unexpected.

Previous work in alkane solvents has shown that the intracarbonyl IVR of (μ-pdt)[Fe $(CO)_3]_2$ is exquisitely sensitive to the chain length of the alkane solvent.[37-38] Although a similar investigation has not been performed for polar solvents (and in fact would be almost impossible due to the overlap of modes 3-4 in all polar solvents tested), this does strongly suggest that specific solvent-solute interactions might play a prominent role in the fast phase of IVR immediately following vibrational excitation, even in non-polar and non-interacting solvents. As previously discussed, one interpretation of the spectral diffusion data is that the presence of the dendritic groups exerts some degree of modulation on the solvent-solute interactions of the carbonyl ligands. An alternative interpretation of the significant slow-down in early IVR observed in many of the dendrimer solutions is that this slow-down arises from the modulation of solvent assistance in the IVR process. This hypothesis is also supported by the observation of unaffected vibrational relaxation in DMF and THF, in which the dendritic groups are expected to be minimally contracted and thus the carbonyl groups are expected to be at least somewhat solvent-exposed. A strong solvent-effect in intracarbonyl IVR is not unprecedented, as previous work has shown that in alcohol solutions of DMDC, specifically ethanol and butanol, the rate of intracarbonyl IVR is strongly influenced by specific solvent-solute conformations and interactions.[39]

Although additional work is certainly needed to clarify the trends observed in our data, especially similar experiments on larger-generation poly(aryl ether) dendrimers, our data offers an informative exploration of the dynamical changes associated with encapsulation in molecular assembly of moderate size, particularly with respect to solvent-solute interactions. Unlike small-molecules, which are typically relatively rigid and fully solvent-exposed, and unlike the pocket of an enzyme active site, which tend to be completely or almost completely shielded from the solvent, our data provides an example of a system which flexible enough to be solvent-exposed, but in which the solvent-solute interaction is modulated by the conformational mobility of the dendritic assembly. The comprehensive picture which emerges from our data is of a conformationally flexible molecular assembly, which in most cases modulates but does not significantly inhibit the solvent-solute interactions associated with the diiron hexacarbonyl core. This modulation

is evident even in our FTIR spectra, where the presence of the dendrimer does not remove whatever solvent-solute interactions give rise to a distinct solvent-dependent delineation of mode 1's vibrational frequency, but does cause that delineation to be most apparent in mode 2 instead of in mode 1. The presence of a dendrimer also invariably gives rise to an additional timescale in the decay of spectral inhomogeneity, which we suggest reflects the continuous response of the solvent to the conformational mobility of the dendritic assembly. Finally, in poorer solvents for poly(aryl-ether) dendrimers a distinct slowdown of the fast intracarbonyl IVR is apparent for the dendrimer, which we are unable to unambiguously interpret.

In acetonitrile, the poorest solvent for poly(aryl-ether) dendrimers, a massive slowdown in what we interpret to be the slow response of the solvent to the conformational mobility of the dendritic groups is observed. We suggest that this is a directly reflects the folding of the dendritic groups around the diiron hexacarbonyl core, and thus that measurements of spectral diffusion may be directly used to probe the solvent-dependent conformation of a macromolecular sample.

4.5 Conclusion

The work in detailed in this chapter represents the first 2D-IR study of a dendritic assembly, in which the vibrational dynamics of the dendrimer's diiron hexacarbonyl core are directly compared to a small-molecule version of the same molecular unit. The testing of six different solvent systems enabled us to identify an unusual solvent-dependence of the vibrational frequency of one vibrational mode in the reference small molecule and another in vibrational mode in the dendrimer. We find that the presence of a dendritic assembly often, but not always, significantly slows the initial IVR of the carbonyl groups, although whether this is due primarily to inter- or intra-molecular processes remains unclear. The fast phase of the decay of the carbonyl groups' spectral inhomogeneity in the dendritic molecule seems to be modulated to a roughly uniform timescale of 2.5 ps, and an additional timescale of spectral diffusion absent in the reference small molecule reveals clear signatures of slow solvent fluctuations in response to the conformational fluctuations of the poly(aryl ether) dendritic assemblies. This conformational flexibility is more similar

to that of a large biomolecule than to a more rigid small molecule, but the size and steric effect of the dendrimer are small enough to retain many similarities to the small molecules, including the solvent-accessibility of the molecule's active site. Further work should focus on larger-generation poly(aryl ether) dendrimers, where a change in the visible spectrum of a poly(aryl ether) monodendron was reported between the third and fourth generation, suggesting the onset of a globular and back-folding conformation.[28] A similar transition has been suggested from NMR work on poly(aryl ether) dendritic complexes.[40] Examination of these larger systems will test the trends we report here from smaller-generation dendrimers, and advance the understanding of the ultrafast dynamics induced by conformationally-dynamic nanoconfinement.

References

1. Bistri, O.; Reinaud, O., Supramolecular Control of Transition Metal Complexes in Water by a Hydrophobic Cavity: a Bio-Inspired Strategy. *Org Biomol Chem* **2015,** *13*, 2849-2865.

2. Zhao, M.; Wang, H. B.; Ji, L. N.; Mao, Z. W., Insights into Metalloenzyme Microenvironments: Biomimetic Metal Complexes with a Functional Second Coordination Sphere. *Chem Soc Rev* **2013,** *42*, 8360-8375.

3. Gray, H. B.; Winkler, J. R., Electron Transfer in Proteins. *Annu Rev Biochem* **1996,** *65*, 537-561.

4. Miesfeld, R. L.; McEvoy, M. M., *Biochemistry*. First edition. ed.; W.W. Norton & Company: New York, 2017.

5. Cram, D. J.; Karbach, S.; Kim, Y. H.; Baczynskyj, L.; Kalleymeyn, G. W., Shell Closure of 2 Cavitands Forms Carcerand Complexes with Components of the Medium as Permanent Guests. *J Am Chem Soc* **1985,** *107*, 2575-2576.

6. Breslow, R.; Dong, S. D., Biomimetic Reactions Catalyzed by Cyclodextrins and their Derivatives. *Chem Rev* **1998,** *98*, 1997-2011.

7. Breslow, R., Biomimetic Chemistry and Artificial Enzymes - Catalysis by Design. *Accounts Chem Res* **1995,** *28*, 146-153.

8. Natarajan, N.; Brenner, E.; Semeril, D.; Matt, D.; Harrowfield, J., The Use of Resorcinarene Cavitands in Metal-Based Catalysis. *Eur J Org Chem* **2017**, 6100-6113.

9. La Manna, P.; De Rosa, M.; Talotta, C.; Gaeta, C.; Soriente, A.; Floresta, G.; Rescifina, A.; Neri, P., The Hexameric Resorcinarene Capsule as an Artificial Enzyme: Ruling the Regio and Stereochemistry of a 1,3-Dipolar Cycloaddition Between Nitrones and Unsaturated Aldehydes. *Org Chem Front* **2018,** *5*, 827-837.

10. Wieser, C.; Dieleman, C. B.; Matt, D., Calixarene and Resorcinarene Ligands in Transition Metal Chemistry. *Coordin Chem Rev* **1997,** *165*, 93-161.

11. Shivanyuk, A.; Rebek, J., Reversible Encapsulation by Self-Assembling Resorcinarene Subunits. *P Natl Acad Sci USA* **2001,** *98*, 7662-7665.

12. Ballester, P.; Fujita, M.; Rebek, J., Molecular Containers. *Chem Soc Rev* **2015,** *44*, 392-393.

13. Rebek, J., Host-Guest Chemistry of Calixarene Capsules. *Chem Commun* **2000**, 637-643.

14. Dalgarno, S. J.; Power, N. P.; Atwood, J. L., Metallo-Supramolecular Capsules. *Coordin Chem Rev* **2008,** *252*, 825-841.

15. Shi, Q. X.; Mower, M. P.; Blackmond, D. G.; Rebek, J., Water-Soluble Cavitands Promote Hydrolyses of Long-Chain Diesters. *P Natl Acad Sci USA* **2016,** *113*, 9199-9203.

16. De Rosa, M.; La Manna, P.; Talotta, C.; Soriente, A.; Gaeta, C.; Neri, P., Supramolecular Organocatalysis in Water Mediated by Macrocyclic Compounds. *Front Chem* **2018,** *6,* 1-16.

17. Zhang, G.; Mastalerz, M., Organic Cage Compounds - from Shape-Persistency to Function. *Chem Soc Rev* **2014,** *43*, 1934-1947.

18. Helms, B.; Frechet, J. M. J., The Dendrimer Effect in Homogeneous Catalysis. *Adv Synth Catal* **2006,** *348*, 1125-1148.

19. Hecht, S.; Frechet, J. M. J., Dendritic Encapsulation of Function: Applying Nature's Site Isolation Principle from Biomimetics to Materials Science. *Angew Chem Int Edit* **2001,** *40*, 74-91.

20. Li, X. Q.; Wang, M.; Zheng, D. H.; Han, K.; Dong, J. F.; Sun, L. C., Photocatalytic H_2 Production in Aqueous Solution with Host-Guest Inclusions Formed by Insertion of an FeFe-hydrogenase Mimic and an Organic Dye into Cyclodextrins. *Energ Environ Sci* **2012,** *5*, 8220-8224.

21. Yu, T. J.; Zeng, Y.; Chen, J. P.; Zhang, X. H.; Yang, G. Q.; Li, Y., Efficient Photochemical Production of Hydrogen in Aqueous Solution by Simply Incorporating a Water-Insoluble Hydrogenase Mimic into a Hydrogel. *J Mater Chem A* **2014,** *2*, 20500-20505.

22. Frederix, P. W. J. M.; Kania, R.; Wright, J. A.; Lamprou, D. A.; Ulijn, R. V.; Pickett, C. J.; Hunt, N. T., Encapsulating [FeFe]-hydrogenase Model Compounds in Peptide Hydrogels Dramatically Modifies Stability and Photochemistry. *Dalton T* **2012,** *41*, 13112-13119.

23. Wang, F.; Liang, W. J.; Jian, J. X.; Li, C. B.; Chen, B.; Tung, C. H.; Wu, L. Z., Exceptional Poly(acrylic acid)-Based Artificial [FeFe]-Hydrogenases for Photocatalytic H-2 Production in Water. *Angew Chem Int Edit* **2013,** *52*, 8134-8138.

24. Jian, J. X.; Liu, Q.; Li, Z. J.; Wang, F.; Li, X. B.; Li, C. B.; Liu, B.; Meng, Q. Y.; Chen, B.; Feng, K.; Tung, C. H.; Wu, L. Z., Chitosan Confinement Enhances Hydrogen Photogeneration from a Mimic of the Diiron Subsite of [FeFe]-hydrogenase. *Nat Commun* **2013,** *4,* 1-6.

25. Yu, T. J.; Zeng, Y.; Chen, J. P.; Li, Y. Y.; Yang, G. Q.; Li, Y., Exceptional Dendrimer-Based Mimics of Diiron Hydrogenase for the Photochemical Production of Hydrogen. *Angew Chem Int Edit* **2013,** *52*, 5631-5635.

26. Ortiz, A. M.; Sanchez-Mendez, A.; de Jesus, E.; Flores, J. C.; Gomez-Sal, P.; Mendicuti, F., Poly(benzyl ether) Dendrimers Functionalized at the Core with Palladium Bis(N-Heterocyclic Carbene) Complexes as Catalysts for the Heck Coupling Reaction. *Inorg Chem* **2016,** *55*, 1304-1314.

27. De Backer, S.; Prinzie, Y.; Verheijen, W.; Smet, M.; Desmedt, K.; Dehaen, W.; De Schryver, F. C., Solvent Dependence of the Hydrodynamical Volume of Dendrimers with a Rubicene Core. *J Phys Chem A* **1998,** *102*, 5451-5455.

28. Riley, J. M.; Alkan, S.; Chen, A. D.; Shapiro, M.; Khan, W. A.; Murphy, W. R.; Hanson, J. E., Pyrene-labeled poly(aryl ether) monodendrons: Synthesis, characterization, diffusion coefficients, and photophysical studies. *Macromolecules* **2001,** *34*, 1797-1809.

29. Stanley, J. L.; Rauchfuss, T. B.; Wilson, S. R., Studies on the condensation pathway to and properties of diiron azadithiolate carbonyls. *Organometallics* **2007,** *26*, 1907-1911.

30. Hartwig, J. F., *Organotransition Metal Chemistry : from Bonding to Catalysis*. University Science Books: Sausalito, Calif., 2010.

31. Pani, R. C.; Yingling, Y. G., Role of Solvent and Dendritic Architecture on the Redox Core Encapsulation. *J Phys Chem A* **2012,** *116*, 7593-7599.

32. Nishida, J.; Tamimi, A.; Fei, H. H.; Pullen, S.; Ott, S.; Cohen, S. M.; Fayer, M. D., Structural dynamics inside a functionalized metal-organic framework probed by ultrafast 2D IR spectroscopy. *P Natl Acad Sci USA* **2014,** *111*, 18442-18447.

33. Uzer, T.; Miller, W. H., Theories of Intramolecular Vibrational-Energy Transfer. *Phys Rep* **1991,** *199*, 73-146.

34. Stratt, R. M.; Maroncelli, M., Nonreactive Dynamics in Solution: The Emerging Molecular View of Solvation Dynamics and Vibrational Relaxation. *J Phys Chem-Us* **1996,** *100*, 12981-12996.

35. Park, K. H.; Jeon, J.; Park, Y.; Lee, S.; Kwon, H. J.; Joo, C.; Park, S.; Han, H.; Cho, M., Infrared Probes Based on Nitrile-Derivatized Prolines: Thermal Insulation Effect and Enhanced Dynamic Range. *J Phys Chem Lett* **2013,** *4*, 2105-2110.

36. Delor, M.; Sazanovich, I. V.; Towrie, M.; Spall, S. J.; Keane, T.; Blake, A. J.; Wilson, C.; Meijer, A. J. H. M.; Weinstein, J. A., Dynamics of Ground and Excited State Vibrational Relaxation and Energy Transfer in Transition Metal Carbonyls. *J Phys Chem B* **2014,** *118*, 11781-11791.

37. Eckert, P. A.; Kubarych, K. J., Dynamic Flexibility of Hydrogenase Active Site Models Studied with 2D-IR Spectroscopy. *J Phys Chem A* **2017,** *121*, 608-615.

38. Banno, M.; Sato, S.; Iwata, K.; Hamaguchi, H., Solvent-dependent Intra- and Intermolecular Vibrational Energy Transfer of $W(CO)_6$ Probed With Sub-Picosecond Time-Resolved Infrared Spectroscopy. *Chem Phys Lett* **2005,** *412*, 464-469.

39. King, J. T.; Anna, J. M.; Kubarych, K. J., Solvent-Hindered Intramolecular Vibrational Redistribution. *Phys Chem Chem Phys* **2011,** *13*, 5579-5583.

40. Wooley, K. L.; Klug, C. A.; Tasaki, K.; Schaefer, J., Shapes of dendrimers from rotational-echo double-resonance NMR. *J Am Chem Soc* **1997,** *119*, 53-58.

Chapter 5
Vibrational Coherence Transfer in a Class of Excitonic Biomimetic Catalysts Studied with 2D-IR Spectroscopy

5.1 Introduction

One of the most pressing and controversial current political issues is the dilemma posed by climate change. Greenhouse gas emissions, which underlie the energy-production processes of modern society, have been clearly implicated in a number of undesirable environmental phenomena, including atmospheric warming and ocean acidification.[1-2] The global economy is heavily dependent upon the energy harvested by processes which generate these greenhouse gas emissions, and another different form of energy harvesting is necessary. Solar power offers a promising alternative to fossil fuels; the sun is a powerful, continuously renewable energy source, and solar energy needs only to be harvested. Unfortunately, this is easier said than done. Commercial solar panels are only ~ 20% efficient, and more efficient light harvesting materials are either undeveloped or prohibitively expensive.[3] A direct comparison of the photosynthetic efficiency of natural and artificial systems is somewhat complicated,[4] but physical scientists look to natural light-harvesting systems for inspiration in the design of artificial light-harvesting systems.[5] One key to efficient harvesting of solar energy in biological systems may involve the presence and longevity of specific superpositions of quantum states in photosynthetic assemblies.

Biological light-harvesting systems are typically excitonic systems in which photoexcitation induces a delocalized electronic excited state within the assembly, which is subsequently transferred elsewhere as part of the light-harvesting process.[6-9] The physics of such excitonic systems have been extensively investigated, and a wide range of molecular and supramolecular systems are modeled as excitons.[10-13] The simplicity of the

exciton model allows the physical characteristics of molecular systems as disparate as small-molecule metal carbonyl complexes and supramolecular light-harvesting assemblies to be modeled using essentially the same Hamiltonian,[14] and makes experimental data from one excitonic system relevant to any other, regardless of other molecular differences.

It is widely known that vibrational coherences may play a significant role in the reactivity and charge transfer processes of a variety of molecular systems,[15-23] but in 2007 the subject received renewed attention when Engel et. al. reported the observation of long-lived oscillatory features in the 2D electronic spectra of the Fenna-Matthews-Olsen (FMO) light-harvesting assembly. They interpreted these to be coherences between electronic excitonic states, and hypothesized that these coherences enhanced the function of the light-harvesting assembly by effectively computing the optimum pathway for charge transfer within the assembly.[24] Since then occurrence and role of coherences in biomolecular light-harvesting have been the subject of intense research and discussion.[25-28] While it seems to be generally accepted that unusually long-lived oscillatory features do indeed occur in the 2D electronic spectra of the FMO assembly, Photosystem II, and other biomolecular light-harvesting complexes, the nature, longevity, and relevance of these coherences to photosynthetic function remains uncertain.[28-31] If vibronic or electronic coherences are instrumental in the biomolecular light-harvesting then biomimetic design to incorporate similar coherences in artificial light-harvesting devices may significantly increase the capacity of modern solar arrays. The key challenge is then to ascertain whether vibronic coherences do significantly participate in the light-harvesting process, and to determine the physical and molecular design necessary to reproduce such coherences in an artificial system.

We report here the observation of what appear to be spectral signatures of vibrational coherence transfer in the 2D infrared (2D-IR) spectra of several biomimetic diiron hexacarbonyl compounds. The signatures of vibrational coherence transfer which we report appear to indicate that diiron hexacarbonyl compounds are predisposed to coherence-coherence and coherence-population transfers similar to the quantum transport reported in biomolecular light-harvesting assemblies.[26] Despite being completely different from biomolecular light-harvesting assemblies on a molecular level, moderately-sized

metal carbonyl complexes display similar excitonic behavior,[14] and our data may shed significant light on the question of whether specific physical conditions predispose excitonic systems to coherence transfer phenomena.

Reports of coherence transfer in experimental 2D-IR spectra have been largely limited to $Rd(CO)_2$(acetylacetonato) (RDC), a small organometallic complex with two strong carbonyl vibrations. In 2004 Khalil et al. suggested that two of the peaks in RDC's 2D-IR spectrum were due to coherence transfer.[32] This was later disputed by Marroux et. al., who used carefully shaped experimental pulses to demonstrate that intercarbonyl coherence transfer is probably negligible in RDC.[33] The Wright group has published several studies of coherence transfer in RDC using a different set of experimental phase-matching conditions than Khalil and Marroux.[34-35] Nee et. al. observed multiple frequency components in the cross peaks of dimanganese dodecacarbonyl (DMDC) and interpreted them as signature of vibrational coherence transfer.[36] Subsequent modeling of DMDC Baiz et. al. using Redfield theory showed that the same cross peak oscillatory features occurred when coherence-coherence transfer terms were explicitly included in the model.[37] In continuation of the studies reported by Nee and Baiz we report the observation of multiple cross peak oscillatory frequencies in the cross peaks of several diiron hexacarbonyl mimics of the [FeFe]-hydrogenase enzyme. We find distinct patterns in the data of all three compounds, and propose that both coherence-coherence and coherence-population transfer contribute to the dynamics in our systems of diiron hexacarbonyls.

5.2 Experimental Methods

All synthetic procedures were performed under nitrogen using standard Schlenk-line procedures. All reagents were ordered from Sigma Aldrich and used as received.
(μ-1,2-ethanedithiolate)$[Fe(CO)_3]_2$: This compound was synthesized according to the procedure outlined by Lyon et. al.[38] Here, equimolar 1,2-ethanedithiolate and $Fe_3(CO)_{12}$ were mixed in 40 ml of toluene and the reaction mixture was refluxed for 3 hours. The solvent was then removed under vacuum to yield the reddish-brown crude product, which was purified on a silica gel column with hexanes as the eluent and recrystallized from a saturated hexanes solution.

(μ-o-xylyldithiolate)[$Fe(CO)_3$]$_2$: This compound was synthesized according to the procedure described by Lyon et al.[38] Here, 1.02 g of o-xylyldithiolate and 3.02 of $Fe_3(CO)_{12}$ were mixed in 250 ml of toluene and refluxed overnight. The solvent was removed under vaccum to yield the reddish-brown crude product, which was purified on a silica gel column using hexanes as the eluent and subsequently recrystallized from hexanes.

Synthesis of [Fe(μ-S)$(CO)_3]_2$: The synthetic method described by Stanley et. al.[39] was employed. Briefly, 12 mL of $Fe(CO)_5$ were mixed with 60 mL of methanol and 35 mL of concentrated KOH. After cooling the reaction mixture in an ice bath 16 g of elemental sulfur were added slowly over the course of ~ 10 minutes. The reaction mixture was stirred for an hour and 140 mL of distilled H_2O, 42 g of NH_4Cl and 350 mL of hexanes were added. The reaction was removed from the ice bath and stirred overnight. The layer of hexanes was decanted from the reaction mixture and the reaction mixture was extracted with hexanes until the extraction layers were uncolored. The extractions were combined with the hexanes initially removed from the reaction mixture, and the combined fractions were rotovapped away leaving the reddish-brown crude product. The crude product was purified on a silica gel column with hexanes as the eluent.

Data acquisition and processing: All data sets were finely sampled for the first 12 ps of waiting time, and sparsely sampled afterward up until ~ 80 ps. To avoid the introduction of any artifacts from slow drift of the experimental set-up, waiting time data points were collected in randomized order. To create the coherence maps the absolute-value 2D data sets were interpolated along t_2 to generate evenly spaced data points, and a Fourier transformation was performed over t_2 axis to yield spectra as a function of ω_2. This operation yields t_2-frequency-dependent peak amplitude in the 2D spectrum and is often used in 2D electronic spectroscopy.[29, 31] The power spectrum was used to create the coherence maps presented in this study.

5.3 Results

Three different diiron hexacarbonyl complexes are used in this study, and they are shown in Figure 5.1. All three have a diiron hexacarbonyl core, and differ in the bridging disulfide group; two are bridged by organic groups, and ethanedithiolate (edt) and an o-

xylyldithiolate (xyl), respectively, while in the third the disulfides are not bridged by any organic group. All data referenced in this study was collected using hexadecane as the solvent. The infrared spectra of all three are shown in Figure 5.1.

As we have previously noted, the CO vibrations of $[Fe(\mu\text{-}S)(CO)_3]_2$ are blue shifted by several wavenumbers relative to the vibrations of the edt- and xylyl-bridged compounds.

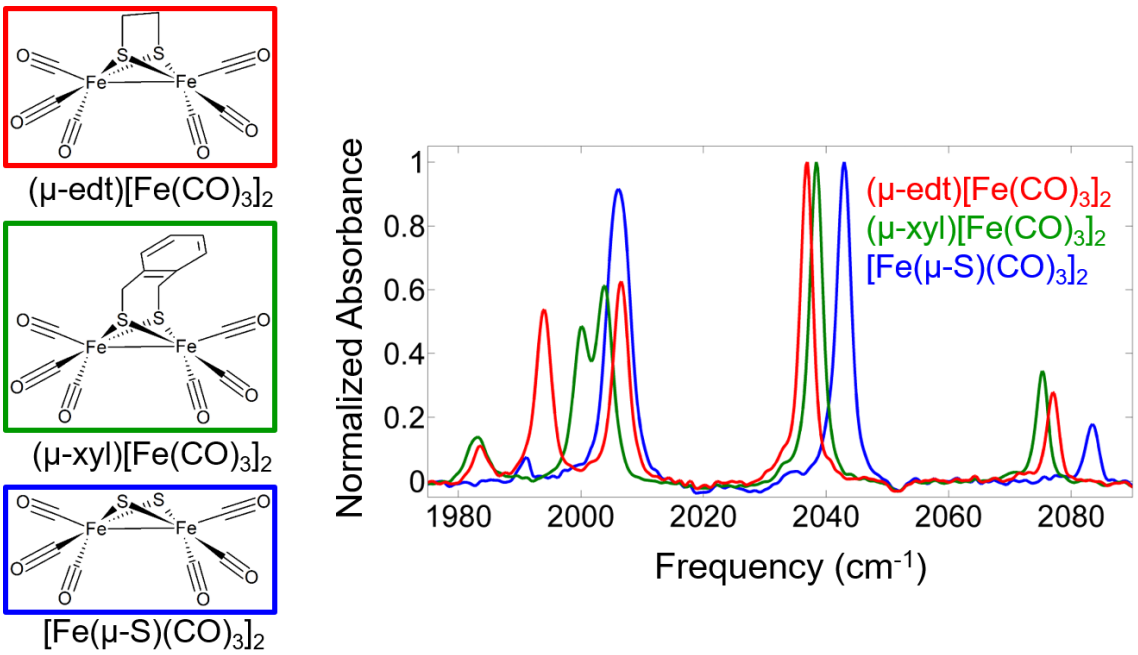

Figure 5.1: Molecular structures of the three diiron hexacarbonyl compounds tested in this study and infrared spectra of their carbonyl stretching vibrations. In $[Fe(\mu\text{-}S)(CO)_3]_2$ the vibrational band at ~ 2005 cm^{-1} arises from two degenerate modes which are not degenerate in either of the other compounds. All data was collected in hexadecane solvent.

This is comparable to the data shown in Chapter 4, and we suggest that the electron density of the diiron core is slightly increased by the organic disulfide bridge. The presence of an organic bridging group appears to separate the vibrational frequencies of modes 3 and 4 to varying degrees, and in the disulfide modes 3 and 4 are degenerate.

Sample rephasing coherence maps of the edt and xyl compounds are shown in Figure 5.2-5.4. To ensure clarity in our discussion of the coherence maps we will refer to frequencies of excitation and detection by the corresponding mode number. For example, the cross peak at (ω_1=mode 1, ω_3 = mode 2) will be denoted as (**1**, **2**). Figure 5.2A shows the 71-73 cm^{-1} frequency in the rephasing spectrum of xyl. It occurs only on the (**1**, **4**) cross peak and its conjugate, as expected. Figure 5.2B shows the 36-39 cm^{-1} frequency in

rephasing spectrum of xyl. That frequency is expected for the (**1**, **2**) cross peak and its conjugate, but is not expected for the (**1**, **4**) cross peak and its conjugate. Figure 5.2C shows the 80-83 cm^{-1} frequency components of the nonrephasing edt spectrum. The 80-83 cm^{-1}

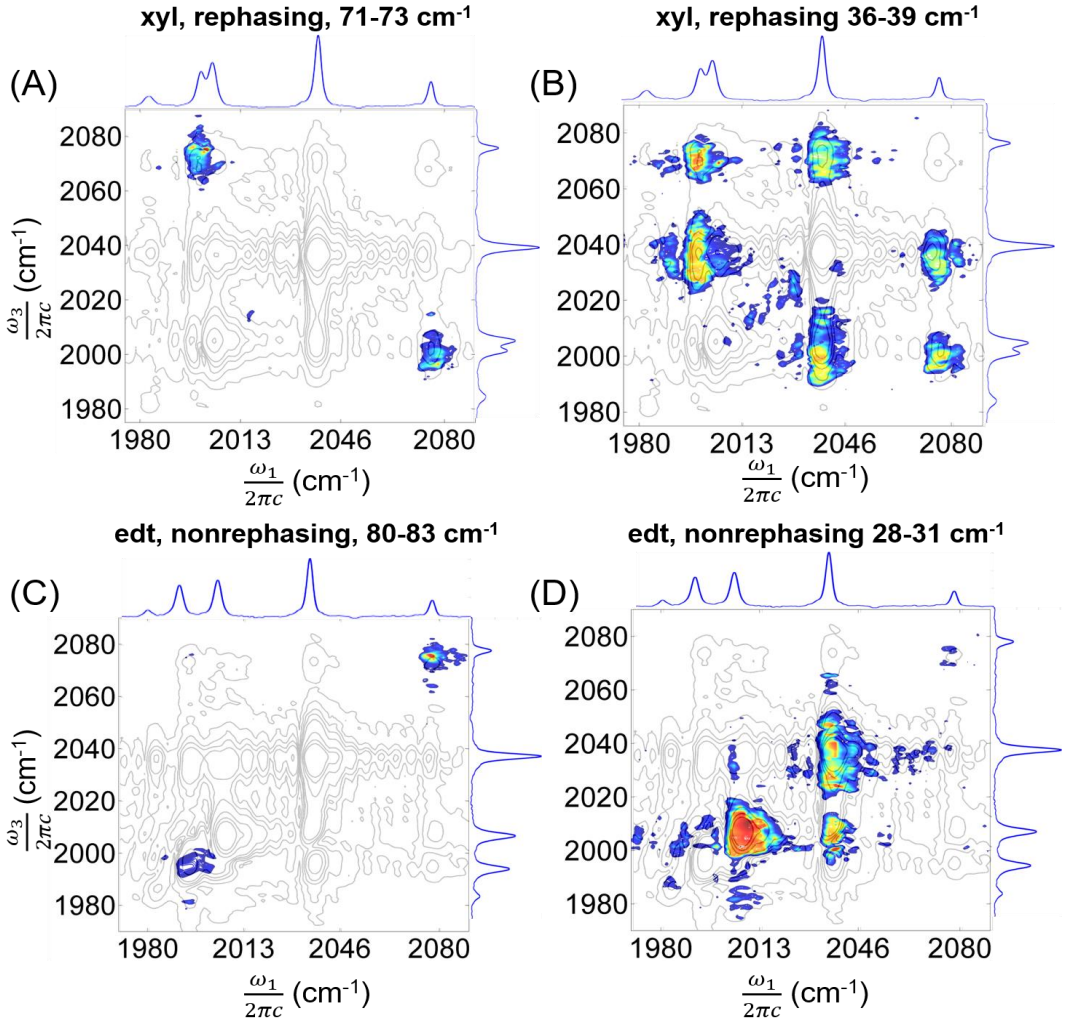

Figure 5.2: Spectra shown are coherence maps depicting the intensity of oscillatory features during t_2 by their frequencies of excitation and detection. (A) 71-73 cm^{-1} frequency in the rephasing spectra of xyl. The difference frequency of mode 1 and mode 4 in xyl is 72 cm^{-1}, and a 72 cm^{-1} oscillatory feature is expected on the (**1**, **4**) cross peak and its conjugate in rephasing spectra. (B) 36-39 cm^{-1} frequency in the rephasing spectra of xyl. The difference frequency of mode 1 and mode 2 in xyl is 37 cm^{-1}, and that difference frequency is expected on the (**1**, **2**) cross peak and its conjugate in rephasing spectra. A 37 cm^{-1} frequency is not expected on the (**1**, **4**) cross peak or its conjugate. (C) 80-83 cm^{-1} frequency in the nonrephasing spectra of edt. The difference frequency of mode 1 and mode 4 in edt is 82 cm^{-1}, and a 82 cm^{-1} oscillatory feature is expected on the (**1, 1**) and (**4**, **4**) in nonrephasing spectra. (D) 28-31 cm^{-1} frequency in the nonrephasing spectra of edt. The difference frequency of mode 2 and mode 3 in edt is 30 cm^{-1}, and that difference frequency is expected on the (**2**, **2**) and (**3**, **3**) peaks in the nonrephasing spectra. A 30 cm^{-1} frequency is not expected on the (**2**, **3**) cross peak.

frequency is localized on (**1**, **1**) and (**4**, **4**) diagonal peaks, as expected. Figure 5.2D shows the 28-31 cm^{-1} oscillatory components of the nonrephasing edt spectrum. This frequency is expected for the (**2**, **2**) and (**3**, **3**) diagonal peaks, but not for the (**1**, **4**) cross peak.

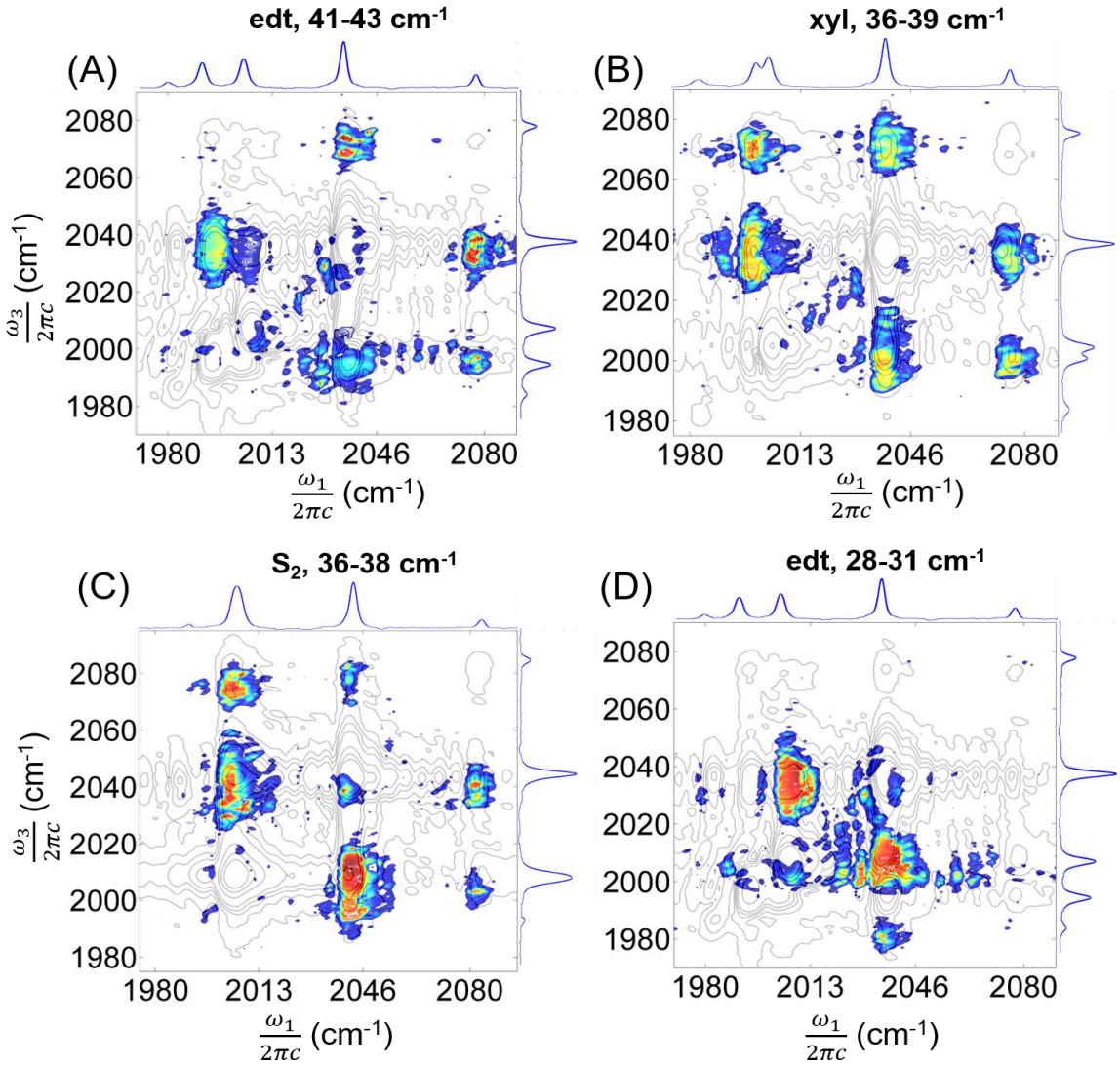

Figure 5.3: Spectra shown are coherence maps depicting the intensity of oscillatory features during t_2 by their frequencies of excitation and detection. All coherence maps are from rephrasing spectra. (A) 41-43 cm^{-1} frequency in edt. The difference frequency of mode 1 and mode 2 in edt is 42 cm^{-1} and the difference of modes 2 and 4 is almost the same. A 42 cm^{-1} oscillatory feature is unexpected on the (**1**, **4**) cross peak. (B) 36-39 cm^{-1} frequency in xyl. The difference frequency of mode 1 and mode 2 in xyl is 37 cm^{-1}, and the difference of mode 2 and 4 is almost the same. A 37 cm^{-1} frequency is unexpected on the (**1**, **4**) cross peak and its conjugate. (C) 36-38 cm^{-1} frequency in the spectra of S_2. The difference frequency of mode 1 and mode 2 in S2 is 37 cm^{-1} and the difference of modes 2 and 4 is almost the same. An oscillatory frequency of 37 cm^{-1} is unexpected for the (**1**, **4**) cross peak and its conjugate. (D) 28-31 cm^{-1} frequency in the rephasing spectra of edt. The difference frequency of mode 2 and mode 3 in edt is 30 cm^{-1}. A 30 cm^{-1} frequency is unexpected on the (**2**, **5**) cross peak.

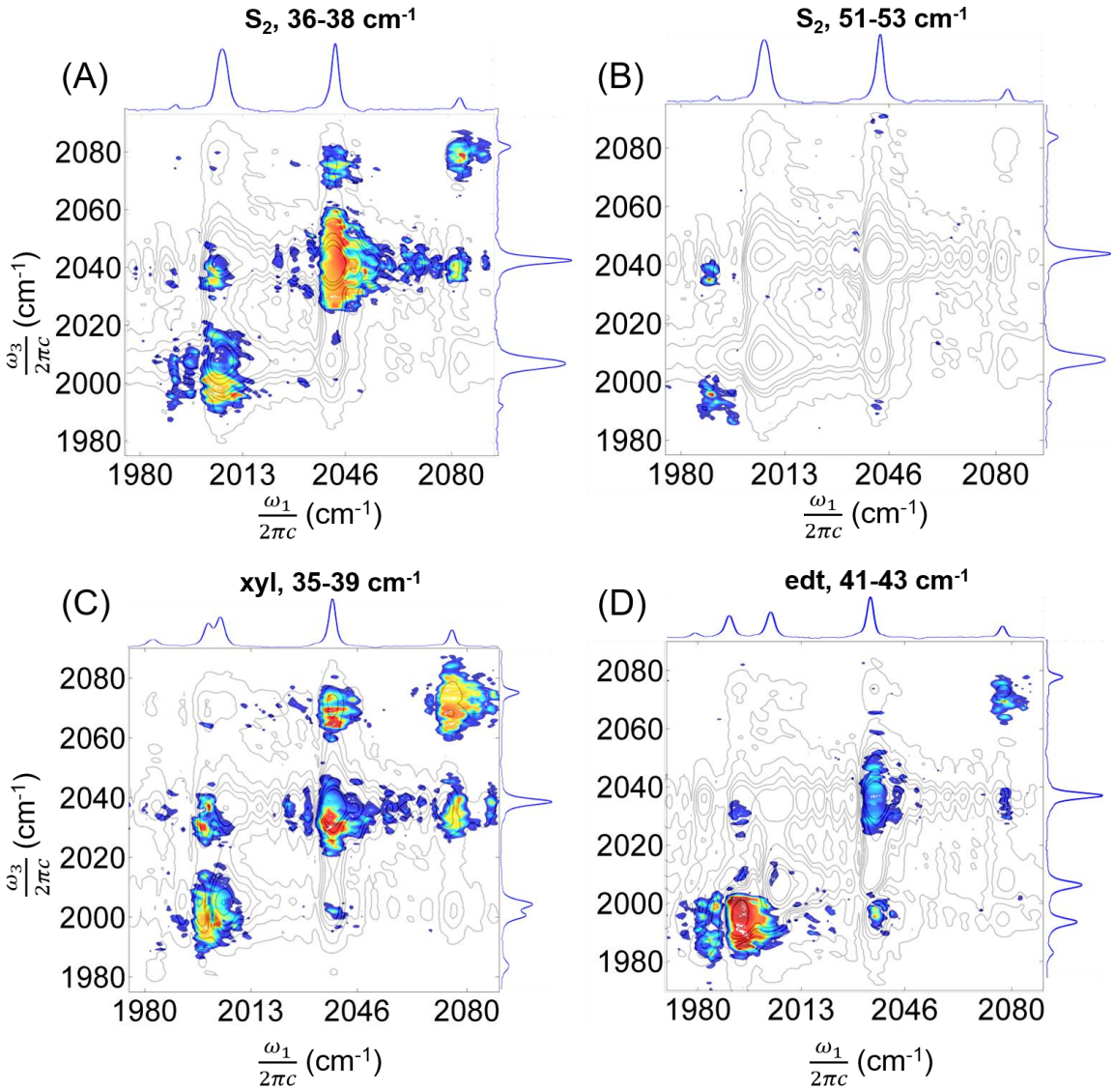

Figure 5.4: Spectra shown are coherence maps depicting the intensity of oscillatory features during t_2 by their frequencies of excitation and detection. All data are from nonrephrasing spectra. (A) 36-38 cm^{-1} frequencies in S_2. The difference frequency of mode 1 and mode 2 in S_2 is 37 cm^{-1} and the difference of modes 2 and 4 is almost the same. A 37 cm^{-1} oscillatory feature is unexpected on any cross peak. (B) 51-53 cm^{-1} frequency in S_2. The difference frequency of mode 2 and mode 5 in S2 is 52 cm^{-1}. A 52 cm^{-1} frequency is unexpected on any cross peak. (C) 35-39 cm^{-1} frequency in the spectra of xyl. The difference frequency of mode 1 and mode 2 in S_2 is ~37 cm^{-1} and the difference of modes 2 and 4 is almost the same. An oscillatory frequency of 37 cm^{-1} is unexpected on any cross peak. (D) 41-43 cm^{-1} frequency in the spectra of edt. The difference frequency of mode 2 and mode 4 in edt is 42 cm^{-1}. A 42 cm^{-1} frequency is unexpected on any cross peak.

5.4 Discussion

Two-dimensional infrared spectroscopy measures the third-order nonlinear response of a sample to a sequence of three field interactions with the sample's transition dipole moments. This response may be written as a four-point correlation function of the system's transition dipole moments μ as in Equation 5.2,[40-42]

$$R^{(3)}_{ijkl}(\tau_3,\tau_2,\tau_1) = \left(\frac{-i}{\hbar}\right)^3 \langle\Big[\Big[\mu_i(\tau_3+\tau_2+\tau_1),\mu_j(\tau_2+\tau_1)\Big]\mu_k(\tau)\Big]\,\mu_l(0)\Big]\rangle \quad (5.1)$$

Where the indices *i*, *j*, *k*, and *l* represent the laboratory-frame polarization of the respective field and τ_n represents the time period between field-matter interactions *n* and *n*+1. Assuming that the vibrational and orientational response of the system are separable, the total response of the system may be written as a product of the two, as shown in Equation 5.3:[42]

$$R_{ijkl}(\tau_3,\tau_2,\tau_1) = \sum_{\nu\kappa\lambda\chi} R^{\nu\kappa\lambda\chi}(\tau_3\tau_2\tau_1)Y^{\nu\kappa\lambda\chi}_{ijkl}(\tau_3\tau_2\tau_1) \quad (5.2)$$

where $R^{\nu\kappa\lambda\chi}$ is the four-point correlation function of system's vibrational transition dipole moments ν, κ, λ, and χ with the four field-matter interactions, respectively, and $Y^{\nu\kappa\lambda\chi}_{ijkl}$ is the orientational response function of that correlation function, which accounts for the effect of orientational diffusion on the response of vibrational transition dipoles ν, κ, λ, and χ to field-matter interactions of *i*, *j*, *k*, and *l* polarizations, respectively. Note that the measured response of the system will include only pathways with nonvanishing orientational response functions.

By invoking the rotating wave approximation the vibrational response function defined in Equation 5.2 may be expressed as 16 individual four-point correlation functions, six of which are responses to the rephasing pulse sequence and six of which are responses to the nonrephasing pulse sequence.[40-41] These four-point correlation functions are often represented as Feynman diagrams to illustrate the time-dependent evolution of the system's density matrix, and this sequence of states is often referred to as a Liouville pathway.[41, 43] The Liouville pathways associated with rephasing and nonrephasing pulse sequences are shown in Figure 5.5. Liouville pathways are read upwards from the bottom, with the arrows representing field-matter interactions and the state of the density matrix

during each waiting written inside the diagram. Solid horizontal lines represent to field-matter interaction which delineates waiting times, and dashed horizontal lines are used to represent the occurrence of a coherence transfer during a waiting time when applicable.

The peaks in a 2D-IR spectrum to which pathways with coherences during t_2

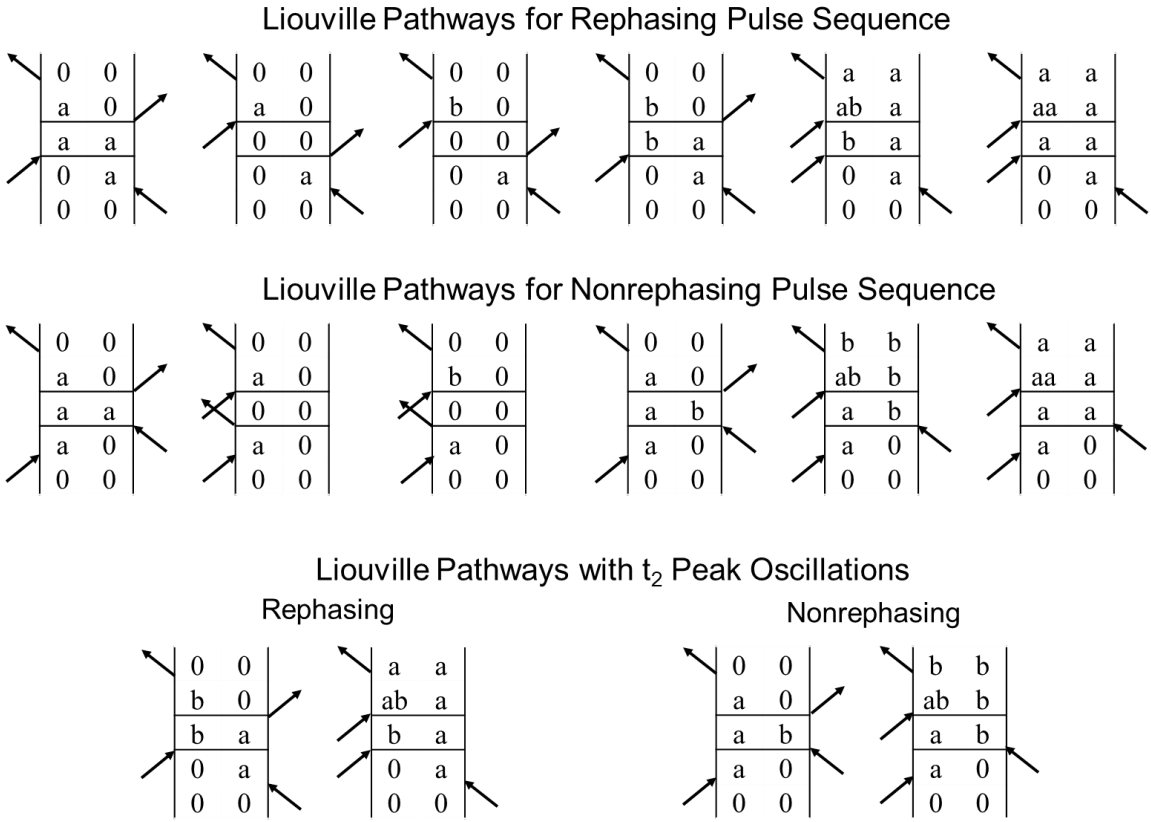

Figure 5.5: Top) Liouville diagrams associated with the rephasing pulse sequence, Middle) Liouville diagrams associated with the nonrephasing pulse sequence, and Bottom) Liouville pathways for both pulse sequences with t_2 oscillatory features. These pathways, where the system evolves in a coherent superposition of states during t_2, contribute to cross peaks in rephasing spectra, and to diagonal peaks in nonrephasing spectra.

contribute are observed to oscillate at the difference frequency of the two vibrations. The positions of such peaks vary depending upon the experimental pulse sequence, as is clear from Figure 5.3. In a nonrephasing experiment the pathways involving t_2 coherences contribute to peaks on the diagonal of the spectrum, and thus in a time-resolved nonrephasing experiment the nonrephasing peaks are expected to oscillate at the difference frequencies of that mode and all the others with which it shares a ground state. In a rephasing experiment the pathways involving t_2 coherences are contribute to off-diagonal cross peaks, each of which beats at the difference frequency of its two diagonal

peaks. In sum, in nonrephasing experiments the diagonal peaks oscillate at as many difference frequencies as there are other vibrational modes, and in rephasing experiments each cross peak oscillates at one difference frequency, that of the two modes for which it is a cross peak.[32, 41]

Several years ago Nee et. al. reported the observation of the cross peak in the rephasing 2D-IR spectra of dimanganese dodecacarbonyl's (DMDC) carbonyl vibrational modes.[36] This cross peak shows oscillatory features at not one but two frequencies, both of which correspond to a difference of vibrational modes within the system. As previously discussed, cross peaks in 2D-IR spectra are expected to only oscillate at only one frequency, and the presence of a second frequency component is anomalous within the usual secular approximation to Redfield theory, which is often used to model 2D-IR spectra. The Redfield equation is given in Equation 5.3,

$$\frac{\delta}{\delta t}\sigma_{jk}(t) = -i\omega_{jk}(t)\sigma_{jk}(t) + \sum_{lm} \Gamma_{jk,lm}\sigma_{lm}(t) \tag{5.3}$$

where ω_{jk} is the transition frequency between states *j* and *k*, σ is the reduced density matrix and $\Gamma_{jk,lm}$ is the element of the relaxation superoperator coupling the *jk* and *lm* elements of the reduced density matrix. Coherence-coherence transfer ($\Gamma_{ij,ik}$) and coherence-population transfer ($\Gamma_{ij,ii}$) terms are typically assumed to contribute negligibly to the system's dynamics and are set to zero – this is known as the secular approximation. Nee et. al. suggested to that the additional frequency component could arise from vibrational coherence transfer during one or more of the experimental waiting times. In a subsequent theoretical study Baiz et. al. compared the data reported by Nee. et. al. to 2D-IR spectra of DMDC simulated using Redfield theory but including the possibility for nonsecular terms to contribute.[36] When coherence-coherence coupling terms were included in the Redfield model the same cross peak oscillatory features reported by Nee et. al. were observed in the simulated 2D spectra, supporting the assignment of multi-frequency cross peak oscillations as spectral signatures of coherence transfer.

Unfortunately, only four of DMDC's ten carbonyl vibrational modes are IR-active, and two of these are degenerate.[36] DMDC's carbonyl vibrational spectrum thus consists of only three bands and two difference frequencies. This relative sparsity of IR-active

vibrations is sufficient to establish the presence of anomalous cross peak frequency components but inadequate to provide any significant insight into the dynamical phenomena associated with the vibrational coherence transfer. The diiron hexacarbonyl systems which we study here are quite different, with five of their six carbonyl vibrations being IR-active and none (in most cases) degenerate.[44-45] The relative abundance of vibrational bands and difference frequencies in these systems affords a wealth of experimental information that would be inaccessible in many of the "benchmark" metal carbonyl complexes that are commonly used in 2D-IR spectroscopy, like DMDC or RDC.

All three of the compounds tested in this study are generally similar in their carbonyl stretching IR spectra, and the vibrational displacements of each mode are comparable in all three. The greatest dissimilarity across the data sets is the frequency difference of modes 3 and 4. In edt and xyl the frequency difference is great enough to delineate between the two, but in the disulfide modes 3 and 4 are degenerate. We note that electronic structure calculations indicate the presence of a sixth carbonyl mode, with a frequency that is roughly between modes 4 and 5, but predict that this vibration is not IR-active. We will discuss this dark mode in greater detail below. Each of the tested compounds shows a unique set of anomalous frequency components (for example, only in edt does the (**2**, **5**) cross peak display anomalous frequency components), but the rephasing spectra of all thee tested compounds contain anomalous frequency components on the (**3**, **1**) and (**4**, **1**) cross peaks and the (**4**, **1**) excited state absorptions, as well as their conjugate cross peaks. These cross peak positions are shown in Figure 5.2B. The nonrephasing spectra of all three compounds contain anomalous frequencies at (**2**, **3**) and (**1**, **2**) and the conjugate cross peaks. These cross peak positions are shown in Figure 5.2D.

Phenomenologically, several patterns appear in all of the molecules we have investigated. In our rephasing data anomalous frequencies are invariably associated with mode 1, and occur on the cross peaks between mode 1 and modes 3-4. The anomalous frequencies associated with these peaks invariably correspond to the frequency difference of mode 1 and another carbonyl vibration, except for a frequency of ~ 88 cm^{-1} which we discuss further below. The excited state absorption of the (**1**, **4**) cross peak and its conjugate consistently displays a frequency which corresponds to the difference frequency of modes

1 and 2. In short, the anomalous frequency components in our rephasing spectra which occur in all three compounds invariably occur on cross peaks with mode 1, typically the (**1**, **4**) cross peak and its conjugate, and the anomalous frequencies associated with these peaks are all difference frequencies associated with mode 1.

Our nonrephasing data set displays similar patterns. Here notable oscillatory features occur on the cross peaks between modes 1 and 2 and between modes 2 and 3-4. These cross peak frequencies always correspond to the difference frequency of the two modes which contribute to the cross peak, and no nonrephasing cross peaks are observed to oscillate at more than one frequency. Essentially, the nonrephasing cross peak oscillatory features are exactly the features expected in a rephasing data set. Unlike the rephasing data set, where the anomalous cross peak frequencies are clearly associated with mode 1, in our nonrephasing data the anomalous frequencies tend to occur on cross peaks associated with mode 2.

To further investigate the origin of the anomalous frequency components of the cross peaks the orientational contribution to each vibrational response function must be considered. To this end, we define the laboratory frame axes as *x*, *y*, and *z*, and the molecular frame axes as *a*, *b*, and *c*. The orientation of the molecular frame is given by the Euler angles α, β, and γ, as depicted in Figure 5.6 according the convention used by Golonzka et. al.[42] The orientational response function determines the sequences of field-matter interactions which contribute to the measured response of the system, as written in Equation 5.2, and is defined by Equation 5.3-5.5:[42]

$$Y_{ijkl}^{\nu\kappa\lambda\chi}(\tau_3,\tau_2,\tau_1) = \int d\Omega_3 \int d\Omega_2 \int d\Omega_1 \int d\Omega_0 \, (\mu_\nu \cdot i) G(\Omega_3,\tau_3|\Omega_2) \times (\mu_\kappa \cdot j) G(\Omega_2,\tau_2|\Omega_1) \times (\mu_\lambda \cdot k) G(\Omega_1,\tau_1|\Omega_0)(\mu_\chi \cdot l) P(\Omega_0) \quad (5.4)$$

$$\int d\Omega = \int_0^{2\pi} d\alpha \int_0^{2\pi} d\gamma \int_0^{\pi} \sin\theta \, d\theta \quad (5.5)$$

$$G(\Omega_n,\tau_n|\Omega_{n-1}) = 8\pi^2 \sum_{J,K,M} \frac{1}{2J+1} e^{(-J(J+1)D_{or}\tau_n)} (D^J)_{K,M}(\Omega_n)(D^J)^*_{K,M}(\Omega_{n+1}) \quad (5.6)$$

where D_{or} is the molecular orientation diffusion coefficient and D^J are the Wigner matrices.[46-47] Equations 5.4-5.6 are fundamental descriptions of time-dependent orientational diffusion for spherical compounds, and represent a conditional probability

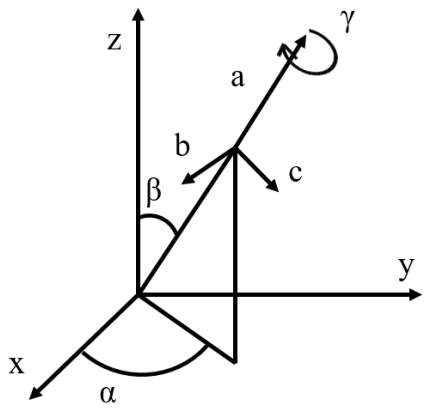

Figure 5.6: Depiction of the molecular and laboratory frame in which the orientational response is calculated. The laboratory frame is defined by axes x, y, and z, and the molecular frame is defined by axes a, b, and c. The relative orientation of the two frames of reference is given by the Euler angles α, β, and γ. For convenience the molecular transition dipole moments, all of which are orthogonal in this work, are taken to lie along each of the molecular axes, and the experimental electric fields are polarized along the three laboratory axes.

function for sequential field-matter interactions involving transition dipole moments ν, κ, λ, and χ.[48]

In the following analysis we adopt the naming convention used by Golonzka et. al. for evaluation of Equations 5.4-5.6.[42] For a system with two transition dipole moments **a** and **b**, each oriented along different principal axes of the molecular frame of reference, the allowed sequences of field-matter interactions with the two transition dipole moments are **aaaa**, **aabb**, **abab**, and **abba**. Each of our diiron hexacarbonyl variants has five transition dipole moments, two pairs of which are parallel, and has at least one transition dipole moment oriented along each of the primary axes of the molecular frame. Designating modes **1-5** as **a-e**, respectively, our system has transition dipole moments **a** || **d** ⊥ **b** || **e** ⊥ **c**. To test the possibility of additional sequences of field-matter interactions contributing to the response of our samples we evaluated to the orientational response function defined in Equation 5.4 for the sequences **abbc**, **abac**, **aabc**, and **baac**, where **a**, **b**, and **c** are orthogonal. Each of these sequences has a vanishing orientational response

function, showing that sequences of field-matter interactions with transition dipole moments oriented along each of the three primary molecular axes do not contribute to the measured response of the system. Thus, in our system the sequence of field-matter interactions with transition dipole moments **abbc** does not contribute to the measured response of the system, but the sequence **abbd** might, since parallel transition dipole moments of **a** and **d** make them interchangeable within the sequence, and **abba** is an allowed sequence of transition dipole moment interactions.

For a Liouville pathways including a coherence transfer during t_1 contribute to two different peaks in the spectrum – peaks at the excitation frequencies of the system pre- and post-transfer, which are uniformly detected at the single frequency of the system during t_3. If one of the t_1 coherences matches the t_3 coherence, one of the two peaks will lie on the diagonal of the spectrum at that frequency and the other will lie off the diagonal. If the t_3 coherence matches none of the t_1 coherences, all of the peaks that the pathway contributes to will lie off the diagonal of the spectrum. A Liouville pathway with a coherence transfer only during t_2 will contribute only to one peak, but that peak will oscillate at as many difference frequencies as the coherences it exists in during t_2. Finally, in the case of a coherence transfer during t_3, if the transition dipole moments of both the initial and final states of the coherence transfer are parallel the spectral response will be analogous to that of the t_1 coherence, but here the pathway will contribute to peaks with multiple detection frequencies but with the same frequency of excitation. In the case of a coherence transfer during t_3 where the states after and before coherence transfer have orthogonal transition dipole moments only one of them will contribute to the system's response function (the other will correspond to a forbidden sequence of field-matter interactions), and the pathway will contribute only to one peak on the spectrum.

The experimental data and the allowed sequences of transition dipole interactions significantly constrain the Liouville pathways which might contribute to our anomalous spectral features. For example, there are no significant oscillatory features on any of the diagonal peaks in our rephasing spectra, and thus no potential rephasing pathways may include the same state during both t_1 and t_3, as such pathways would contribute to peaks which are detected on the diagonal of the spectrum. Our nonrephasing data is less strictly

constrained since oscillations of the diagonal peaks are expected in nonrephasing spectra, and contributions to the diagonal peaks from coherence transfer pathways would be masked by the contributions from pathways without coherence transfer. As such, it is relatively straightforward to write a set of potential Liouville pathway for the nonrephasing cross peak oscillations, especially since t_2 coherence-coherence transfer may be effectively

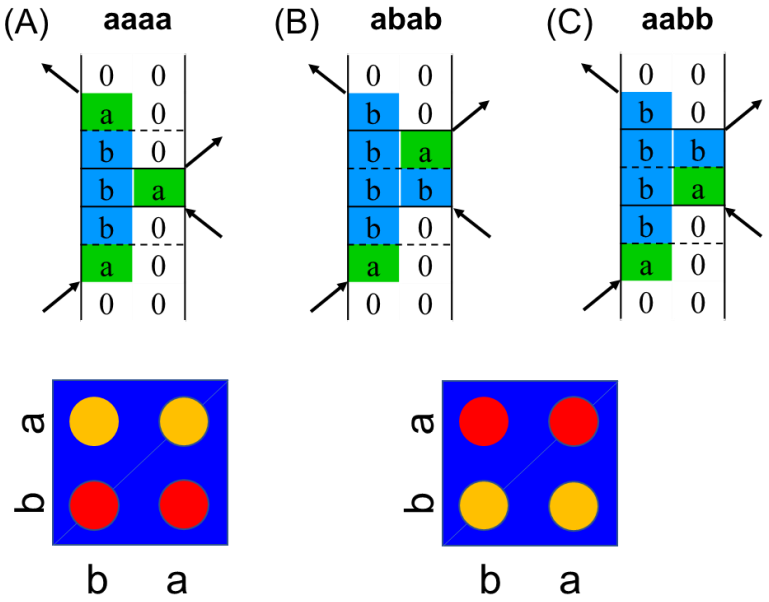

Figure 5.7: Potential Liouville pathways for the nonrephasing cross peak oscillations. In the cartoon 2D spectra orange circles represent peaks to which the Liouville diagrams above the spectra will contribute. (A) t_1 and t_3 coherence transfer. If the two states during t_3 have orthogonal transition dipole moments only one will contribute to the measured response. (B) Population-to-coherence transfer pathway. (C) Coherence-to-population pathway. The spectral features of (B) and (C) are comparable. All three of the example Liouville pathways contribute a single oscillatory frequency to both a diagonal peak and a cross peak

ruled out for the cross peak oscillations. Three such Liouville pathways are shown in Figure 5.7, exemplifying pathways which involve simple coherence transfer, t_2 coherence-population transfer, and t_2 population-coherence transfer.

Writing a set of Liouville pathways to explain the anomalous oscillatory features of our rephasing data is slightly more involved, partially due to a lack of oscillatory features on the diagonal of the spectrum. The absence of oscillatory features on the diagonal excludes all Liouville pathways in which the system evolves in the same state during t_1 and t_3. Some representative Liouville diagrams are shown in Figure 5.8. The excited-state absorption of the (**4**, **1**) cross peak provides an excellent example of the constraints

involved in determining potential Liouville pathways to explain the spectral features. To write a Liouville pathway which is evolves at mode 4's frequency during t_1, evolves in a coherence between modes 1 and 2 during t_2, and is detected at frequency of mode 1's excited state absorption, at least three vibrational states must be involved, and only two of them may contribute to the sequence of field-matter interactions. A coherence involving

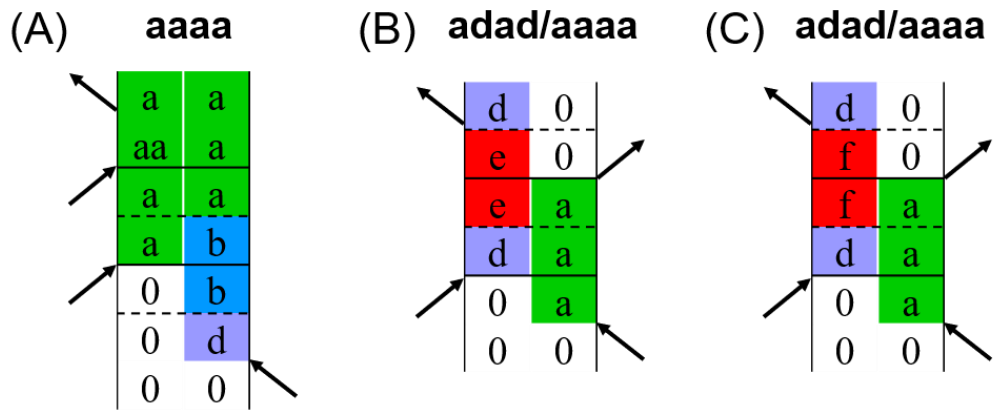

Figure 5.8: Potential Liouville pathways for three of the anomalous rephasing cross peak frequency components. (A) Coherence-to-population transfer pathway contributing to the excited-state absorption of the (**4**, **1**) and (**2**, **1**) cross peaks which oscillates at the (**2**, **1**) difference frequency. (B) Coherence-coherence transfer pathway contributing to the (**1**, **4**) and (**1**, **5**) cross peaks and oscillating at the (**1**, **4**) and (**1**, **5**) difference frequencies. (C) Coherence-coherence transfer pathway contributing to the (**1**, **4**) cross peak and oscillating at the (**1**, **4**) and (**1**, **6**) difference frequencies.

either mode 2 or mode 4 must therefore be introduced to the diagram through coherence transfer. Limiting ourselves to Liouville pathways involving at most one coherence transfer per waiting time, we are unable to write any pathways that meet such criteria except for one which involves a coherence-coherence transfer during t_1 and a coherence-population transfer during t_2, and which depends upon the parallel nature of mode 1 and mode 4's transition dipole moments for its nonvanishing orientational response. A similar pathway may be written for the conjugate peak.

Notwithstanding the specificity encountered in writing a suitable Liouville pathway for the excited-state absorption of the (**4**, **1**) cross peak, the most puzzling cross peak frequency in the rephasing data set an oscillatory feature of ~ 88 cm^{-1} on the (**4**, **1**) cross peak and its conjugate in the disulfide and xyl. Coherence maps for this frequency and representative peak amplitude traces and Fourier transforms for one of the involved cross peaks are shown in Figure 5.9. There is no corresponding difference frequency in any of

the diiron hexacarbonyls tested, and 88 cm^{-1} is greater than the difference frequency of modes 1 and 4 and lesser than the difference frequency of modes 1 and 5. This anomalous difference frequency is present in both xyl and the disulfide, which would seem to preclude it being an experimental artifact, and there is a sixth carbonyl vibrational mode in the diiron hexacarbonyl compounds we test. Electronic structure calculations place its vibrational frequency between that of mode 5 and mode 4, with frequency difference from mode 1 which corresponds well to the oscillatory frequency observed in the cross peak of mode1 and mode 4. This sixth mode (labeled as mode 6 in Figure 1.1C) is IR-inactive and Raman active, and it has been assigned in the resonance Raman spectrum of (μ-edt)$[Fe(CO)_3]_2$ dissolved in CH_3CN,[44] where its frequency is between the frequencies of modes 4 and 5,

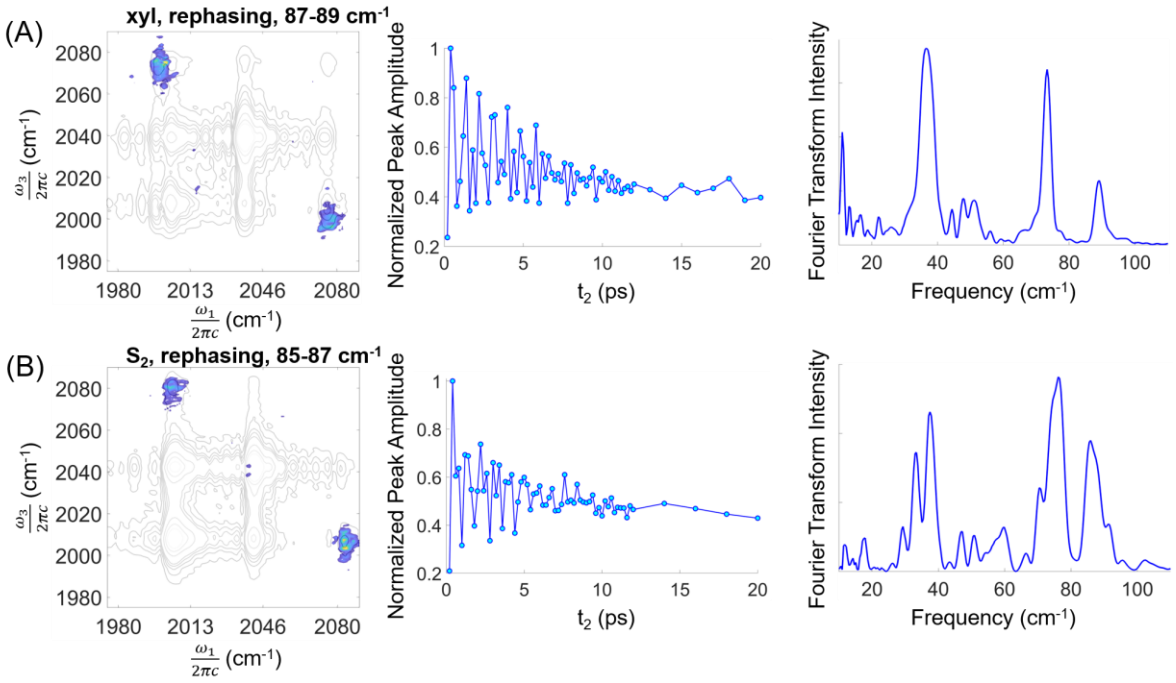

Figure 5.9: (A) Coherence maps of xyl highlighting the 88-89 cm^{-1} frequency in rephasing data. Peak amplitude data for the (**4**, **1**) cross peak and the Fourier transform of the peak amplitude are shown, illustrating three frequency components at ~ 38, 73, and 88 cm^{-1}. (B) Coherence maps of the disulfide highlighting the 85-87 cm^{-1} frequency. Peak amplitude data for the (**4**, **1**) cross peak and the Fourier transform of the peak amplitude are shown, illustrating three frequency components at ~ 38, 78, and 86 cm^{-1}.

as predicted by electronic structure calculations. It is impossible to extract the exact frequency difference of modes 1 and 6 from the resonance Raman spectrum due to a pronounced IR-Raman noncoincidence effect,[49-50] but the good correspondence of

relative mode ordering reported the experimental literature and predicted by our calculations supports our hypothesis that the anomalous frequency of ~ 87 cm-1 observed in the disulfide and xyl coes correspond to the difference frequency of modes 1 and 6. To the best of our knowledge, this represents the first use of coherence transfer to probe the vibrational characteristics and dynamics of dark modes in 2D-IR.

Our data represents a formidable challenge to detailed theoretical analysis, in many respects due to its clarity and the evident spectral patterns across data sets. It is apparent that in the rephasing data most of the unexpected cross peak frequency components arise from the manifold of difference frequencies associated with mode 1, and typically occur on specific cross peaks, primarily the (**4**, **1**) cross peak and its conjugate. It is equally apparent that in the nonrephasing data sets the cross peak oscillations that we attribute to coherence transfer typically occur on cross peaks associated with mode 2, and unlike the rephasing data, there are no cross peak oscillations in the nonrephasing data sets with more than one significant frequency component. It is not immediately clear to us why the (**4**, **1**) cross peak should so consistently display signatures of vibrational coherence transfer when other cross peaks do not show comparable oscillatory features, or why these anomalous frequencies invariably correspond to the difference of mode 1 and another carbonyl vibration. It appears that there may be a specific set of molecular conditions which enhance the probability of a coherence transfer event, and that at least some of these conditions are associated with mode 1 or mode 1's manifold of difference frequencies. A similar pattern is apparent for mode 2 in the nonrephasing spectrum. Why all of the cross peaks with multiple oscillatory features occur in rephasing spectra and why all of the cross peaks with oscillatory features in nonrephasing spectra are associated with mode 2 is equally unclear to us, but the pattern is apparent.

We note also that Liouville pathways for many of the anomalous cross peak frequencies we observe, in both rephasing and nonrephasing spectra, may be written to involve a coherence-population transfer during t_2 – indeed, this seems necessary to explain the oscillatory features observed on the excited-state absorption of the (**4**, **1**) cross peak. Future investigation of the coherence transfer phenomena in this and similar systems may garner significant insight in by determining whether coherence-population transfer does

significantly contribute the vibrational dynamics of the system, and what, if any, set of conditions enhances the occurrence of coherence transfer with the manifold of mode 1.

5.5 Conclusion

We report signatures of vibrational coherence transfer in three diiron hexacarbonyl mimics of the [FeFe]-hydrogenase enzyme active site. These coherence transfer signatures are consistently associated with specific carbonyl vibrational modes and are present in all three compounds, suggesting an underlying dependence of coherence transfer upon specific vibrational characteristics or molecular topology. To the best of our knowledge, this is the first observation of oscillatory features in 2D-IR nonrephasing cross peaks. We report also what appears to be coherence transfer between a bright and a dark mode in two of the three tested compounds. To the best of our knowledge, this is also the first use of coherence transfer phenomena to identify and probe the vibrational dynamics of dark modes in 2D-IR. We suggest that these systems provide optimal systems for the investigation coherence transfer phenomena in excitonic systems. Our experimental data is clear and consistent, and theoretical investigation is necessary to explain the patterns we report.

References

1. Cramer, W.; Bondeau, A.; Woodward, F. I.; Prentice, I. C.; Betts, R. A.; Brovkin, V.; Cox, P. M.; Fisher, V.; Foley, J. A.; Friend, A. D.; Kucharik, C.; Lomas, M. R.; Ramankutty, N.; Sitch, S.; Smith, B.; White, A.; Young-Molling, C., Global response of terrestrial ecosystem structure and function to CO_2 and climate change: results from six dynamic global vegetation models. *Global Change Biol* **2001,** *7*, 357-373.

2. Doney, S. C.; Fabry, V. J.; Feely, R. A.; Kleypas, J. A., Ocean Acidification: The Other CO_2 Problem. *Annu Rev Mar Sci* **2009,** *1*, 169-192.

3. Green, M. A.; Hishikawa, Y.; Dunlop, E. D.; Levi, D. H.; Hohl-Ebinger, J.; Ho-Baillie, A. W. Y., Solar cell efficiency tables (version 51). *Prog Photovoltaics* **2018,** *26*, 3-12.

4. Blankenship, R. E.; Tiede, D. M.; Barber, J.; Brudvig, G. W.; Fleming, G.; Ghirardi, M.; Gunner, M. R.; Junge, W.; Kramer, D. M.; Melis, A.; Moore, T. A.; Moser, C. C.; Nocera, D. G.; Nozik, A. J.; Ort, D. R.; Parson, W. W.; Prince, R. C.; Sayre, R. T., Comparing Photosynthetic and Photovoltaic Efficiencies and Recognizing the Potential for Improvement. *Science* **2011,** *332*, 805-809.

5. Gust, D.; Moore, T. A.; Moore, A. L., Solar Fuels via Artificial Photosynthesis. *Accounts Chem Res* **2009,** *42*, 1890-1898.

6. Frese, R. N.; Germano, M.; de Weerd, F. L.; van Stokkum, I. H. M.; Shkuropatov, A. Y.; Shuvalov, V. A.; van Gorkom, H. J.; van Grondelle, R.; Dekker, J. P., Electric field effects on the chlorophylls, pheophytins, and beta-carotenes in the reaction center of photosystem II. *Biochemistry-Us* **2003,** *42*, 9205-9213.

7. Swenberg, C. E.; Geacintov, N. E.; Pope, M., Bimolecular Quenching of Excitons and Fluorescence in Photosynthetic Unit. *Biophys J* **1976,** *16*, 1447-1452.

8. Fassioli, F.; Dinshaw, R.; Arpin, P. C.; Scholes, G. D., Photosynthetic light harvesting: excitons and coherence. *J R Soc Interface* **2014,** *11,* 20130901.

9. Prokhorenko, V. I.; Steensgaard, D. B.; Holzwarth, A. R., Exciton theory for supramolecular chlorosomal aggregates: 1. Aggregate size dependence of the linear spectra. *Biophys J* **2003,** *85*, 3173-3186.

10. Spano, F. C., The Spectral Signatures of Frenkel Polarons in H- and J-Aggregates. *Accounts Chem Res* **2010,** *43*, 429-439.

11. Kraner, S.; Prampolini, G.; Cuniberti, G., Exciton Binding Energy in Molecular Triads. *J Phys Chem C* **2017,** *121*, 17088-17095.

12. Bardeen, C. J., The Structure and Dynamics of Molecular Excitons. *Annual Review of Physical Chemistry, Vol 65* **2014,** *65*, 127-148.

13. Kasha, M., Energy Transfer Mechanisms and the Molecular Exciton Model for Molecular Aggregates. *Radiat Res* **2012,** *178*, Av27-Av34.

14. King, J. T.; Baiz, C. R.; Kubarych, K. J., Solvent-Dependent Spectral Diffusion in a Hydrogen Bonded "Vibrational Aggregate". *J Phys Chem A* **2010,** *114*, 10590-10604.

15. Alden, R. G.; Cheng, W. D.; Lin, S. H., Vibrational-Relaxation and Coherence and Primary Electron-Transfer in Photosynthetic Reaction Centers. *Chem Phys Lett* **1992,** *194*, 318-326.

16. Vos, M. H.; Jones, M. R.; Martin, J. L., Vibrational coherence in bacterial reaction centers: spectroscopic characterisation of motions active during primary electron transfer. *Chem Phys* **1998**, *233*, 179-190.

17. Chudoba, C.; Riedle, E.; Pfeiffer, M.; Elsaesser, T., Vibrational Coherence in Ultrafast Excited State Proton Transfer. *Chem Phys Lett* **1996,** *263*, 622-628.

18. Wynne, K.; Reid, G. D.; Hochstrasser, R. M., Vibrational Coherence in Electron Transfer: The Tetracyanoethylene-Pyrene Complex. *J Chem Phys* **1996,** *105*, 2287.

19. Takeuchi, S.; Tahara, T., Coherent Nuclear Wavepacket Motions in Ultrafast Excited-State Intramolecular Proton Transfer: Sub-30-fs Resolved Pump-Probe Absorption Spectroscopy of 10-hydroxybenzo[h]quinoline in Solution. *J Phys Chem A* **2005,** *109*, 10199-10207.

20. Higashi, M.; Saito, S., Direct Simulation of Excited-State Intramolecular Proton Transfer and Vibrational Coherence of 10-Hydroxybenzo[h]quinoline in Solution. *J Phys Chem Lett* **2011,** *2*, 2366-2371.

21. Rury, A. S.; Sorenson, S. A.; Dawlaty, J. M., Evidence of Ultrafast Charge Transfer Driven by Coherent Lattice Vibrations. *J Phys Chem Lett* **2017,** *8*, 181-187.

22. Delor, M.; Keane, T.; Scattergood, P. A.; Sazanovich, I. V.; Greetham, G. M.; Towrie, M.; Meijer, A. J. H. M.; Weinstein, J. A., On the mechanism of vibrational control of light-induced charge transfer in donor-bridge-acceptor assemblies. *Nat Chem* **2015,** *7*, 689-695.

23. Delor, M.; Archer, S. A.; Keane, T.; Meijer, A. J. H. M.; Sazanovich, I. V.; Greetham, G. M.; Towrie, M.; Weinstein, J. A., Directing the path of light-induced electron transfer at a molecular fork using vibrational excitation. *Nat Chem* **2017,** *9*, 1099-1104.

24. Engel, G. S.; Calhoun, T. R.; Read, E. L.; Ahn, T. K.; Mancal, T.; Cheng, Y. C.; Blankenship, R. E.; Fleming, G. R., Evidence for wavelike energy transfer through quantum coherence in photosynthetic systems. *Nature* **2007,** *446*, 782-786.

25. Panitchayangkoon, G.; Hayes, D.; Fransted, K. A.; Caram, J. R.; Harel, E.; Wen, J. Z.; Blankenship, R. E.; Engel, G. S., Long-lived quantum coherence in photosynthetic complexes at physiological temperature. *P Natl Acad Sci USA* **2010,** *107*, 12766-12770.

26. Panitchayangkoon, G.; Voronine, D. V.; Abramavicius, D.; Caram, J. R.; Lewis, N. H. C.; Mukamel, S.; Engel, G. S., Direct evidence of quantum transport in photosynthetic light-harvesting complexes. *P Natl Acad Sci USA* **2011,** *108*, 20908-20912.

27. Tiwari, V.; Peters, W. K.; Jonas, D. M., Electronic resonance with anticorrelated pigment vibrations drives photosynthetic energy transfer outside the adiabatic framework. *P Natl Acad Sci USA* **2013,** *110*, 1203-1208.

28. Roscioli, J. D.; Ghosh, S.; LaFountain, A. M.; Frank, H. A.; Beck, W. F., Quantum Coherent Excitation Energy Transfer by Carotenoids in Photosynthetic Light Harvesting. *J Phys Chem Lett* **2017,** *8*, 5141-5147.

29. Scholes, G. D.; Fleming, G. R.; Chen, L. X.; Aspuru-Guzik, A.; Buchleitner, A.; Coker, D. F.; Engel, G. S.; van Grondelle, R.; Ishizaki, A.; Jonas, D. M.; Lundeen, J. S.; McCusker, J. K.; Mukamel, S.; Ogilvie, J. P.; Olaya-Castro, A.; Ratner, M. A.; Spano, F. C.; Whaley, K. B.; Zhu, X. Y., Using coherence to enhance function in chemical and biophysical systems. *Nature* **2017,** *543*, 647-656.

30. Duan, H. G.; Prokhorenko, V. I.; Cogdell, R. J.; Ashraf, K.; Stevens, A. L.; Thorwart, M.; Miller, R. J. D., Nature does not rely on long-lived electronic quantum coherence for photosynthetic energy transfer. *P Natl Acad Sci USA* **2017,** *114*, 8493-8498.

31. Fuller, F. D.; Pan, J.; Gelzinis, A.; Butkus, V.; Senlik, S. S.; Wilcox, D. E.; Yocum, C. F.; Valkunas, L.; Abramavicius, D.; Ogilvie, J. P., Vibronic coherence in oxygenic photosynthesis. *Nat Chem* **2014,** *6*, 706-711.

32. Khalil, M.; Demirdoven, N.; Tokmakoff, A., Vibrational coherence transfer characterized with Fourier-transform 2D IR spectroscopy. *J Chem Phys* **2004,** *121*, 362.

33. Marroux, H. J. B.; Orr-Ewing, A. J., Distinguishing Population and Coherence Transfer Pathways in a Metal Dicarbonyl Complex Using Pulse-Shaped Two-Dimensional Infrared Spectroscopy. *J Phys Chem B* **2016,** *120*, 4125-4130.

34. Pakoulev, A. V.; Rickard, M. A.; Mathew, N. A.; Kornau, K. M.; Wright, J. C., Frequency-domain time-resolved four wave mixing spectroscopy of vibrational coherence transfer with single-color excitation. *J Phys Chem A* **2008,** *112*, 6320-6329.

35. Rickard, M. A.; Pakoulev, A. V.; Kornau, K.; Mathew, N. A.; Wright, J. C., Interferometric coherence transfer modulations in triply vibrationally enhanced four-wave mixing. *J Phys Chem A* **2006,** *110*, 11384-11387.

36. Nee, M. J.; Baiz, C. R.; Anna, J. M.; McCanne, R.; Kubarych, K. J., Multilevel vibrational coherence transfer and wavepacket dynamics probed with multidimensional IR spectroscopy. *J Chem Phys* **2008,** *129*, 084503.

37. Baiz, C. R.; Kubarych, K. J.; Geva, E., Molecular Theory and Simulation of Coherence Transfer in Metal Carbonyls and Its Signature on Multidimensional Infrared Spectra. *J Phys Chem B* **2011,** *115*, 5322-5339.

38. Lyon, E. J.; Georgakaki, I. P.; Reibenspies, J. H.; Darensbourg, M. Y., Coordination sphere flexibility of active-site models for Fe-only hydrogenase: Studies in intra- and intermolecular diatomic ligand exchange. *J Am Chem Soc* **2001,** *123*, 3268-3278.

39. Stanley, J. L.; Rauchfuss, T. B.; Wilson, S. R., Studies on the condensation pathway to and properties of diiron azadithiolate carbonyls. *Organometallics* **2007,** *26*, 1907-1911.

40. Hamm, P.; Zanni, M. T., *Concepts and methods of 2d infrared spectroscopy*. Cambridge University Pres: Cambridge ; New York, 2011.

41. Khalil, M.; Demirdoven, N.; Tokmakoff, A., Coherent 2D IR Spectroscopy: Molecular Structure and Dynamics in Solution. *J Phys Chem A* **2003,** *107*, 5258-5279.

42. Golonzka, O.; Tokmakoff, A., Polarization-Selective Third-Order Spectroscopy of Coupled Vibronic States. *J Chem Phys* **2001,** *115*, 297.

43. Mukamel, S., *Principles of nonlinear optical spectroscopy*. Oxford University Press: New York, 1995.

44. Galinato, M. G. I.; Whaley, C. M.; Lehnert, N., Vibrational Analysis of the Model Complex (mu-edt[$Fe(CO)_3$]$_2$ and Comparison to Iron-Only Hydrogenase: The Activation Scale of Hydrogenase Model Systems. *Inorg Chem* **2010,** *49*, 3201-3215.

45. Stromberg, C. J.; Kohnhorst, C. L.; Van Meter, G. A.; Rakowski, E. A.; Caplins, B. C.; Gutowski, T. A.; Mehalko, J. L.; Heilweil, E. J., Terahertz, Infrared and Raman Vibrational Assignments of [FeFe]-hydrogenase Model Compounds. *Vib Spectrosc* **2011,** *56*, 219-227.

46. Rose, M. E., *Elementary Theory of Angular Momentum*. Wiley: New York, 1957.

47. Wigner, E. P., *Group theory and its application to the quantum mechanics of atomic spectra*. Expanded and improved ed.; Academic Press: New York, 1959.

48. Berne, B. J.; Pecora, R., *Dynamic light scattering : with applications to chemistry, biology, and physics*. R.E. Krieger Pub. Co.: Malabar, Fla., 1990.

49. Torii, H., Extent of delocalization of vibrational modes in liquids as a result of competition between diagonal disorder and off-diagonal coupling. *J Phys Chem A* **2004,** *108*, 2103-2107.

50. Torii, H.; Musso, M.; Giorgini, M. G., Time-domain theoretical analysis of the noncoincidence effect, diagonal frequency shift, and the extent of delocalization of the C=O stretching mode of acetone/dimethyl sulfoxide binary liquid mixtures. *J Phys Chem A* **2005,** *109*, 7797-7804.

Chapter 6
Conclusion

6.1 Summary

The studies detailed in this thesis follow one cohesive theme, an investigation of the dynamical processes which contribute to chemical reactivity on an ultrafast timescale in biomimetic small-molecule catalysts. To this end we employ two-dimensional infrared spectroscopy to probe the picosecond dynamics of metal carbonyl vibrations. With one exception our investigation is focused upon small molecule mimics of the [FeFe]-hydrogenase enzyme active site. We demonstrate that 2D-IR spectroscopy is an excellent method for experimental studies of molecular redox events, conformational flexibility, steric hindrance, and excitonic vibrational coherence transfer.

In the first section of this work we describe our investigation of the effect of molecular oxidation on the vibrational dynamics of an organometallic catalyst [(1,1'-bis(diphenylphosphino)ferrocene)chromium(0)]tetracarbonyl (DPPFCr). DPPFCr is not a biomimetic compound but its carbonyl vibrational modes are directly comparable pre- and post-oxidation, and its molecular topology is minimally distorted by the redox event. This allows us to directly compare the vibrational structure of the compound before and after molecular oxidation. We find that the vibrational relaxation of the carbonyl modes is accelerated in the oxidized state but that the spectral diffusion of the carbonyl modes is not significantly affected. We interpret the comparable dynamics of spectral diffusion in both oxidation states to an idiosyncrasy of the experimental solvent. The accelerated vibrational relaxation is hypothesized to arise from increased anharmonic coupling of the vibrational modes to lower frequency bath modes in the oxidized state, and discuss the similarity of our experimental findings to recent investigations of similar organometallic complexes in ^{3}MLCT excited states.

In the second chapter of this work we describe our investigation of spectral dynamics of (μ-pdt)$[Fe(CO)_3]_2$, an archetypical small-molecule mimic of the hydrogenase enzyme active site. We report clear solvent-insensitive spectral diffusion of the carbonyl vibrations in alkane solvents, and relate this to a known mode of catalytically relevant self-isomerization in diiron hexacarbonyl small molecules which is hypothesized to contribute to the reactivity of the [FeFe]-hydrogenase enzyme. Using electronic structure calculations we calculate the Boltzmann distribution of states and show that a range of molecular conformations are represented in solution at room temperature. We find a clear correlation between CO bond length and carbonyl local mode vibrational frequency in a series of chromium tricarbonyl compounds using electronic structure calculations and find a striking agreement between our experimental peak widths and the CO bond length distribution predicted by our calculated distribution of states. We extend our investigation to two other metal carbonyl complexes, $M_3(CO)_{12}$ (M = Ru, Os), and find clear spectral diffusion of the carbonyl vibrations in alkane solvents. This study represents the first use of spectral diffusion to probe conformational flexibility in molecular compounds.

In the third chapter of this work we describe our investigation of the spectral dynamics induced by partial nanoconfinement in catalytically relevant dendritic biomimics of the [FeFe]-hydrogenase enzyme active site. We incorporate a diiron hexacarbonyl compound into a second-generation Frechet-type poly(aryl ether) dendrimer and directly compare the vibrational dynamics of the carbonyl ligands in the dendritic compound with the vibrational frequencies of the carbonyl ligands in $[Fe(\mu\text{-}S)(CO)_3]_2$, which is analogous to the core of the dendritic compound. We report an unusual solvent-dependent partition of vibrational frequencies in both the dendrimer and $[Fe(\mu\text{-}S)(CO)_3]_2$ and hypothesize that it represents a specific solvent-dependent microenvironment. We find that encapsulation in the dendrimer sometimes significantly slows the initial phase of carbonyl vibrational relaxation and that the spectral diffusion of the carbonyl ligands in the dendritic assembly display an additional slow timescale which is absent in $[Fe(\mu\text{-}S)(CO)_3]_2$. We correlate the patterns of spectral diffusion in the dendrimer with previous studies of the solvent-dependence of the conformation of poly(aryl ether) dendrimers and suggest that the spectral diffusion of the carbonyl groups at the core of the dendrimer reflects the

conformational mobility of the dendritic assembly and represents a case of partial nano-confinement.

In the fourth and last chapter of this work we describe our investigation of vibrational coherence transfer in three diiron hexacarbonyl mimics of the [FeFe]-hydrogenase active site. We find specific oscillatory features in the crosspeaks of our 2D spectra for all three compounds which indicate the presence of vibrational coherence transfer dynamics in alkane solvents. We also find an anomalous oscillatory feature in the spectra of two of the compounds which we hypothesize to reflect coherence transfer dynamics involving a carbonyl vibrational mode which is dark in the infrared. This work represents the first identification of vibrational coherence transfer using oscillatory features in the crosspeaks of nonrephasing 2D-IR spectra, and the first identification of coherence transfer to a dark vibrational mode. We discuss our experimental results in the context of the investigation of coherence-transfer dynamics in biological light-harvesting assemblies and suggest that small-molecule diiron hexacarbonyl compounds provide an excellent system for the investigation of excitonic coherence transfer dynamics.

6.2 Outlook

Biomimetic catalytic systems are typically designed to incorporate a number of factors which are ideal for 2D-IR experiments, including strong vibrational transitions in relatively uncongested regions of the infrared spectrum, relative ease of synthetic preparation, robust chemical stability under typical experimental conditions, and computationally tractable molecular size. In addition to their promise as systems in 2D-IR spectroscopy biomimetic catalytic systems are designed to incorporate the physical conditions which enhance chemical reactivity in biological systems, including the hydrophobic effect, nano-confinement, participation of the first and second coordination spheres in the reactivity of the active site, and fine-tuning of the reorganizational energy and photochemistry of the system.[1-4] We hope that in this thesis we have been able to demonstrate the experimental tractability and physical complexity of small- and moderately-sized biomimetic catalysts.

The work in this thesis has focused upon the vibrational dynamics of a class of compounds incorporating the diiron hexacarbonyl chemical motif. Several other research groups have used 2D-IR spectroscopy to probe the vibrational dynamics and photochemistry of these compounds,[5-6] but the published 2D-IR studies of this class of compounds only scratches the surface of the rich chemical dynamics and reactivity that has been built into these compounds. Chapter 3 of this work described our identification of the conformational flexibility of (μ-pdt)$[Fe(CO)_3]_2$. The activation energy of the isomerization which facilitates chemical reactivity in (μ-pdt)$[Fe(CO)_3]_2$ is ~ 10 kcal/mol, too high for the isomerization to be experimentally accessible on our timescale. Darensbourg's group has used steric interactions between the carbonyl groups and the disulfide bridging group to significantly lower the activation energy to of this isomerization.[7] A natural extension of our investigation in Chapter 3 would be to use steric interactions with the disulfide bridging group to lower the activation energy until the isomerization occurs significantly on the picosecond timescale and characterize the isomerization using 2D-IR. In addition to this a wide variety of diiron hexacarbonyl photocatalysts have been reported, and the excited state dynamics of these compounds are typically tunable through the bridging dithiolate group.[8-11] These systems offer ideal

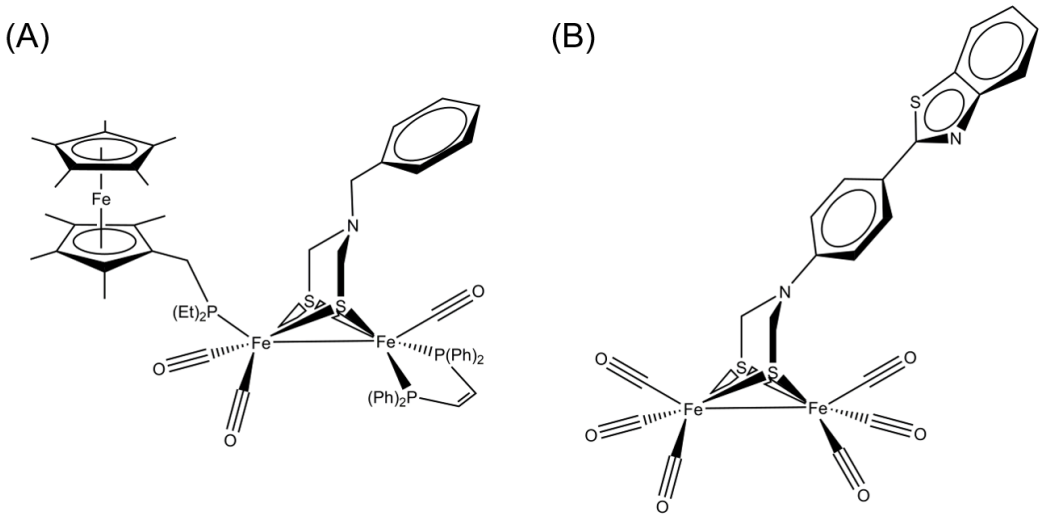

Figure 6.1: (A) A biomimetic model of the [FeFe]-hydrogenase active site and FeS cluster. This biomimetic compound has been shown to display reversible redox chemistry, redox-dependent isomerization, and the formation of metal hydrides, all of which produce marked changes in the carbonyl vibrational bands.[16] (B) Photosensitized diiron hexacarbonyl catalyst for the formation of H_2. The small organic photosensitizer makes this system easily tractable for computational studies as well as experimental work.[11]

platforms for spectroscopic investigation of the excited-state dynamics of diiron hexacarbonyl compounds, and the excited-state dynamics of several diiron hexacarbonyl compounds have been reported, although these studies have typically focused upon carbonyl dissociation and not upon intramolecular charge transfer from a photosensitizer to the diiron hexacarbonyl core.[12-15] Figure 6.1 shows two excellent diiron hexacarbonyl compounds for future studies. Figure 6.1A shows a system designed by Camara et. al. to mimic the active site of the [FeFe]-hydrogenase enzyme which has been demonstrated to exhibit a number of biomimetic features, including coordination-sphere reorganization after redox events, stable redox chemistry, and protonation to form a metal-hydride complex.[16] Figure 6.1B shows a diiron hexacarbonyl covalently bonded to small organic photosensitizer, which has been shown to catalyze the production of H_2.[11]

We have reported the first 2D-IR spectroscopic investigation of a dendritic system, but the dendrimer we studied is only second-generation and is relatively small compared to other dendritic systems.[17-18] A systematic investigation of several sequential dendrimer generations in the system we reported using 2D-IR and molecular dynamics simulations would certainly yield valuable insight into the dynamics of nano-confinement in dendrimers and other conformationally mobile systems. Studies of the electronic excited state may be easily performed in tandem with studies of the electronic ground state, and would be insightful in elucidating the effect of conformationally-mobile nano-confinement on the photophysics of biomimetic catalysts. To the best of our knowledge no such experiments have ever been performed using 2D spectroscopy, despite widely recognized examples of the modulating influence of nano-confinement on photochemistry and photophysics.[18-20]

Cavitands and hemicarcerands represent another ubiquitous and easily accessible form of molecular nano-confinement. Cyclodextrins and cyclodextrin-metal carbonyl host-guest complexes have been extensively studied for decades[21-22] but to the best of our knowledge there has only been one study of a cyclodextrin-encapsulated catalyst using 2D methodology, in which a cyclodextrin-$(Cp)Cr(CO)_3$ host-guest complex was investigated using 2D-IR in a series of linear alcohols.[23] Modern cavitands are widely used and carefully tailor-made for specific chemical applications, and not only are cavitand-hosted reactions

of significant interest to the catalytic community[24-27] but cavitands and carcerands are excellent systems for the study of the hydrophobic effect, reorganizational dynamics

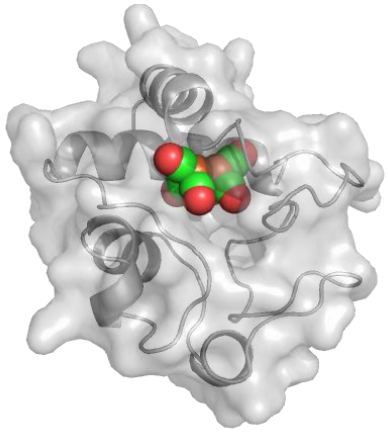

Figure 6.2: A modified cytochrome c protein where the heme group has been replaced with a biomimetic diiron hexacarbonyl core. This artificial enzyme has been shown to be a modest catalyst for the production of H_2 in aqueous media.[30]

during redox events, and photochemistry and photophysics of nano-confined catalysts.[1, 19, 25, 28-29] In a related vein, Sano et. al. recently reported the creation of an artificial photocatalytic enzyme by replacing the heme group of cytochrome c with a diiron hexacarbonyl group.[30] This artificial enzyme is shown in Figure 6.2. In the presence of a Ru-based photosensitizer and a sacrificial proton donor the enzyme showed modest production of H_2. Work is underway in the Kubarych group to replicate this synthesis and use the carbonyl vibrations of the diiron active site to probe the dynamics of the enzyme on an ultrafast timescale.

The relevance of excitonic coherences to biomolecular assemblies remains uncertain,[31-33] but vibrationally- and vibronically-modulated chemical reactivity are widely known and have received significant recent interest.[34-38] The first observation of unusually long-lived coherences and the association of those coherences with the light-harvesting mechanism occurred using 2D spectroscopy, and 2D electronic spectroscopy has remained at the center of the ensuing debate. In Chapter 5 we demonstrated that 2D-IR spectroscopy offers an excellent method to investigate excitonic coherence and coherent dynamics in small-molecule systems which are easily amenable to explicit quantum-mechanical and QM/MM modeling. Further extension of this work to include vibronic coherence in photoexcited complexes and investigation of vibrational coherences in polar

and interacting solvents may shed further light on coherence transfer dynamics in excitonic molecular systems.

References

1. Bistri, O.; Reinaud, O., Supramolecular control of transition metal complexes in water by a hydrophobic cavity: a bio-inspired strategy. *Org Biomol Chem* **2015,** *13*, 2849-2865.

2. Dydio, P.; Reek, J. N. H., Supramolecular control of selectivity in transition-metal catalysis through substrate preorganization. *Chem Sci* **2014,** *5*, 2135-2145.

3. Zhao, M.; Wang, H. B.; Ji, L. N.; Mao, Z. W., Insights into Metalloenzyme Microenvironments: Biomimetic Metal Complexes with a Functional Second Coordination Sphere. *Chem Soc Rev* **2013,** *42*, 8360-8375.

4. Hecht, S.; Frechet, J. M. J., Dendritic Encapsulation of Function: Applying Nature's Site Isolation Principle from Biomimetics to Materials Science. *Angew Chem Int Edit* **2001,** *40*, 74-91.

5. Kaziannis, S.; Wright, J. A.; Candelaresi, M.; Kania, R.; Greetham, G. M.; Parker, A. W.; Pickett, C. J.; Hunt, N. T., The role of CN and CO ligands in the vibrational relaxation dynamics of model compounds of the [FeFe]-hydrogenase enzyme. *Phys Chem Chem Phys* **2011,** *13*, 10295-10305.

6. Nishida, J.; Tamimi, A.; Fei, H. H.; Pullen, S.; Ott, S.; Cohen, S. M.; Fayer, M. D., Structural dynamics inside a functionalized metal-organic framework probed by ultrafast 2D IR spectroscopy. *P Natl Acad Sci USA* **2014,** *111*, 18442-18447.

7. Crouthers, D. J.; Denny, J. A.; Bethel, R. D.; Munoz, D. G.; Darensbourg, M. Y., Conformational Mobility and Pendent Base Effects on Electrochemistry of Synthetic Analogues of the [FeFe]-Hydrogenase Active Site. *Organometallics* **2014,** *33*, 4747-4755.

8. Song, L. C.; Luo, F. X.; Liu, B. B.; Gu, Z. C.; Tan, H., Novel Ruthenium Phthalocyanine-Containing Model Complex for the Active Site of [FeFe]-Hydrogenases: Synthesis,

Structural Characterization, and Catalytic H-2 Evolution. *Organometallics* **2016,** *35*, 1399-1408.

9. Li, X. Q.; Wang, M.; Zhang, S. P.; Pan, J. X.; Na, Y.; Liu, J. H.; Akermark, B.; Sun, L. C., Noncovalent assembly of a metalloporphyrin and an iron hydrogenase active-site model: Photo-induced electron transfer and hydrogen generation. *J Phys Chem B* **2008,** *112*, 8198-8202.

10. Poddutoori, P.; Co, D. T.; Samuel, A. P. S.; Kim, C. H.; Vagnini, M. T.; Wasielewski, M. R., Photoinitiated multistep charge separation in ferrocene-zinc porphyrin-diiron hydrogenase model complex triads. *Energ Environ Sci* **2011,** *4*, 2441-2450.

11. Gao, S.; Huang, S.; Duan, Q.; Hou, J. H.; Jiang, D. Y.; Liang, Q. C.; Zhao, J. X., Iron-iron hydrogenase active subunit covalently linking to organic chromophore for light-driven hydrogen evolution. *Int J Hydrogen Energ* **2014,** *39*, 10434-10444.

12. Mirmohades, M.; Pullen, S.; Stein, M.; Maji, S.; Ott, S.; Hammarstrom, L.; Lomoth, R., Direct Observation of Key Catalytic Intermediates in a Photoinduced Proton Reduction Cycle with a Diiron Carbonyl Complex. *J Am Chem Soc* **2014,** *136*, 17366-17369.

13. Ridley, A. R.; Stewart, A. I.; Adamczyk, K.; Ghosh, H. N.; Kerkeni, B.; Guo, Z. X.; Nibbering, E. T. J.; Pickett, C. J.; Hunt, N. T., Multiple-timescale photoreactivity of a model compound related to the active site of [FeFe]-hydrogenase. *Inorg Chem* **2008,** *47*, 7453-7455.

14. Caplins, B. W.; Lomont, J. P.; Nguyen, S. C.; Harris, C. B., Vibrational Cooling Dynamics of a [FeFe]-Hydrogenase Mimic Probed by Time-Resolved Infrared Spectroscopy. *J Phys Chem A* **2014,** *118*, 11529-11540.

15. Johnson, M.; Thuman, J.; Letterman, R. G.; Stromberg, C. J.; Webster, C. E.; Heilweil, E. J., Time-Resolved Infrared Studies of a Trimethylphosphine Model Derivative of [FeFe]-Hydrogenase. *J Phys Chem B* **2013,** *117*, 15792-15803.

16. Camara, J. M.; Rauchfuss, T. B., Combining acid-base, redox and substrate binding functionalities to give a complete model for the [FeFe]-hydrogenase. *Nat Chem* **2012,** *4*, 26-30.

17. Helms, B.; Frechet, J. M. J., The Dendrimer Effect in Homogeneous Catalysis. *Adv Synth Catal* **2006,** *348*, 1125-1148.

18. Yu, T. J.; Zeng, Y.; Chen, J. P.; Li, Y. Y.; Yang, G. Q.; Li, Y., Exceptional Dendrimer-Based Mimics of Diiron Hydrogenase for the Photochemical Production of Hydrogen. *Angew Chem Int Edit* **2013,** *52*, 5631-5635.

19. Vallavoju, N.; Sivaguru, J., Supramolecular photocatalysis: combining confinement and non-covalent interactions to control light initiated reactions. *Chem Soc Rev* **2014,** *43*, 4084-4101.

20. Natarajan, B.; Gupta, S.; Ramamurthy, V.; Jayaraman, N., Interfacial Regions Governing Internal Cavities of Dendrimers. Studies of Poly(alkyl aryl ether) Dendrimers Constituted with Linkers of Varying Alkyl Chain Length. *J Org Chem* **2011,** *76*, 4018-4026.

21. Shimada, M.; Morimoto, Y.; Takahashi, S., Preparation and Properties of Cyclodextrin Metal-Carbonyl Inclusion-Compounds. *J Organomet Chem* **1993,** *443*, C8-C10.

22. Song, L. X.; Meng, Q. J.; You, X. Z., Preparation and Properties of Inclusion Compound of Cyclopentadienylmanganese Tricarbonyl Complex with a Beta-Cyclodextrin Dimer. *J Organomet Chem* **1995,** *498*, C1-C5.

23. Osborne, D. G.; King, J. T.; Dunbar, J. A.; White, A. M.; Kubarych, K. J., Ultrafast 2DIR probe of a host-guest inclusion complex: Structural and dynamical constraints of nanoconfinement. *J Chem Phys* **2013,** *138,* 144501.

24. Shi, Q. X.; Mower, M. P.; Blackmond, D. G.; Rebek, J., Water-Soluble Cavitands Promote Hydrolyses of Long-Chain Diesters. *P Natl Acad Sci USA* **2016,** *113*, 9199-9203.

25. Wieser, C.; Dieleman, C. B.; Matt, D., Calixarene and Resorcinarene Ligands in Transition Metal Chemistry. *Coordin Chem Rev* **1997,** *165*, 93-161.

26. De Rosa, M.; La Manna, P.; Talotta, C.; Soriente, A.; Gaeta, C.; Neri, P., Supramolecular Organocatalysis in Water Mediated by Macrocyclic Compounds. *Front Chem* **2018,** *6,* 1-16.

27. La Manna, P.; De Rosa, M.; Talotta, C.; Gaeta, C.; Soriente, A.; Floresta, G.; Rescifina, A.; Neri, P., The Hexameric Resorcinarene Capsule as an Artificial Enzyme: Ruling the Regio and Stereochemistry of a 1,3-Dipolar Cycloaddition Between Nitrones and Unsaturated Aldehydes. *Org Chem Front* **2018,** *5*, 827-837.

28. Natarajan, N.; Brenner, E.; Semeril, D.; Matt, D.; Harrowfield, J., The Use of Resorcinarene Cavitands in Metal-Based Catalysis. *Eur J Org Chem* **2017**, 6100-6113.

29. Zhang, G.; Mastalerz, M., Organic Cage Compounds - from Shape-Persistency to Function. *Chem Soc Rev* **2014,** *43*, 1934-1947.

30. Sano, Y.; Onoda, A.; Hayashi, T., A hydrogenase model system based on the sequence of cytochrome c: photochemical hydrogen evolution in aqueous media. *Chem Commun* **2011,** *47*, 8229-8231.

31. Duan, H. G.; Prokhorenko, V. I.; Cogdell, R. J.; Ashraf, K.; Stevens, A. L.; Thorwart, M.; Miller, R. J. D., Nature does not rely on long-lived electronic quantum coherence for photosynthetic energy transfer. *P Natl Acad Sci USA* **2017,** *114*, 8493-8498.

32. Fuller, F. D.; Pan, J.; Gelzinis, A.; Butkus, V.; Senlik, S. S.; Wilcox, D. E.; Yocum, C. F.; Valkunas, L.; Abramavicius, D.; Ogilvie, J. P., Vibronic coherence in oxygenic photosynthesis. *Nat Chem* **2014,** *6*, 706-711.

33. Panitchayangkoon, G.; Voronine, D. V.; Abramavicius, D.; Caram, J. R.; Lewis, N. H. C.; Mukamel, S.; Engel, G. S., Direct evidence of quantum transport in photosynthetic light-harvesting complexes. *P Natl Acad Sci USA* **2011,** *108*, 20908-20912.

34. Chudoba, C.; Riedle, E.; Pfeiffer, M.; Elsaesser, T., Vibrational Coherence in Ultrafast Excited State Proton Transfer. *Chem Phys Lett* **1996,** *263*, 622-628.

35. Delor, M.; Archer, S. A.; Keane, T.; Meijer, A. J. H. M.; Sazanovich, I. V.; Greetham, G. M.; Towrie, M.; Weinstein, J. A., Directing the path of light-induced electron transfer at a molecular fork using vibrational excitation. *Nat Chem* **2017,** *9*, 1099-1104.

36. Delor, M.; Keane, T.; Scattergood, P. A.; Sazanovich, I. V.; Greetham, G. M.; Towrie, M.; Meijer, A. J. H. M.; Weinstein, J. A., On the mechanism of vibrational control of light-induced charge transfer in donor-bridge-acceptor assemblies. *Nat Chem* **2015,** *7*, 689-695.

37. Higashi, M.; Saito, S., Direct Simulation of Excited-State Intramolecular Proton Transfer and Vibrational Coherence of 10-Hydroxybenzo[h]quinoline in Solution. *J Phys Chem Lett* **2011,** *2*, 2366-2371.

38. Wynne, K.; Reid, G. D.; Hochstrasser, R. M., Vibrational Coherence in Electron Transfer: The Tetracyanoethylene-Pyrene Complex. *J Chem Phys* **1996,** *105*, 2287.

Appendix

A1: Spectral Diffusion and IVR Data for $[Fe(\mu\text{-}S)(CO)_3]_2$ and the Dendrimer

The decay of the inhomogeneity of mode 2 in the dendrimer and in $[Fe(\mu\text{-}S)(CO)_3]_2$ was different for all of the tested solvents, but several clear patterns were observed in the total data set. Interpretations of these patterns are presented in Chapter 4.4, as are representative data series for the inhomogeneity decay and decay of the peak amplitude in the nonrephasing spectra. We present the rest of the data here.

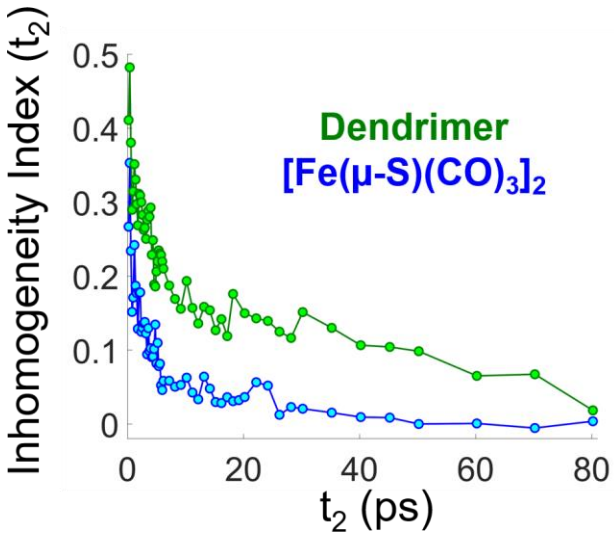

Figure A1: Inhomogeneity decay of mode 2 in $[Fe(\mu\text{-}S)(CO)_3]_2$ and the dendrimer in chloroform

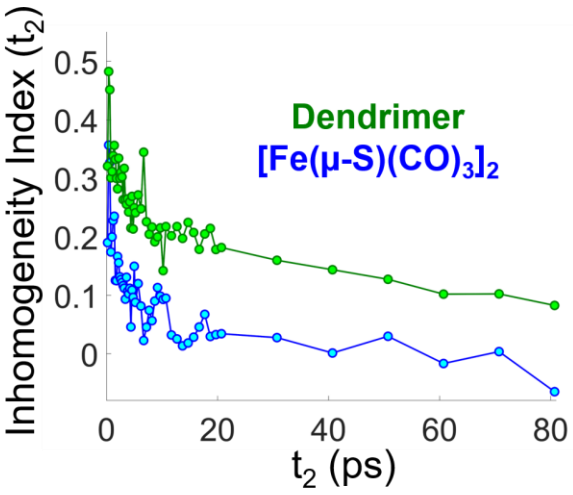

Figure A2: Inhomogeneity decay of mode 2 in $[Fe(\mu\text{-}S)(CO)_3]_2$ and the dendrimer in THF

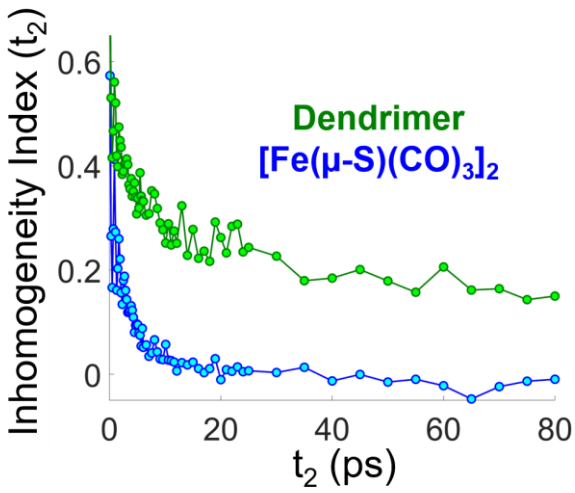

Figure A3: Inhomogeneity decay of mode 2 in $[Fe(\mu\text{-}S)(CO)_3]_2$ and the dendrimer in toluene

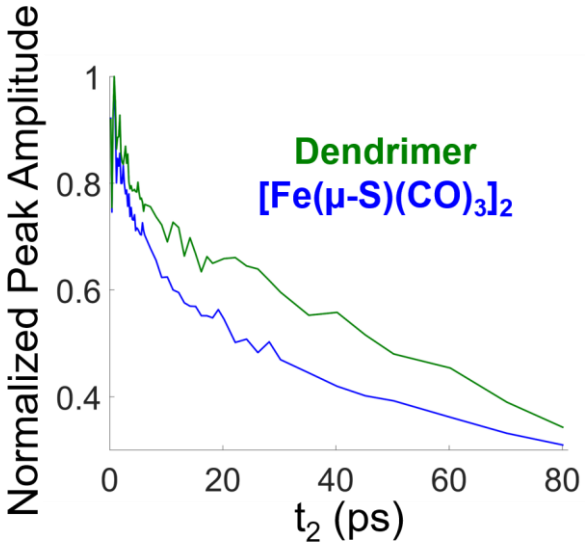

Figure A4: Decay of the nonrephasing peak amplitude of mode 2 in $[Fe(\mu\text{-}S)(CO)_3]_2$ and the dendrimer in chloroform

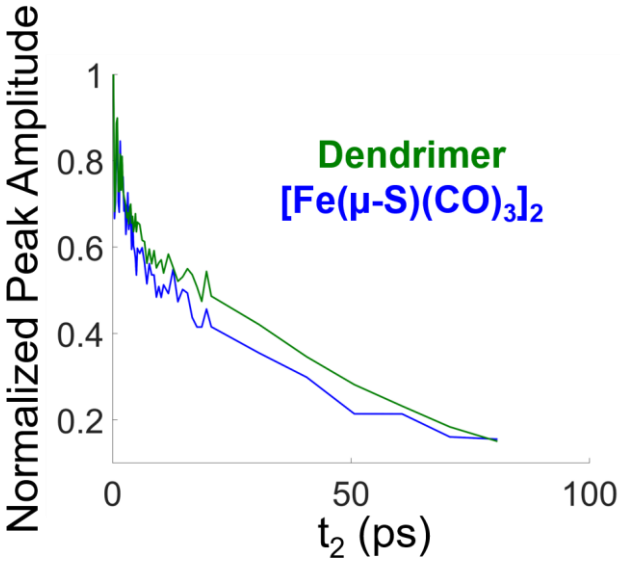

Figure A5: Decay of the nonrephasing peak amplitude of mode 2 in $[Fe(\mu\text{-}S)(CO)_3]_2$ and the dendrimer in THF

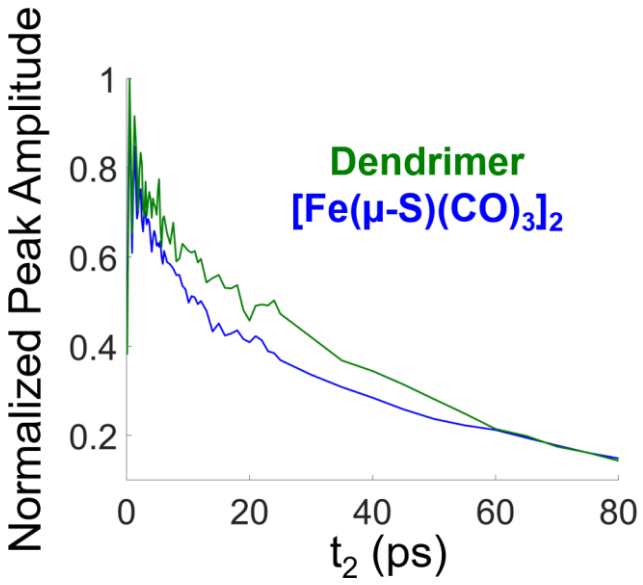

Figure A6: Decay of the nonrephasing peak amplitude of mode 2 in $[Fe(\mu\text{-}S)(CO)_3]_2$ and the dendrimer in toluene